TECHNISCHE
UNIVERSITÄT
DARMSTADT

Inelastic scattering of Ni and Zn isotopes off a proton target

Vom Fachbereich Physik
der Technischen Universität Darmstadt

zur Erlangung des Grades eines Doktors der Naturwissenschaften
(Dr. rer. nat.)

genehmigte Dissertation von

Mag. en Ciencias - Física
Martha Liliana Cortés Sua
aus Bogotá, Kolumbien

Referent: Prof. Dr. Dr. h. c. Norbert Pietralla
Korreferent: Prof. Dr. Thomas Aumann

Darmstadt 2016
D 17

Inelastic scattering of Ni and Zn isotopes off a proton target

Genehmigte Dissertation von
Mag. en Ciencias - Física Martha Liliana Cortés Sua
aus Bogotá, Kolumbien

Referent: Prof. Dr. Dr. h. c. Norbert Pietralla

Korreferent: Prof. Dr. Thomas Aumann

Tag der Einreichung: 15.06.2016

Tag der Prüfung: 18.07.2016

Darmstadt
D 17

Para Nana.

Abstract

Inelastic proton scattering of ^{70,72,74}Ni and ^{76,78,80}Zn was performed at the RIBF facility of the RIKEN Nishina Center, Japan, as part of the first SEASTAR campaign. Radioactive isotopes were produced by the in-flight fission of a beam of ^{238}U ions incident on a 3 mm thick Beryllium target. After production, neutron-rich radioactive isotopes were selected and identified on an event-by-event basis using the BigRIPS separator. Selected isotopes of interest were focused onto the liquid hydrogen target of the MINOS device and γ-rays from inelastic (p, p') reactions were detected with the DALI2 array, consisting of 186 NaI crystals. Outgoing beam-like particles were identified using the ZeroDegree spectrometer. γ-rays produced in the reaction were Doppler corrected and the first 2^+ and 4^+ states in all the isotopes were identified. Detailed data analysis was performed including the implementation of algorithms that discriminate events where more than one particle was present. Using detailed `Geant4` simulations, exclusive cross-sections for inelastic proton scattering were obtained. Deformation lengths were deduced from the experimental cross-sections using the coupled-channel calculation code ECIS-97.

The deformations lengths of ^{72,74}Ni and ^{76,80}Zn were found to be fairly constant at a value of 0.8(2) fm, suggesting similar vibrational amplitudes, while the isomeric presence in the secondary beams of ^{70}Ni and ^{78}Zn allowed only lower limits for those two isotopes. By combining the deformation lengths with the known $B(E2;\ 0^+_{\rm gs} \rightarrow 2^+_1)$ values, the neutron-to-proton matrix element ratios, M_n/M_p, were obtained. A clear indication of the closed proton shell in the ^{72,74}Ni could be observed, as $M_n/M_p > N/Z$, indicating an increased contribution of the neutrons to the vibrational amplitude. For the case of ^{76,80}Zn, $M_n/M_p < N/Z$, indicating an open proton shell.

Zusammenfassung

Inelastische Streuung von ^{70,72,74}Ni und ^{76,78,80}Zn an einem Protonen-Target wurde am RIBF des RIKEN Nishina Centers, Japan, im Rahmen der ersten SEASTAR-Kampagne durchgeführt. Radioaktive Isotope wurden mittels In-Strahl-Spaltung eines ^{238}U-Strahls in einem Be-Target hergestellt. Die neutronenreichen radioaktiven Isotope wurden mit dem BigRIPS-Separator ausgewählt und auf Event-by-Event-Basis identifiziert. Die ausgewählten Isotope wurden auf das mit flüssigem Wasserstoff gefüllten MINOS-Target fokussiert und die Gamma-Strahlen wurden nach inelastischer (p, p')-Streuung mit dem DALI2-Spektrometer detektiert, das aus 186 NaI-Kristallen bestand. Gestreute Teilchen wurden mit dem ZeroDegre-Spektrometer identifiziert. Durch die Reaktionen auftretende Gamma-Strahlen wurden Doppler-korrigiert und die ersten angeregten 2^+ und 4^+-Zustände in allen Isotopen identifiziert. Eine detaillierte Daten-Analyse wurde durchgeführt, die die Implementierung von Algorithmen beinhaltete, die Ereignisse herausfilterten, bei der mehr als ein Teilchen in den Detektoren nachgewiesen wurde. Mithilfe detaillierter GEANT4-Simulationen wurden die exklusiven Wirkungsquerschnitte für inelastische Streuung bestimmt. Deformationslängen wurden aus den experimentellen Wirkungsquerschnitten durch gekoppelte-Kanäle-Rechnungen des ECIS97-Codes bestimmt.

Die Deformationslängen von ^{72,74}Ni und ^{76,80}Zn erweisen sich als relativ konstant bei 0.8(2) fm, was auf ähnliche Vibrations-Amplituden schließen läßt, während die Präsenz von isomeren Zuständen in ^{70}Ni und ^{78}Zn nur die Bestimmung eines Minimalwertes zuließ. Durch die Kombination der Deformationslängen mit den bekannten $B(E2;\ 0^+_{\rm gs} \rightarrow 2^+_1)$-Werten konnten die Verhältnisse der Neutron-zu-Proton-Matrixelemente, M_n/M_p, bestimmt werden. Einen klaren Hinweis der geschlossenen Protonenschale in ^{72,74}Ni

lieferte die Tatsache, dass $M_n/M_p > N/Z$, was auf eine höheren Anteil der Neutronen zur Vibrationsamplituden schließen lässt. Für ^{76,80}Zn war $M_n/M_p < N/Z$, was auf eine offene Protonenschale schließen lässt.

Erklärung zur Dissertation

Hiermit versichere ich, die vorliegende Dissertation ohne Hilfe Dritter nur mit den angegebenen Quellen und Hilfen angefertigt zu haben. Alle Stellen, die aus Quellen entnommen wurden, sind als solche kenntlich gemacht. Diese Arbeit hat in gleicher oder ähnlicher Form noch keiner Prüfungsbehörde vorgelegen.

Darmstadt, den 18. Juli 2016

Martha Liliana Cortés Sua

Acknowledgements

In first place, I would like to thank my supervisor, Prof. Pietralla for the opportunity to make my Ph.D in his group. His constant enthusiasm for physics discussions, and the unconditional support he provided me from the beginning, were fundamental during my PhD.

I would also like to thank Dr. Jürgen Gerl for welcoming me at the Gamma Spectroscopy group at GSI. Not only I learned a lot about detectors and techniques during my time there, but I also had a great time and acquired a lot of experience on experimental nuclear physics.

I am grateful to Dr. Volker Werner, for introducing me to the SEASTAR collaboration, and to Dr. Alexandre Obertelli and Dr. Pieter Doornenbal for welcoming me as part of it. I would like to particularly thank Pieter for all the support during the analysis, for reading and correcting parts of my thesis, for helping me with the German translation of the abstract, and for the nice times we have shared.

Many thanks also to all the members of the SEASTAR collaboration. It has been a fantastic experience to work with all of you. I really appreciate the nice combination of fun and work we had during my visit to RIKEN, the analysis workshops and each analysis meeting.

I also want to thank Hans-Jürgen, Magda, Henning, Ivan, Plamen, Frederic, Corinne, Tobias, Jelena, Michael, Tugba, Damian, Giulia, Cesar, Sudipta, and all the members and former members of the Gamma-Spectroscopy group of GSI for all the help, advise, and good times we have shared, specially during the AGATA campaigns. I want to particularly thank Henning for sharing the joy of football with me and, of course, for all the help with the electronics of the Finger detector, and Tugba for being there when I needed her.

I also acknowledge all the support I got from Dirk, Pico and Zsolt during the first part of my Ph.D. Special thanks to Dirk for lending me the best keyboard ever (in which I am writing these lines).

My gratitude also goes to the members of the Nuclear Physics group of TU Darmstadt: Christian, Waldemar, Pavlos, Johannes, and many others. In particular, I would like to thank Marc for being such a unique officemate and for all the fun times we have had. I thank as well all the secretaries of the Institute, in particular Giovanna, for the countless times they helped me with the administrative procedures.

Among all the wonderful people that have become my friends, I would like to give specially thanks to a couple. Thanks to Frank for all the support, for having the perfect words to cheer me up every time and for just being him. Many thanks to Michael, with whom I have shared from the first day of my Ph.D, for every physics discussion, for the patience, for showing me what good programming is and, in summary, for being such a great friend.

I also thank HiC for FAIR, HGS-Hire and the Federal Ministry of Education and Research (BMBF) for the academic and financial support they provided me at different stages of my Ph.D.

My gratitude also to my flatmates and ex-flatmates, in particular Stefano and Lara, and to all of my friends, specially Andrea, for the very good times we shared during my stay in Germany. Thanks to all of you these year are unforgettable.

Finalmente quiero agradecele a mi mamá, a mi papá, a mi tita y en especial a mi Nana por todo su amor y su apoyo incondicional. Sin ustedes, nada de esto, ni de lo anterior, ni de lo que viene, sería posible. Los quiero muchísimo.

CONTENTS

LIST OF FIGURES

LIST OF FIGURES

LIST OF TABLES

CHAPTER 1

INTRODUCTION

The atomic nucleus is a many-body system formed by protons and neutrons. It can be characterized by some basic properties as its radius, mass, angular momentum and parity. In addition, useful information on the internal structure can be obtained by the study of the characteristics of its excited states. The properties of the nucleus are determined by the competition of the strong force and the unified electroweak forces. It is well known that the main component of the nuclear force is an attractive central term which becomes repulsive at very short distances of nucleons. It is also known that this force is charge-independent to good approximation, which allows to describe protons and neutrons using the isospin formalism. In addition, the presence of a non-central term, known as the tensor force, contributes to various structural changes in nuclei far from stability with respect to the nuclei near the β-stability line (1). Although much progress has been made to develop models that can accurately predict properties of nuclei in a particular region of the nuclear chart, to this date, no unifying theory can explain every property of the nucleus in different mass regions.

In the most fundamental level, Quantum chromodynamics (QCD) governs the properties of quarks and gluons and is thus also responsible for the nucleon-nucleon interaction. Recent advances in the computation of nuclear properties based on QCD have been achieved using what is known as lattice-QCD (2). This approach requires very large computing power and up to now is only able to predict some properties of nuclei with $A \leq 4$ (3). *Ab initio* calculations, which derive global properties of the nucleus

based on the nucleon-nucleon interaction, have greatly advanced thanks to an improved understanding of the strong interaction and a significant improvement of the algorithms, allowing to perform calculations up to ^{48}Ca (4). One of the main drivers of these advances is the development of theories such as coupled-clusters (5). The use of this and other configuration-interaction techniques allows to extend the calculations to medium-mass isotopes. Heavier systems are studied using Density Functional Theory, based on self-consistent mean fields. In addition, phenomenological models, such as the shell model or the collective model, provide accurate descriptions of nuclear properties for different regions of the nuclear chart.

Investigation of nuclei far from the line of β-stability allow us to get a better insight in the nature of the nucleon-nucleon interaction and are a fundamental pillar of nuclear theories. The advent of Radioactive Ion Beam (RIB) facilities around the world opened the research on exotic isotopes and the study of the nuclear force for systems with extreme isospin values. In such facilities, RIBs are produced using either ISOL or in-flight techniques. Nowadays, facilities such as GSI (Germany), RIKEN (Japan), ISOLDE at CERN (Switzerland), GANIL (France), NSCL (USA), etc., are able to produce a great variety of RIBs to be studied with different techniques. In addition, future facilities such as FAIR (Germany), HIE-ISOLDE at CERN (Switzerland) and SPES (Italy), will increase the intensity and energy of RIBs to expand even further the boundaries of our knowledge about the nuclear interaction.

RIBs produced by the in-flight separation technique are characterized by their high luminosity as well as by the large velocities of the particles. Primary beam intensities higher than 10^{10} pps are expected to be achieved at FAIR and relativistic velocities imply that the radiation emitted by the isotopes has a very strong Doppler shift. Therefore, together with the development of the facilities, a huge development on the particle detectors, γ-ray detectors and target design are in progress around the world.

Examples of the advances in particle detectors are segmented Time-of-Flight (ToF) detectors such as the Finger detector (6, 7), capable of standing rates up to 10^6 pps without detriment in the ToF resolution. The major advances in γ-ray detection are the High-Purity segmented-Germanium tracking arrays AGATA (8) and GRETINA (9). Thanks to the precise position resolution of AGATA and GRETINA, the γ-ray resolution obtained after Doppler correction has been greatly improved, which in turn increases

the achievable sensitivity. Target developments have also been performed in order to increase the luminosity. Important examples of these improvements are the PreSPEC (10) and the MINOS (11) liquid-hydrogen targets. Using these targets, direct reactions, such as proton inelastic scattering or pick-up reactions, can be performed with a high luminosity and without losing resolution in the γ-ray spectrum after Doppler correction.

The use of RIBs has already proven to greatly contribute to expand our knowledge of the nuclear force. One of the most important results achieved is that the shell closures, which give rise to the magic numbers 2, 8, 20, 28, 50, 82 and 126 near the line of β-stability, change dramatically for extreme values of isospin. This so-called shell-evolution has been widely studied, in particular in the neutron-rich side of the nuclear chart. Experimental evidence suggests the appearance of new magic numbers $N = 32, 34$ in Ca isotopes (12, 13), although conclusions are still under debate (14). A new magic number $N = 16$ has also been proposed for ^{24}O (15), while the disappearance of the shell closure at $N = 28$ has been suggested for ^{42}Si (16). Apart from shell-evolution, RIBs have greatly contributed to nuclear astrophysics research. As an example, the accurate measurement of the lifetime of neutron-rich isotopes in the r-process path have allowed a better understanding of the observed element abundances (17). The further improvements on RIB facilities and detection systems will undoubtedly push nuclear physics research towards a better understanding of the fundamental forces of nature.

Of paramount importance to study the shell-evolution, are nuclei around doubly-closed shells, for example nuclei around ^{78}Ni ($Z = 28$, $N = 50$). This isotope can be approached by studying the Ni isotopic chain and the $N = 50$ isotonic chain, in particular ^{80}Zn, with two protons more than ^{78}Ni. Better insight in the nuclear structure of this region can be achieved by studying also other Zn isotopes. A well established way to determine the collectivity of a nucleus is to measure its quadrupole deformation. This is usually achieved by performing Coulomb-excitation experiments. Nevertheless, as this is an electromagnetic probe, it is only sensitive to the protons. In order to distinguish the relative importance of the contribution of protons and neutrons to the collectivity, a probe that is sensitive to both types of nucleons is needed. One of such probes is proton inelastic scattering.

In this thesis, the measurement of proton inelastic scattering for neutron-rich Ni and Zn isotopes in a liquid-hydrogen target is reported. The reaction cross sections

and their implication in the structure of the isotopes is discussed. The basic concepts needed in the analysis of the experiment are briefly presented in Chapter 2. Chapter 3 shows a general description of the technique used to produce the isotopes of interest as well as a detailed explanation of the setup used to perform the experiment. The data analysis is summarized in Chapter 4. After presenting the calibration of the different detectors of the setup, a summary of the characteristics of the beams used in the experiment is shown. The gates used to reduce the background and the Doppler correction procedure applied to the data are also shown in this Chapter. Chapter 5 shows the results obtained. It presents the reaction cross sections from which the contribution of protons and neutrons to the deformation can be extracted. A discussion of the implications of the results in the structure of the isotopes is also presented together with an analysis of possible improvements. Finally, Chapter 6 shows a summary of the thesis and a discussion on the future perspectives.

CHAPTER 2

BASIC CONCEPTS

This Chapter describes the basic concepts that motivated the experiment. Only a brief overview is presented and more detailed information can be found in the references given at the beginning of each section or along the text. In Section 2.1, the nuclear shell model and the collective model for vibrations and rotations are reviewed. Section 2.2 shows a brief overview of direct reactions and the particular characteristics of proton inelastic scattering. In Section 2.3, the concepts needed to characterize the contributions of protons and neutrons to the collectivity of an excited state are revised. Finally, Section 2.4 presents the current experimental status of the research on shell-evolution towards ^{78}Ni, namely for $Z = 28$ and $N = 50$.

2.1 Nuclear Models

Although the nucleons can be fundamentally described in terms of quarks and gluons, calculations of nuclear properties based on such fundamental theories are currently unfeasible for isotopes with more than 4 nucleons. Other techniques such as *ab-initio* calculations, where the nucleus is described based on an established two-nucleon potential, can only be performed for light isotopes. On the other hand, by putting together the experimental evidence collected along the years, it is possible to construct phenomenological models able to give a fairly good explanation of different nuclear

properties. Two of such models are the shell model and the collective model. Most of the information given in this section is taken from Refs. (18, 19).

2.1.1 The nuclear shell-model

One of the most remarkable results in nuclear physics is the nuclear shell model with spin-orbit interaction discovered by Maria Goeppert-Mayer (20) and Otto Haxel, Hans Jensen and Hans Suess (21). In this model, which was inspired by the atomic shell model, the nucleons are considered to be independent particles bound by a mean potential created by all the nucleons. The Hamiltonian of a system of nucleons can be approximated by a 2-body interaction as

$$H = T + V = \sum_{i=1}^{A} \frac{\boldsymbol{p}_i^2}{2m_i} + \sum_{i>k=1}^{A} V_{ik}(\boldsymbol{r_i} - \boldsymbol{r_j}), \tag{2.1}$$

where the first term of the sum represents the kinetic energy of the particles and the potential V has a repulsive component at short distances and an attractive part which extends up to the size of the nucleus. This Hamiltonian can be simplified by assuming that the particles move in a 1-body central potential created by the combined effect of all the 2-body interactions as

$$H = \sum_{i=1}^{A} \left[\frac{\boldsymbol{p}_i^2}{2m_i} + U_i(\boldsymbol{r}) \right] + H_{\text{residual}}, \tag{2.2}$$

where $U_i(\boldsymbol{r})$ is the nuclear mean potential introduced by the model and H_{residual} accounts for the deviations from the mean field approximation. $U_i(\boldsymbol{r})$ is typically obtained using Hartree-Fock methods. When using as a mean field a harmonic oscillator model or a more realistic Wood-Saxon potential together with a term of the form $-V_{so}\, \boldsymbol{l} \cdot \boldsymbol{s}$, the magic numbers 2, 8, 20, 28, 50, 82 and 126 are obtained. Nuclei with a magic proton or neutron number show abundant experimental evidence of their particular properties, showing that they form closed shells.

According to the shell model, the properties of the nucleus are determined by the valence nucleons. This idea gives accurate results for the ground state spin and parity of nuclei with one odd nucleon outside a magic shell. This model also gives a satisfactory, although not exact, explanation of other properties such as excited states and

electromagnetic moments (18, 19). Deviations can be explained by considering additional properties of the nuclei, which arise from collective motion of the protons and neutrons, as will be explained in the next section.

The partial success of the shell model opened up the further study of its validity for nuclei away from the stability line. In this respect, different studies have shown that the magic numbers are not valid across the entire chart of nuclei. Remarkable examples of the shell evolution are the disappearance of the $N = 28$ magic number in ^{42}Si (16) and the emergence of a new shell closure at $N = 16$ for exotic Oxygen isotopes (22). These changes of shell structure have been explained by the effect of the residual interactions, in particular a non-central component of the nuclear potential (1). More information on the structure of nuclei far from stability is needed in order to get an insight in the relevance of different terms of the nuclear force.

2.1.2 Collective models

As mentioned in the previous section, some properties of the nucleus, such as the large quadrupole moments observed for isotopes with $A > 150$, are better described using collective models. In this case, the nucleus is described as a liquid drop which can rotate or vibrate as a whole.

Two important parameters to take into account in the determination of the type and degree of collectivity of an even-mass nucleus are the energy of the first excited state and the reduced electric quadrupole transition probability between the ground state and the first excited state, $B(E2;\ 0^+_{\rm gs} \rightarrow 2^+_1)$. In a collective system, the excitation energy of the first excited state is much lower than the "classical" shell model prediction for a system of only very few valence nucleons and the $B(E2;\ 0^+_{\rm gs} \rightarrow 2^+_1)$ $= B(E2)\uparrow$ is much larger, indicating a coherent motion of the nucleons, which is considered as nuclear collectivity. The $B(E2)\uparrow$ value is directly related to the transition matrix element between the two states, $\langle \Psi_f | \hat{E2} | \Psi_f \rangle$ and thus to their wave functions.

2.1.2.1 Nuclear vibrations

In the vicinity of magic numbers, nuclei are usually treated as having a vibrational behavior. In this case, the average shape of the nucleus is considered to be spherical

while its instantaneous shape is not. These surface vibrations are described as

$$R(\theta,\phi) = R_0 \left[1 + \sum_{\lambda>1} \sum_{\mu=-\lambda}^{\lambda} \alpha_{\lambda\mu} Y_\lambda^\mu(\theta,\phi) \right], \tag{2.3}$$

where $R_0 = 1.2A^{1/3}$ is the average nuclear radius, Y_λ^μ are the spherical harmonics and $\alpha_{\lambda\mu}$ gives the amplitude of each vibrational mode. The lowest possible vibrational mode ($\lambda = 2$) can be seen as a single quadrupole phonon excitation and results in the first excited 2_1^+ state of the nucleus. There is no reason to prevent excitations corresponding to more than one phonon to occur. These multi-phonon states will correspond to higher nuclear levels. A two-quadrupole phonon excitation would give rise to a triplet of states with $l = 0, 2, 4$ and positive parity, while a single octupole phonon excitation ($\lambda = 3$) would generate a 3^- state.

In vibrational nuclei, the electric quadrupole moments have small values, which are comparable to the single particle values. The magnitude of the $B(E2)\uparrow$ values for higher excited states is expected to be proportional to the number of phonons that give rise to the state. Additionally, the energy of each level is also expected to be proportional to the number of phonons, thus the model predicts $E(4_1^+)/E(2_1^+)$ =2. The experimental evidence suggest $E(4_1^+)/E(2_1^+)$ ≈2.2 (19), showing that this model is only an approximation.

2.1.2.2 Nuclear rotations

Nuclear rotations are only possible for nuclei with static deformation. The lowest shape component is a quadrupole deformation. There can also be octupole and hexadecapole shapes. Nuclei with quadrupole shapes have been observed all along the nuclear chart, in particular for the ground-state bands of isotopes with $150 < A < 190$. In the case of a quadrupole deformation, the nuclear radius can be written as

$$R(\theta,\phi) = R_0 \left[1 + \sum_{\mu} \alpha_\mu Y_2^\mu(\theta,\phi) \right], \tag{2.4}$$

where $R_0 = 1.2A^{1/3}$ is the average radius, Y_2^μ are spherical harmonics of order 2 and α_μ are the expansion coefficients which measure the deformation. It is convenient to

write the five α_μ in terms of three Euler angles and two intrinsic variables as

$$\begin{aligned} \alpha_0 =& \beta_2 \cos\gamma \\ \alpha_2 = \alpha_{-2} =& \beta_2 \sin\gamma. \end{aligned} \tag{2.5}$$

In this way, β_2 represents the quadrupole deformation and γ represents the degree of axial symmetry. Following the Lund convention, if $\beta_2 > 0$ and $\gamma = 0^\circ$ one obtains and axially symmetric prolate nucleus. On the other hand $\beta_2 > 0$ and $\gamma = 60^\circ$ results in an axially symmetric oblate nucleus. In a different convention, $\beta_2 > 0$ is assigned to prolate nuclei and $\beta_2 < 0$ to oblate nuclei, while γ varies between 0° for an axially symmetric nucleus to 30° for an axially asymmetric one.

In a axially symmetric deformed nucleus, the $B(E2;\ 0^+_{\rm gs} \rightarrow 2^+_1)$ value is proportional to the square of the intrinsic quadrupole moment and thus, to the deformation parameter as

$$\beta_2 = \frac{4\pi}{3ZeR_0^2}\sqrt{B(E2;\ 0^+_{\rm gs} \rightarrow 2^+_1)}. \tag{2.6}$$

Assuming that the nucleus is a rotating object with a fixed moment of inertia, the rotational energy of the nucleus, which gives rise to the excited states, is proportional to $I(I+1)$, where I represents the total angular momentum of the nucleus. This in turn results in $E(4^+_1)/E(2^+_1)$ =3.33. If one considers that the cylindrical symmetry is broken, resulting in an axially asymmetric, or $\gamma-$soft, nucleus one obtains $E(4^+_1)/E(2^+_1)$ =2.5.

Deviations on $E(4^+_1)/E(2^+_1)$ for axially symmetric rotors have been measured. In order to give a more accurate description of these nuclei, models which take into account the rotational bands appearing on top of vibrational states, such as the confined β-soft rotor model (23), are needed.

2.2 Direct reactions

A direct reaction between two nuclei occurs when the incident particles interact primarily with the surface of the target nucleus and only one or few valence nucleons participate. This situation occurs when the de Broglie wavelength associated to the energy of the incoming particle is at least in the order of the nucleon size ($\approx$ 1 fm). In direct reactions no compound nucleus is formed, and the interaction is expected to take place in a time comparable with the time it takes for a particle to cross the nucleus. The scattering amplitudes are calculated by means of potential scattering

mechanisms which involve only few degrees of freedom. Examples of direct reactions are inelastic scattering, pick-up and stripping, each one of which allows the study of different nuclear properties. In particular, proton inelastic scattering is a probe that can be used to study collective states and that is sensitive to both protons and neutrons. Coulomb excitation, in which the interaction takes place between the Coulomb fields of the projectile and the target, is a powerful tool to study the low-lying excited states of a nucleus and the proton collectivity in these states. The main Refs. used in this Sections are (24, 25, 26).

2.2.1 Proton inelastic scattering

Proton inelastic scattering has been used, for example, to study the neutron and proton transition densities for ^{32}S (27) and to study the neutron halo in ^{6}He (28, 29). Such studies rely on the fact that, contrary to Coulomb excitation, proton inelastic scattering is able to yield information on both the proton and the neutron contributions to a nuclear excitation. Nevertheless, while the Coulomb force is exactly known, the analysis of proton inelastic scattering has to rely on nuclear models, either phenomenological or microscopic, of the interaction potential.

2.2.1.1 The optical model

In the optical model the scattering potential is represented in terms of a complex potential which has a limited number of parameters. A standard form of this model is given by

$$\begin{aligned}
U_{opt}(r) =& V_C(r) && \text{a Coulomb term} \\
& -V_v f_V(r) && \text{a real volume term} \\
& -iW_v f_W(r) && \text{an imaginary volume term} \\
& +V_s g_V(r) && \text{a real surface term} \\
& -iW_s g_W(r) && \text{an imaginary surface term} \\
& +d_{s.o}\vec{l}\cdot\vec{s}V_{so}h_{v_{so}}(r) && \text{a real spin-orbit term} \\
& +id_{s.o}\vec{l}\cdot\vec{s}W_{so}h_{W_{so}}(r) && \text{an imaginary spin-orbit term,}
\end{aligned} \tag{2.7}$$

where the $d_{s.o} = (\hbar/m_\pi c)^2 \approx 2$ fm^2 and m_π is the pion mass. The Coulomb term is given by the interaction of a point-like charge with a uniformly charged sphere of

radius $R_C = r_C A^{1/3}$,

$$V_C(r) = \begin{cases} \left(\frac{3}{2} - \frac{r^2}{2R_C^2}\right) Z_p Z_t e^2/R_C, & \text{if } r \leq R_C \\ Z_p Z_t e^2/r, & \text{if } r > R_c, \end{cases} \tag{2.8}$$

where $Z_p = 1$ and Z_t are the projectile and target charge, respectively. The form factors are given by

$$f_i(r) = \frac{1}{1 + \exp[(r - R_i)/a_i]}, \tag{2.9}$$

$$g_i(r) = -4a_i \frac{d}{dr} f_i(r) = 4 \frac{\exp[(r - R_i)/a_i]}{1 + \exp[(r - R_i)/a_i]}, \tag{2.10}$$

$$h_i(r) = -\frac{1}{r} \frac{d}{dr} f_i(r) = \frac{1}{r a_i} \frac{\exp[(r - R_i)/a_i]}{(1 + \exp[(r - R_i)/a_i])^2}, \tag{2.11}$$

where $i = V, W, s, sw$ or so, sow for the volume real, volume imaginary, surface real, surface imaginary, spin-orbit real and spin-orbit imaginary potentials, respectively. The real part of the optical potential describes the elastic scattering of the particle, while the imaginary part takes into account the inelastic channels through absorption.

The values of the parameters needed by the optical model can be calculated in two different ways. The first possibility is to fit the parameters to experimental data in order to reproduce the observed cross sections of elastic scattering. It has been observed that these parameters change slowly for different isotopes over a wide range or proton energies. This gives rise to empirically parametrized optical models. Examples of such parametrization are the Beccheti-Greenless model (30), which is valid for $A > 40$ and energies < 50 MeV, and the Koning-Delaroche model (KD02) (31), valid for energies between 1 keV and 200 MeV.

The second possible way to obtain the parameters of the optical model is by performing a microscopic calculation based solely on the nuclear matter calculations. This approach was developed by Jeukenne, Lejeune and Mahaux (JLK) (32). In this model, a form of the nucleon-nucleon interaction, V_{nn}, is considered together with calculated nuclear densities to obtain the interaction potential, $U(r)$, as

$$U(r) = \int \rho(r') V_{nn}(|r - r'|) d^3 r', \tag{2.12}$$

where $\rho(r)$ represents the distribution of nuclear matter and the integral runs over the full nuclear volume.

Comparisons between the results obtained with the phenomenological parametrization and the JLK calculations have shown discrepancies in the results. Such discrepancies have been attributed to a possible difference between the neutron and proton distributions for neutron-rich isotopes, which is not taken into account by the form factors of the parametrized models (25, 33)

2.3 Neutron-to-proton matrix elements ratio

The proton and neutron multipole transition matrix elements, M_n and M_p, can be used to determine the contribution of each type of nucleon to the excitation of a nuclear state. The description of these matrix elements is taken mainly from Refs. (33, 34).

The proton and neutron matrix elements are defined as

$$M^{\lambda}_{n(p)} = \int \rho_{n(p)}(r) r^{\lambda-2} dr, \tag{2.13}$$

where $\rho_{n(p)}$ are the neutron (proton) transition densities and λ is the multipolarity of the transition. In the particular case when the transition under study is from a 0^+ state to a 2^+ state, the matrix element M_p is directly related to the $B(E2)\uparrow$ value as $B(E2)\uparrow = M_p^2$. In order to probe both the contribution of the neutrons and the protons to the excitation a hadronic probe, such as proton inelastic scattering, is needed.

The neutron-to-proton matrix element ratio, M_n/M_p, can be obtained by comparing the excitation probabilities of a hadronic probe and an electromagnetic probe, such as Coulomb excitation. From a phenomenological approach, this can be achieved using the Bernstein approach (34) as

$$\frac{M_n}{M_p} = \frac{N}{Z}\left[\frac{\delta_{p,p'}}{\delta_C} + \frac{Zb_p}{Nb_n}\left(\frac{\delta_{p,p'}}{\delta_C} - 1\right)\right]. \tag{2.14}$$

The coefficients b_p and b_n represent the strength of the interaction of protons with protons and protons with neutrons respectively and $\delta_{p,p'}$ and δ_C are the deformation lengths obtained with the proton inelastic scattering and the Coulomb excitation measurements respectively. The values of b_p and b_n depend on the energy of the incoming beam and are reported to vary between $b_n/b_p = 3$ for 10-50 MeV protons to $b_n/b_p = 0.95$ for 1 GeV protons. The deformation length δ_C is directly related to the β_2 parameter, and thus to $B(E2)\uparrow$, as

$$\delta_C = \beta_2 R_0 A^{1/3}, \tag{2.15}$$

while $\delta_{(p,p')}$ is related to the vibrational amplitude of the state $\alpha_{\lambda\mu}$ in equation 2.3

In the collective model it is usually assumed that the nucleus is a homogeneous proton-neutron fluid. This gives rise to a pure isoscalar excitation where $M_n/M_p = N/Z$. A significant deviation of this prediction is an indicator of an isovector component of the excitation. Such deviations are expected to occur near closed-shells where the protons or the neutrons form a spherical shell and contribute to the excitation differently from a simple proportionality to their numbers. Although core polarization restores to a large extent the isoscalar character of the excitation (35), values of M_n/M_p significantly different from N/Z give clear indications of shell effects.

2.4 Shell evolution for the $Z = 28$ and $N = 50$ chains

This section summarizes the current status of the research performed in Ni isotopes and $N = 50$ isotones. Some of the information was taken from Ref. (36) and references within. The discussion has been extended using recent experimental results.

The known Ni isotopic chain (Z =28) ranges from the doubly-magic ^{48}Ni to ^{79}Ni (37, 38), passing also the doubly-magic ^{78}Ni. While ^{48}Ni is a candidate of two-proton radioactivity, ^{78}Ni is an important waiting point in the r-process path. Thus the study of this chain offers a great insight in nuclear structure and astrophysics (36).

Figure 2.1 shows the experimental values on the $E(2_1^+)$ and $B(E2)\uparrow$ values of the Ni isotopes as a function of the neutron number. The increase in the excitation energy of the 2_1^+ state clearly shows the presence of a shell closure at $N = 28$ and a sub-shell closure at $N = 40$. The $B(E2)\uparrow$ values show the opposite trend: minimum values are reached at $N = 28$ and $N = 40$, while the maximum is reached for the middle of the shell. This behavior is consistent with a seniority scheme (39) in the fp shell. According to this model, which attributes the properties of the excitations solely to the number of unpaired nucleons, the $B(E2)\uparrow$ values follow a parabola between the shell closures, which can be expressed as

$$B(E2;\ 0^+_{\rm gs} \rightarrow 2^+_1) = c(\pi fp, \nu fp)F(1-F), \tag{2.16}$$

where $c(\pi fp, \nu fp)$ represents the strength of the proton-neutron interaction in the fp shell and $F = (N-N_1)/(N_2-N_1)$ is the fractional filling of an nucleus with N neutrons between the shell closures given by N_1 and N_2 (19).

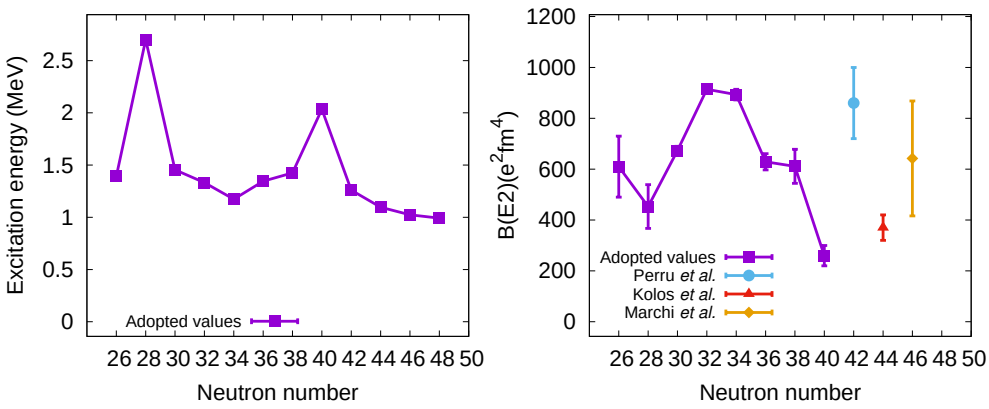

Figure 2.1: Systematics of $E(2_1^+)$ and $B(E2;\ 0_{gs}^+ \rightarrow 2_1^+)$ values for the $Z = 28$ isotopic chain. The adopted values are taken from Ref. (40). The other $B(E2;\ 0_{gs}^+ \rightarrow 2_1^+)$ values are taken from Refs. (41, 42, 43).

Although the $B(E2)\uparrow$ values between $N = 28$ and $N = 40$ seem to follow reasonably well the seniority scheme, this is not the case for $N > 40$. The $B(E2)\uparrow$ value for ^{70}Ni reported in Ref. (41) is much larger than expected by different shell model calculations (44).

This was interpreted as an enhancement of the core polarization for this isotope and a consequent weakening of the $N = 50$ shell closure. Nevertheless, the values reported for ^{72,74}Ni are considerably lower and seem to contradict the ^{70}Ni measurement. These values are also in better agreement with shell model calculations and point to the persistence of the $N = 50$ shell gap (42, 43). Further studies on the Ni isotopes heavier than ^{68}Ni and in particular on ^{78}Ni are necessary to obtain firm conclusions about this magic number.

The known even-even isotonic $N = 50$ chain goes from the the doubly-magic ^{78}Ni to the self-conjugated doubly-magic ^{100}Sn (45). Although these two *a priori* doubly-magic isotopes have been synthesized using the in-flight separation technique, not enough statistics have been collected to study their excited states.

Figure 2.2 shows the adopted values of the excitation energy and the $B(E2)\uparrow$ values for the $N = 50$ isotones as function of the proton number. From the excitation energies it can clearly be seen that the sub-shell closure at $Z = 40$ is present. Although a slight increase in excitation energy is observed towards $Z = 28$, data on ^{78}Ni is still missing. The $B(E2)\uparrow$ values show a parabolic behavior between $Z = 30$ and $Z = 40$, consistent

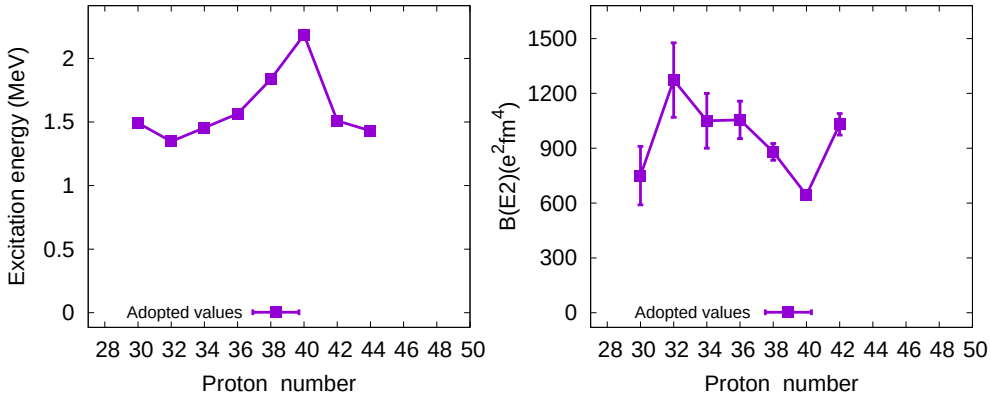

Figure 2.2: Systematics of $E(2_1^+)$ and $B(E2;\ 0_{\rm gs}^+ \rightarrow 2_1^+)$ values for the $N = 50$ isotonic chain. The adopted values are taken from NNDC (46).

with the seniority scheme. This behavior points to the conservation of the $N = 50$ shell gap towards ^{78}Ni.

In order to help the study of the shell structure in the region around ^{78}Ni, the contributions of the protons and the neutrons to the collectivity were studied by means of γ-ray spectroscopy performed after proton inelastic scattering. Along the $Z = 28$ shell closure, ^{70,72,74}Ni were studied. By comparing the proton inelastic scattering cross sections, the question of the increased collectivity measured for ^{70}Ni can be addressed, as well as the effect of the increasing number of neutrons in the collective behavior of the Ni isotopes. Along the Zn isotopic chain, ^{76,78,80}Zn were measured. The comparison of the cross sections between the isobars ^{74}Ni and ^{76}Zn, can shed light in the importance of the proton shell closure on the excitation, while the cross section measured for ^{80}Zn, with a closed $N = 50$ neutron shell, serves as a comparison of the collectivity between a proton and a neutron closed shell when approaching ^{78}Ni.

CHAPTER 3

EXPERIMENTAL SETUP

Radioactive Ion Beams (RIBs) offer a unique opportunity to explore more exotic nuclei and thus broaden our knowledge of the atomic nucleus. Two different techniques to produce and separate RIBs have been developed: The Isotope Separation On-Line (ISOL) and the In-Flight (IF) techniques. In the ISOL technique, a primary beam of protons, deuterons or alpha particles collides with a thick target, causing it to fragment or fission. The target in this case can be up to 13 cm long (47). The reaction products are removed from the target by diffusion and passed through an ion source. The radioactive isotopes are then selected using an electromagnetic separator. Because of the low energies, a post-acceleration stage may be needed to perform secondary reaction studies. Alternatively, β-decay studies can be performed. ISOLDE at CERN (48) and the future SPES at Legnaro National Laboratory (49) are examples of facilities using the ISOL technique. In the IF separation technique, a target in the order of 1 g/cm^2 is used to induce fragmentation or fission of the projectile nuclei. The reaction fragments are traveling through the target with a velocity similar to the velocity of the incoming beam and no further acceleration is needed. An electromagnetic separator is used to select the isotopes of interest. Examples of facilities using the IF separation technique are GSI in Germany (50), RIKEN in Japan (51), NSCL in USA (52) and Ganil in France (53). Section 3.1 describes some general aspects of the IF separation technique, which was used to perform the experiment reported in this thesis. The setup used for the experiment is described in Section 3.2.

3.1 In-flight separation technique

3.1.1 Production

In the IF separation technique, a high energy beam is broken to smaller pieces in a target in the order of 1 g/cm^2 by means of fragmentation or fission. In the fragmentation process, the peripheral interaction of the projectile with a target nucleus causes some nucleons to be removed. Coulomb deflection and the nuclear recoil of the ion are small so that due to the large initial velocity all the products are focused into a narrow cone (54, 55). The mass, charge and velocity distributions of the residues have been described in microscopic nucleon-nucleon scattering models or the macroscopic abrasion framework (56, 57). The target is used to induce the fission of the projectile. This mechanism populates predominantly neutron-rich isotopes. The angular distribution of the nuclei created in this process is essentially isotropical in the rest frame of the projectile. If the projectile nucleus is moving with a kinetic energy that is large compared to the fission recoil, the products can be collected and separated using an electromagnetic separator similar to those used for projectile fragments (54, 55). A Pb target is usually employed to perform Coulomb induced fission, in which medium-to-heavy-mass isotopes as Sn, Te and Xe are produced. A Be target is preferred for fragmentation or fragmentation-fission reactions where lighter isotopes, as Zn and Ni can be produced. Reaction cross sections for different beam and target combinations can be found in Reference (58). The IF fission technique has been widely used to study neutron-rich isotopes since the nineteen-nineteens (59, 60).

3.1.2 Separation

After the primary reaction takes place, the products are separated using an achromatic magnetic separator. These devices are based on the fact that when charged particles with different mass-to-charge ratio (A/Q) and different momentum (p) cross a magnetic field, they will follow different trajectories. If the magnetic field (B) is assumed to be homogeneous and perpendicular to the velocity of the particles, the trajectories can be described by

$$B\rho = \frac{p}{Q} = \frac{\gamma m v}{Q} = \gamma\beta\frac{A}{Z}\frac{cu}{e}, \tag{3.1}$$

where ρ is the radius of curvature of the path followed by the particle, $v = c\beta$ is the velocity of the particle, $m = Au$ is the mass of the particle and $\gamma = 1/\sqrt{1-\beta^2}$. Here, c is the speed of light and $u = 931.5$ MeV/c^2 is the atomic mass unit. The quantity $B\rho$ is defined as the magnetic rigidity and has the unit Tesla-meter (Tm). As shown by the Equation 3.1, a dipole magnet can be used to disperse the beam particles and select only a certain range of magnetic rigidities. In practice, most separators use at least two dipoles in order to refocus the particles after a $B\rho$ selection has been done. If the refocusing of the particles is done to a single point regardless of their momentum, the separator is called an achromatic separator (61). The plane between the dipoles is called a dispersive plane as isotopes with the same A/Q will be placed at different positions depending on their momentum. A detailed description of the trajectory of a particle in a magnetic field can be obtained using ion-optics based on transfer matrices (62). According to this formalism, a first-order approximation for the horizontal position of a particle after passing through a magnetic stage of a fragment separator is given by

$$x = (x|x)\, x_0 + (x|a)\, a_0 + (x|\delta)\, \delta, \tag{3.2}$$

where x and a represent the position and angle of the particle in the horizontal plane and the subscript "0" refers to the original coordinates of the ion. δ denotes the relative momentum deviation with respect to the central trajectory. The coefficients $(x|x)$, $(x|a)$ and $(x|\delta)$ represent the magnification, the angular dependence and the momentum dispersion of the magnetic stage, respectively. If the magnetic stage results in a focal plane, the term $(x|a)$ vanishes (63, 64). In a standard fragment separator, in addition to bending dipoles, quadrupole magnets are needed to focus the beam in both x and y direction, and higher order multipole magnets can be used to correct ion-optical aberrations.

Further selection can be achieved by inserting a wedge-shaped degrader between two dipoles. The specific energy loss of a heavy ion in matter can be described by the Bethe-Bloch formula

$$-\frac{dE}{dx} = \frac{4\pi e^2 Z^2}{m_e v^2} N_m B, \tag{3.3}$$

where

$$B = Z_m \left[\ln \frac{2m_e v^2}{I} - \ln\left(1 - \frac{v^2}{c^2}\right) - \frac{v^2}{c^2} \right]. \tag{3.4}$$

In these equations, N_m and Z_m are the number density and the atomic number of the target matter, m_e and e are the electron rest mass and its charge, respectively. The parameter I represents the average excitation and ionization potential of the material (65). From Equation 3.3, it can be seen that in a good approximation, the energy loss (ΔE) depends on the atomic number of the projectile as Z^2. Thanks to this, isotopes with a different charge will have a different velocity after passing the degrader. This change in velocity leads to a change in magnetic rigidity for isotopes that have the same A/Q, allowing them to be separated in a second dipole stage. The degrader is wedge-shaped in order to take into account the dependence of the energy loss on the velocity and to keep the achromatic condition: Isotopes with a higher velocity will pass a thicker piece of matter than those traveling with low velocity. This separation method is known as the $B\rho$-ΔE-$B\rho$ separation method. As a secondary beam composed of different isotopes may still pass the two magnetic stages, it is required to determine Z and A/Q for each isotope on an event-by-event basis. Examples of magnetic separators are the FRS at GSI (50), RIPS and BigRIPS at RIBF (51), the A1900 at NSCL (52) and LISE at Ganil (53).

3.1.3 Identification

Usually, the atomic number of the particles is determined using an ionization chamber. As can be seen from Equation 3.3, the energy loss of an ion after a certain distance depends on its charge and its velocity. When an ion deposits energy in the gas volume of an ionization chamber, electron-hole pairs are created. The number of created free electrons is proportional to the energy deposited by the particle in the gas (65, 66). By applying an electric field, the electrons can be collected. After electronic processing, a measurement of the energy loss is obtained. As the energy loss in the gas depends on its density, temperature and pressure, changes can affect the measurements. According to Equation 3.3, to extract the atomic number of the particle, it is also necessary to know its velocity.

The determination of the velocity is performed by measuring the ToF of the particle between two points separated by a known distance along the beam line. This is usually achieved by placing fast plastic scintillators in the middle and final focal planes of the separator. When a charged particle crosses a piece of plastic scintillator, it loses energy

by exciting electrons to higher energy levels. For the case of a plastic scintillator, the de-excitation takes places through molecular levels, producing a flash of light (65, 66). If the plastic scintillator is coupled to a device which can convert the light back to electrons and can amplify the signal, such as a photomultiplier (PMT), an electric pulse is created and can be further analyzed. The number of light photons created in the plastic is proportional to the energy deposited by the particle in the material. By using a PMT or any device that keeps the linearity, the energy loss in the plastic can be determined. In addition, plastic scintillators show an extremely fast response to the passage or radiation, with pulse widths of few nanoseconds. Because of this, the electric pulse can also be used to resolve the time of interaction of the particle. By subtracting the time of interaction in each scintillator and taking into account the distance between them, the velocity of the particles is obtained.

To determine A/Q, Equation 3.1 can be used. Solving for A/Q results in

$$\frac{A}{Q} = B\rho \frac{1}{\gamma\beta} \frac{e}{cu}. \tag{3.5}$$

The value of the magnetic field can be accurately measured using a Hall probe, and β and γ can be determined using the ToF measurement as described above. To accurately determine the radius of curvature of the trajectory of each particle, it is possible to use the definition of δ,

$$\delta = \frac{p - p_o}{p_0}, \tag{3.6}$$

where p is the momentum of the particle and p_0 is the momentum it would have for the central trajectory. By recalling that $B\rho = p/q$, Equation 3.6 can be transformed in an expression for the magnetic rigidity

$$B\rho = B\rho_0 \left(1 + \delta\right), \tag{3.7}$$

where ρ_0 corresponds to the length of the central trajectory. By replacing δ with Equation 3.2,

$$B\rho = B\rho_0 \left[1 + \frac{x - (x|x)\, x_0 - (x|a)\, a_0}{(x|\delta)}\right] \tag{3.8}$$

is obtained. From the above equation, it is visible that it is necessary to measure the position of the particle along the separator as well as its angle in the horizontal direction. To achieve this, high-resolution position detectors are inserted in the different focal planes of the separator. In general, the detectors used for these measurements

are gas detectors similar to ionization chambers. The particular detector which is used depends on the properties of the beam and the facility. The measurement of A/Q is then a combination of position and ToF measurements.

The RIBs produced with the IF technique can be used to perform different reactions, such as Coulomb excitation, secondary fragmentation or inelastic scattering, in a secondary target. By surrounding the target with an array of γ-ray detectors, the de-excitation of the projectile and/or the target nuclei can be measured and different properties of these nuclei can be extracted. After the reaction takes place, the outgoing fragments require further identification. This identification can be performed with a magnetic spectrometer or any device capable of measuring the outgoing velocity of the particles, its charge, and mass. The next section gives an overview of in-beam γ-ray spectroscopy for RIBs. The particular characteristics of the experimental setup used to perform the measurements reported in this thesis are described in the Section 3.2.

3.1.4 In-beam γ-ray spectroscopy

After a reaction takes place, γ-rays are emitted by the residual particles traveling with a large velocity. The energy measured by a γ-ray detection system placed around the target, E_γ, will be Doppler shifted with respect to the original de-excitation energy, $E_{\gamma 0}$. This Doppler shift can be corrected using the formula

$$\frac{E_\gamma}{E_{\gamma 0}} = \frac{\sqrt{1-\beta^2}}{1-\beta\cos\vartheta}, \tag{3.9}$$

where ϑ is the γ-ray emission angle in the laboratory frame of reference. If the scattering angle of the outgoing particles is small, ϑ is in good approximation equal to the angle at which the γ-ray is detected. The uncertainty in $E_{\gamma 0}$ is given by

$$\begin{aligned}\left(\frac{\Delta E_{\gamma 0}}{E_{\gamma 0}}\right)^2 = &\left(\frac{\beta\sin\vartheta}{1-\beta\cos\vartheta}\right)^2(\Delta\vartheta)^2 + \\ &\left(\frac{\beta-\cos\vartheta}{(1-\beta^2)(1-\beta\cos\vartheta)}\right)^2(\Delta\beta)^2 + \\ &\left(\frac{\Delta E_{int}}{E_\gamma}\right)^2.\end{aligned} \tag{3.10}$$

The first term in the right of Equation 3.10 represents the the uncertainty due to the detection angle, which is mainly correlated with the solid angle covered by the detectors. The second term shows the uncertainty on the velocity, which is due to the

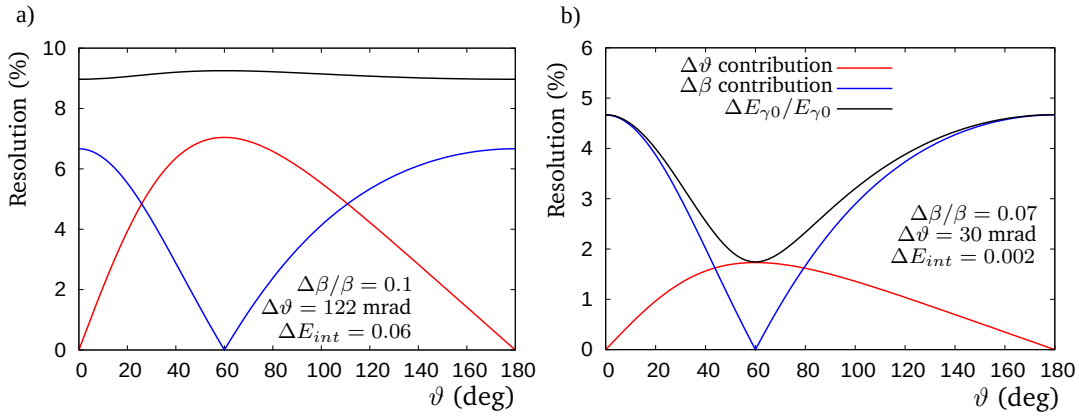

Figure 3.1: Doppler broadening of the detected γ-rays. Panel a) shows the results obtained using parameters typical for scintillators-based arrays, while Panel b) shows the result obtained taking parameters found in a Ge-based array. It was assumed $\beta = 0.5$.

slowing down and straggling in the target. The last term represents the intrinsic energy resolution of the detection system, which depends only on the type of detector used. Figure 3.1 shows the Doppler broadening due to each one of these contributions as a function of ϑ assuming $\beta = 0.5$ and a $E_{\gamma 0} = 1.33$ MeV. Panel a) of the Figure shows the results obtained using $\Delta\beta/\beta = 0.1$, $\Delta\vartheta = 122$ mrad and an intrinsic resolution of the detectors of $\Delta E_{int} = 0.06$, which are typical values for a scintillator-based array. Panel b) shows the results obtained when $\Delta\beta/\beta = 0.07$, $\Delta\vartheta = 30$ mrad and $\Delta E_{int} = 0.002$, which are values found in segmented Ge-based arrays. It can be seen from the plot that at lower angles the broadening arising from $\Delta\vartheta$ is small, reaching its maximum around 60°. On the other hand, around the same angle, the broadening due to the uncertainty in β is minimal. The resolution achieved at different angles can be significantly different. Due to the Lorentz boost, most of the γ-rays will be emitted in forward directions (low angle in the laboratory frame). Thus, a good efficiency and angular resolution is desirable in the forward-angle detectors.

Further limiting effects on the achievable resolution are introduced because of the lifetimes of the excited states (67). Due to the use of thick targets, the determination of the velocity is affected by possible energy losses of the particle inside the target before the γ-decay. In order to minimize this effect, the velocity used to perform the Doppler correction should be calculated back from the velocity measured after the target, taking into account the lifetime and the energy loss of the reaction products. The lifetime of

the excited states can also cause a shift on the position along the beam line where the particle decays. The position of emission of the γ-ray along the beam line is usually taken as the center of the target and its accuracy is limited by the target thickness. When a long lifetime is present, using the target position to calculate the emission angle of the γ-rays causes a smearing of the peaks (67, 68).

Although the use of thick targets generates an increase in the Doppler broadening of the peaks, low-Z targets maximize the number of reaction points per energy loss, increasing the luminosity. In order to take full advantage of these targets while keeping a reasonably good energy resolution, a vertex tracker can be placed around the target to have a more accurate measurement of the interaction position. This principle is exploited by the MINOS device (11), as will be shown in Section 3.2.4.

3.2 SEASTAR setup

The proton inelastic scattering experiment on Ni and Zn isotopes was performed as part of the first SEASTAR campaign (69) at the Radioactive Isotope Beam Factory (RIBF) (70), which is operated by the RIKEN Nishina Center (RNC) and Center of Nuclear Study (CNS) of the University of Tokyo. SEASTAR stands for "Shell Evolution And Search for Two-plus energies At the RIBF" and aims to perform a systematic search of new 2_1^+ energies in a wide range of neutron-rich nuclei between Ar and Zr.

In the first SEASTAR campaign, a ^{238}U beam was accelerated to 345 MeV/u and impinged on a 3 mm thick ^{9}Be target to produce a cocktail of secondary isotopes via in-flight fission. The isotopes produced in the primary target entered the BigRIPS isotope separator (51), where selection and identification of each ion on an event-by-event basis was performed using the $B\rho$-ΔE-$B\rho$ method. Selected isotopes were focused on the liquid Hydrogen target of the MINOS device (11), where reactions took place. The target was placed in the center of the DALI2 array (71), consisting of 186 NaI crystals in order to detect the γ-rays emitted by the isotopes after the reactions. The outgoing particles were identified using the ZeroDegree spectrometer (51). The γ-rays emitted after the reaction were corrected to take into account the Doppler shift using the velocity measured by the BigRIPS and ZeroDegree separators. The corrected γ-ray spectra were then fitted with a simulated response function of the DALI2 array in order to extract the proton inelastic scattering cross sections for each isotope.

This Section gives a detailed description on the experimental setup used. The analysis of the data will be described in Chapter 4.

3.2.1 Production and acceleration

Figure 3.2 shows the schematic view of the accelerator complex of the RIBF. Three different initial acceleration modes can be used: The Azimuthally Varying Field (AVF) injection mode, used exclusively for light ions; the variable-energy mode used for medium mass isotopes; and the fixed-energy mode, used for the acceleration of heavy ions such as Xe and U (72). For the SEASTAR campaign, the fixed-energy mode was used. A high intensity ^{238}U beam was produced by injecting 28 GHz microwaves in a superconducting electron cyclotron resonance (SC-ECR) ion source (73, 74). The beam was then extracted from the source and accelerated using the RIKEN Heavy Ion LINAC 2 (RILAC2) which accelerated the ions to 0.67 MeV/u (75). Afterwards, the beam was accelerated in four consecutive cyclotrons: The RIKEN Ring Cyclotron (RRC), which accelerated the ions to 11 MeV/u; the Fixed-frequency Ring Cyclotron (fRC) after which the ions had an energy of about 50 MeV/u; the Intermediate-stage Ring Cyclotron (IRC), and the Superconducting Ring Cyclotron (SRC), which accelerated the U to 345 MeV/u. As shown in Figure 3.2, two charge strippers were used in

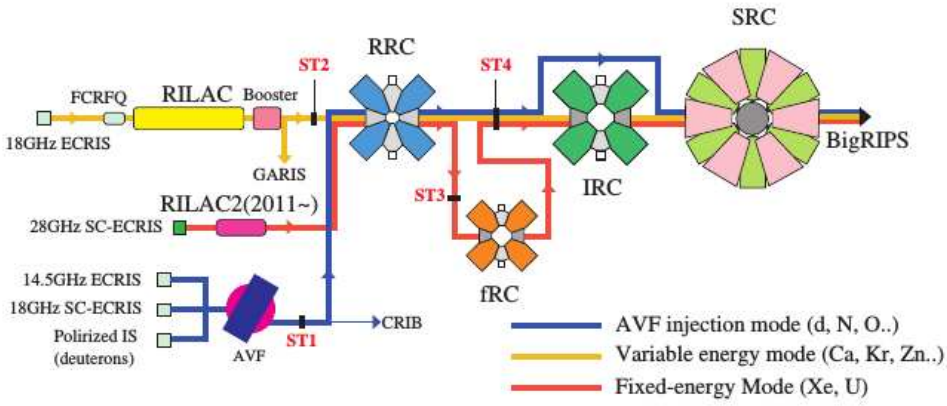

Figure 3.2: Accelerator complex of the RIBF. For the fixed-energy mode, the 28 GHz SC-ECR Ion Source was used together with the RILAC2 injector. Ions are then further accelerated using four cyclotrons to reach an energy of 345 MeV/u. In the figure, ST1-ST4 represent charge strippers. The image is taken from Reference (72).

the fixed-energy mode, one before and one after the fRC. The first of these strippers was a Helium gas stripper (76, 77), which guaranteed a charge state of the U ions of 69^+ at the entrance of the fRC (77). The second stripper was a rotating Beryllium disk (78), which guaranteed a charge state of 86^+ at the entrance of the IRC. After exiting the SRC, the ^{238}U beam was delivered to the BigRIPS separator, where a 3 mm thick Beryllium target was placed. The beam underwent induced fission in the target and a large range or neutron-rich isotopes was created.

3.2.2 Selection: BigRIPS and ZeroDegree

Figure 3.3 shows a schematic view of BigRIPS, which is a large acceptance, two-stages separator. The large angular acceptance is needed because of the broad angular spread of the fission fragments produced in the target, and it is achieved by using high aperture superconducting quadrupoles. The angular acceptances are ±40 mrad and ±50 mrad in the vertical and horizontal directions, respectively, and the momentum acceptance is ±3%. These acceptances allow for up to 50% transmission in the collection of fission fragments (51). The first stage of BigRIPS is a two-bend achromatic spectrometer that goes from the target position to the F2 focus. It is composed of four superconducting quadrupole triplets (STQ1 to STQ4) and two room-temperature dipoles with a bending angle of 30 degrees (D1 and D2). A wedge-shaped degrader was placed at the momentum-dispersive focal plane F1 to provide the isotopic separation. This stage

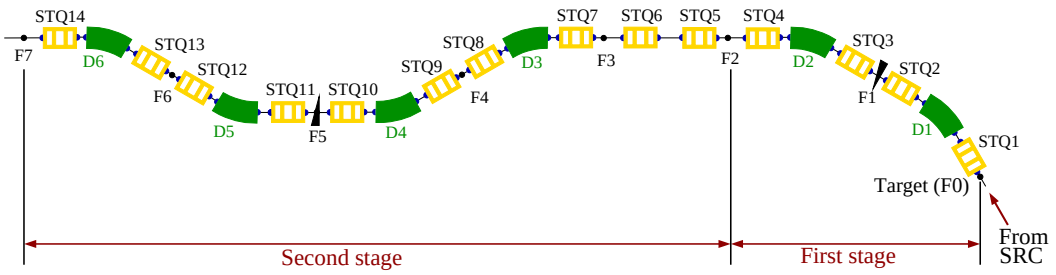

Figure 3.3: Schematics of the BigRIPS separator. The first stage, composed of two dipoles and four STQs, goes from the target position to F2. The second stage, from F3 to F7, is composed of four dipoles and eight STQs. In order to increase the separation, a degrader was placed at the F1 focal plane and a second degrader can be placed at F5.

has a maximum $B\rho$ of 9.5 Tm and it is used to produce and separate RI beams. The second stage, from F3 to the F7 focal plane, is a four-bend achromatic spectrometer consisting of eight STQs (STQ7 to STQ14) and four room-temperature dipoles with a bending angle of 30 degrees (D3 to D6). The intermediate focal planes F4, F5, and F6 are momentum-dispersive, while the final focus F7 is doubly achromatic. A second degrader can be placed at the F5 focal plane in order to improve the separation of the beam (79). This stage has a maximum $B\rho$ of 8.8 Tm. Table 3.1 shows a summary of the characteristics of the BigRIPS separator.

BigRIPS characteristics	
Horizontal acceptance	$\pm$40 mrad
Vertical acceptance	$\pm$50 mrad
Momentum acceptance	$\pm$3%
Momentum resolution	1260/3420
Maximum magnetic rigidity	9.5 Tm/8.8 Tm
Length	78.2 m

Table 3.1: Basic parameters of the BigRIPS separator. The momentum resolution corresponds to the first-order resolution of the first and second stages, respectively, when a beam spot of 1 mm is assumed. The maximum $B\rho$ values given correspond to the first and second stage, respectively.

After being separated and identified, the isotopes of interest were focused in the liquid hydrogen target of MINOS to perform inelastic proton scattering. The target was surrounded by the DALI2 array. Once the reaction takes place, outgoing fragments need to be identified. In the SEASTAR setup, this was achieved by using the ZeroDegree spectrometer. This is a two-bends achromatic spectrometer consisting of two room-temperature dipoles and six STQs. Each STQ has one sextupole to allow for second-order optical aberration corrections. Figure 3.4 shows a schematic view of ZeroDegree. It is to note that STQ15 and STQ16, not shown in the figure, are placed between the F7 focal plane of BigRIPS and the F8 focal plane of ZeroDegree. These two STQs form a telescopic system used to perform the matching between the ion optics of BigRIPS and ZeroDegree.

The first focal point of ZeroDegree is located at F8, where the secondary target was placed. The focal planes at F9 and F10 are momentum dispersive, while the final

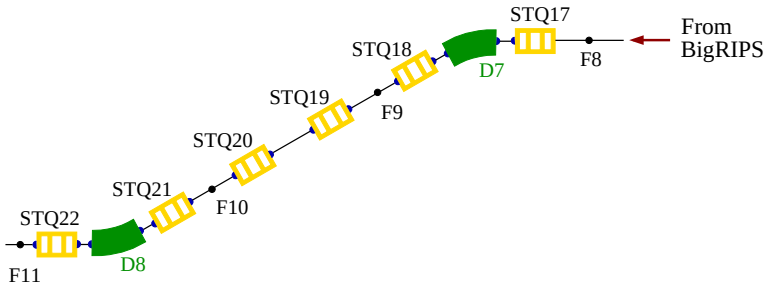

Figure 3.4: Schematics of the ZeroDegree spectrometer. It is composed of two room-temperature dipoles and six STQs.

focus at F11 is fully achromatic. Depending on the experimental needs, the ZeroDegree separator can be tuned to different optical modes, including the possibility to make F11 a dispersive plane. For the first SEASTAR campaign the standard setting, called Large Acceptance Achromatic mode, was used. Table 3.2 summarizes the parameters of the ZeroDegree spectrometer for that setting.

ZeroDegree characteristics	
Horizontal acceptance	±45 mrad
Vertical acceptance	±30 mrad
Momentum acceptance	±3%
Momentum resolution	1240
Maximum magnetic rigidity	8.1 Tm
Length	36.5 m

Table 3.2: Basic parameters of the ZeroDegree separator. The momentum resolution corresponds to the first-order resolution when a beam spot of 1 mm resolution is assumed.

During the first SEASTAR campaign, a passive stopper was placed at F11 surrounded by the EURICA Germanium array (80) in order to perform isomer spectroscopy of the outgoing fragments. EURICA was not used for the inelastic scattering of Ni and Zn isotopes and will not be further described in this thesis. In order to identify the particles passing through BigRIPS and ZeroDegree, different detectors were placed along the beam line.

3.2.3 Identification

3.2.3.1 Atomic number measurement

The determination of the atomic number of the particles was performed using a Tilted Electrode Gas Ionization Chamber (TEGIC) (81). It consisted of twelve anode plates and thirteen cathode planes placed alternatively in 20 mm steps to form a 48 cm long chamber. A reduction in the probability of electron-hole recombination was achieved by tilting the electrode plates by 30°. Figure 3.5 shows a schematic view of the TEGIC. The inner diameter of the electrodes was 116 mm. The full setup was enclosed in an aluminum chamber with 50 μm thick Kapton windows. A gas mixture of Ar-CH_4 (90%, 10%) with a purity above 99.99% was used as the filling gas. Pairs of anode electrodes were electrically connected together inside the chamber, thus only six outputs were read-out. All the cathode planes were connected together and grounded. The electrical connections just described can also be seen in Figure 3.5. The anode voltage was set to 500 V and the outputs were processed using shaping amplifiers and digitized with a charge-to-digital converter (QDC).

Two TEGIC were used in the setup: One placed at the F7 focal plane to determine the atomic number of the incoming particle and one at F11 to measure the atomic num-

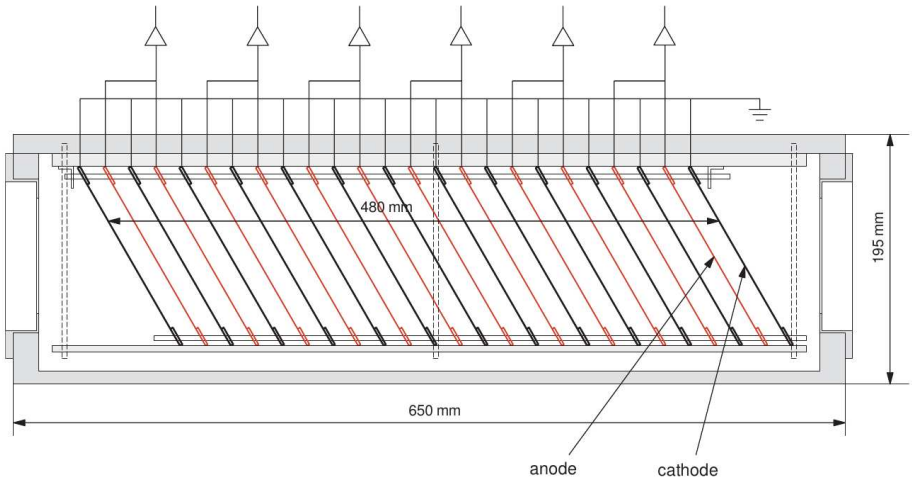

Figure 3.5: Cross-sectional view of the Tilted Electrode Gas Ionization Chamber (TEGIC). The electrode plates are tilted 30° to reduce the probability of electron-hole recombination. The figure was taken from Reference (81).

ber of the outgoing particle after the reaction. In each case, the geometrical average of the six anode signals was taken as a measurement of the energy loss. From that measurement, Z was calculated based on Equation 3.3 as

$$Z = K_1 \beta \sqrt{\frac{\Delta E}{\ln\left(2m_e c^2 \beta^2 / I\right) - \ln(1-\beta^2) - \beta^2}} + K_2, \tag{3.11}$$

where K_1 and K_2 were calibration parameters to be determined experimentally.

3.2.3.2 Time-of-Flight measurement

The ToF measurements were performed by placing thin plastic scintillators at F3 and F7 for BigRIPS and at F8 and F11 for ZeroDegree. Each scintillator was 200 μm thick and was read-out by two PMTs attached to the left and right edges. The electrical pulse from each PMT was split in two. The first signal was read-out by a QDC to obtain the energy loss measurement. The second signal was processed by a leading-edge-discriminator (LED) and a Multi-hit-Time-to-Digital converter (MhTDC) to obtain the timing information of the pulse. The total charge collected by the PMTs is related to the position of interaction of the incoming particle by

$$q_1 = q_0 \exp\left(-\frac{L-x}{\lambda}\right) \qquad q_2 = q_0 \exp\left(-\frac{L+x}{\lambda}\right), \tag{3.12}$$

where q_1 and q_2 represent the charges measured in the left and right PMTs respectively, λ denotes the attenuation length of light in the scintillation material, $2L$ and x represent the length of the scintillation counter and the horizontal position of an incident particle respectively, and q_0 represents the total charge created in the scintillation event. From Eq. 3.12, it is possible to obtain the position information as

$$x = \frac{\lambda}{2} \ln\left(\frac{q_1}{q_2}\right). \tag{3.13}$$

The timing signals from the PMTs also contain the position information of an incident particle, which can be expressed by

$$x = \frac{V}{2}\left(t_2 - t_1\right), \tag{3.14}$$

where t_1 and t_2 represent the timing information from the left and right PMTs, respectively, while V is the speed of light in the scintillator. As the position of an incident

particle is unique, every event should fulfill the condition

$$\frac{\lambda}{2}\ln\left(\frac{q_1}{q_2}\right) = \frac{V}{2}\left(t_2 - t_1\right). \tag{3.15}$$

A first check of the behavior of the detector can be then performed by observing that Eq. 3.15 holds.

In order to remove position dependencies, the timing of a fragment passing through a plastic was determined as the average of the left and right time measurements as

$$\text{Time(Fx)} = \frac{1}{2}\left(t_1(\text{Fx}) + t_2(\text{Fx})\right), \tag{3.16}$$

where the notation "Fx" refers to the x focal plane where the plastic is located. The ToF along BigRIPS (ToF_{37}) and ZeroDegree (ToF_{811}) are then calculated as

$$\begin{aligned} \text{ToF}_{37} &= \text{Time(F7)} - \text{Time(F3)} + \text{TimeOffset(37)} \\ \text{ToF}_{811} &= \text{Time(F11)} - \text{Time(F8)} + \text{TimeOffset(811)}, \end{aligned} \tag{3.17}$$

where TimeOffset(37) and TimeOffset(811) are parameters to adjust experimentally. For the case of ZeroDegree, the velocity of the outgoing particles (β_{811}) can be calculated in a straightforward way by knowing the flight path between F8 and F11 (L_{811}) using the relation

$$\text{ToF}_{811} = \frac{1}{c}\frac{L_{811}}{\beta_{811}}. \tag{3.18}$$

For BigRIPS, it is necessary to take into account that the degrader placed at F5 alters the velocity of the particle. A more accurate description for this separator is

$$\text{ToF}_{37} = \frac{1}{c}\left(\frac{L_{35}}{\beta_{35}} + \frac{L_{57}}{\beta_{57}}\right), \tag{3.19}$$

where L_{35} and L_{57} represent the flight paths between F3-F5 and F5-F7 respectively and β_{35} and β_{35} correspond to the velocity of the particle between the same focal planes.

3.2.3.3 Position measurement

Position measurements were performed using delay-line Parallel Plate Avalanche Counters (PPACs) (82, 83). Figure 3.6 shows an schematic view of a PPAC. It consisted of an anode plate located between two cathodes which were connected to delay-lines. The anode was 2.5 μm thick and each cathode was 4 μm thick. The distance between the electrodes was 4.3 mm. The cathodes were formed by 2.4 mm wide strips

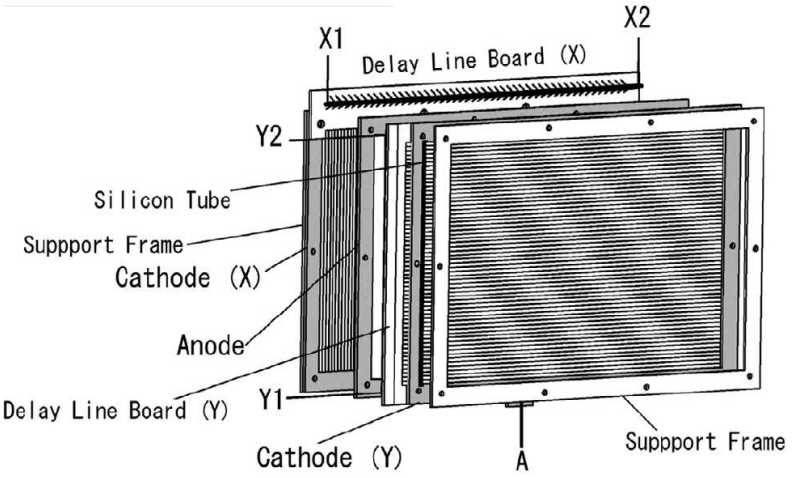

Figure 3.6: Schematic view of a delay-line Parallel Plate Avalanche Counter. The figure is taken from Reference (83).

with 0.15 mm inter-strip distance and the total active area of the detector was 240 $\times$ 150 mm^2. In order to achieve higher detection efficiency and to have a backup measurement, two PPACs were placed in a single chamber made of duralumin to form what is called a double PPAC. The chamber was closed by window plates made of 12μm thick aluminum-deposited polyester. As filling gas, C_3F_8 at a pressure of 10 Torr was used and an anode bias of about 850 V was applied.

As seen from Figure 3.6, five pulses from each PPAC: X1, X2, Y1, Y2, and a signal from the Anode (A) are obtained. These signals were sent to a fast amplification stage and were processed by a discriminator before being send to a TDC to get the timing signals. Denoting the times measured as T_{X1}, T_{X2}, T_{Y1}, T_{Y2}, and T_A, the x and y position of interaction can be obtained by

$$\begin{aligned} x &= k_x \frac{T_{X1} - T_{X2}}{2} + X_{offset} \\ y &= k_y \frac{T_{Y1} - T_{Y2}}{2} + Y_{offset}, \end{aligned} \tag{3.20}$$

where k_x and k_y are the slope factors of the delay line and are typically 1.25 mm/ns and X_{offset} and Y_{offset} are parameters included to take into account the delay line offset and any geometrical misalignment. For an event to be consistent, the sum of the times measured at each side of the cathode with respect to the anode has to be

constant. Thus, the quantities T_{sumX} and T_{sumY}, defined as

$$\begin{aligned} T_{sumX} &= T_{X1} + T_{X2} - 2T_A \\ T_{sumY} &= T_{Y1} + T_{Y2} - 2T_A, \end{aligned} \tag{3.21}$$

can be used to remove the effect of δ rays and multiple hits.

Pairs of double PPACs were placed at the focal planes F3, F5, and F7 for BigRIPS and at F8, F9 and F11 in ZeroDegree. The F8 PPACs were placed before the secondary target. This means that in each one of these focal planes, four measurements of x and four measurements of y were obtained. To determine the position of the particle in a given focal plane, each PPAC with valid T_{sumX} and T_{sumY} was taken into account to perform a linear track reconstruction. With this reconstruction, it was possible to project the position of the particle at the focal plane and also to obtain the angle of its trajectory in the horizontal and vertical directions.

3.2.3.4 A/Q determination

As shown in Equation 3.8, using the horizontal position of the particle measured by the PPACs and the optical parameters of the separator, the magnetic rigidity of each magnetic section can be obtained. The optical parameters were calculated using the COSY INFINITY code (84) and can be found in the Appendix A. To determine A/Q, it is necessary to know the velocity of the particle. As mentioned in Section 3.2.3.2, the presence of the degrader in F5 leads to Equation 3.19. It is possible to avoid the independent measurement of β_{35} and β_{57} by assuming that the only change experienced by the particle when crossing the degrader is a change in velocity. In this case, the A/Q of the particle is constant and, using Equation 3.5

$$\frac{(B\rho)_{35}}{\gamma_{35}\beta_{35}} = \frac{(B\rho)_{57}}{\gamma_{57}\beta_{57}}, \tag{3.22}$$

is obtained. The subscript "35" and "57" refer to values between F3-F5 and F5-F7 respectively. Combining Equation 3.19 and Equation 3.22, it is possible to solve for β_{35} and β_{57} as

$$\beta_{35} = \frac{aL_{35} + c\text{ToF}_{37}L_{57}}{ac\text{ToF}_{37} + L_{35}L_{57}(1-R^2)} \tag{3.23}$$

$$\beta_{57} = \frac{aL_{35} + c\text{ToF}_{37}L_{57}}{c^2\text{ToF}_{37}^2 + L_{35}^2(R^2-1)}, \tag{3.24}$$

where

$$a = \sqrt{c^2 \mathrm{ToF}_{37}^2 R^2 + L_{35}^2 (R^4 - R^2) + L_{57}^2 (1 - R^2)}$$
$$R = (B\rho)_{57}/(B\rho)_{35}. \tag{3.25}$$

A complete deduction of these equations can be found in Appendix B. To obtain the A/Q of the incoming and outgoing particles, it is possible to combine the calculated velocities and magnetic rigidities in different ways and use Equation 3.5. In Section 4.2, a discussion of the different ways to obtain A/Q is presented.

3.2.4 Secondary target: MINOS

MINOS (MagIc Numbers Off-Stability) is a device developed to perform different proton-induced reactions on very exotic neutron-rich nuclei. It consists of a thick liquid hydrogen target surrounded by a vertex tracker, which allows to reconstruct the reaction vertex position inside the target. Thanks to this reconstruction, it is possible to have a target length up to 150 mm and obtain a Doppler correction better than the one for a passive target (85). In the following sections, the liquid hydrogen target, the vertex tracker and the vertex reconstruction of MINOS are briefly discussed. A more complete description of the design, construction and commissioning of MINOS can be found in References (11) and (86).

3.2.4.1 Liquid hydrogen target

The target cell containing the liquid hydrogen had a cylindrical shape with curved caps. It was made of Mylar foils glued to a stainless steel target holder structure. The glue was chosen to stand low temperatures. The Mylar foil forming the entrance window had an effective diameter of 38 mm and was 110 μm thick. The foil corresponding to the exit window had a 52 mm diameter and was 150 μm thick. The total length of the cell could be varied between 100 mm and 150 mm. For the case of the first SEASTAR campaign, the length used was 100 mm. The caps were thermoformed at 160°C using a stamping press. An additional deflection of the entrance window of between 1.35 mm and 2.70 mm due to the pressure difference when the target was filled has been reported (86). The variation in target thickness created because of this is small compared to the position resolution. The exit window was rigid. Two pipes

passing through the target holder took care of the liquid hydrogen supply and the gas exhaust. The hydrogen was liquefied in a cryostat equipped with a Cryo-cooler, which was placed above the target. After being liquefied, the hydrogen fell by gravity into the target cell. The target cell was placed inside an 800 mm long aluminum beam pipe of 72 mm inner diameter and 2 mm thickness (86). Mylar windows of 150 μm thickness were placed at each end of the pipe and the chamber was pumped to a vacuum of $\approx 10^{-6}$ mbar.

3.2.4.2 Vertex tracker

The MINOS vertex tracker was used to make a 3D reconstruction of the tracks of the scattered protons and to determine their point of origin inside the liquid hydrogen target. It was formed by an annular Time Projection Chamber (TPC) read-out in one side by a Micro-Mesh Gaseous Structure detector (MicroMegas) (87). A Double Sided Silicon Strip Detector (DSSSD) was placed in front of the TPC to be used as a beam tracker. It is possible to add a second DSSSD in the other end of the TPC as well as an external MicroMegas cylindrical tracker. As those components were not used for the SEASTAR campaign, they will not be discussed.

The TPC was formed by two concentric cylinders made of 2 mm thick polymethacrylimide structural foam (Rohacell). The internal diameters of the cylinders were 80 mm and 178.8 mm and the length of the vessel was 300 mm. The internal surfaces of the cylinders were covered with a gas tight copper-stripped Kapton foil to form the field cage. The TPC volume was filled with a gas mixture of Argon (82%), CF_4 (15%) and isobutane (3%) and a voltage of 6 kV was applied between the electrodes. The composition used in the gas admixture was defined using the gas simulation program Magboltz (88). One of the end caps of the cylinder was used as the cathode. This side also held the high-voltage connections and the gas outlets. The other end cap held the gas inlets as well as the MicroMegas detector.

In the MicroMegas detector, a metallic micro-mesh under high-voltage was placed in the gas volume, very close to the anode, to create an amplification region. This detector was chosen as a read-out as it provides high gain together with a fast output signal. A bulk-MicroMegas detector (89) was used, with a space between the mesh and the anodes of 128 μm. A voltage between 450 V and 470 V was applied to the mesh

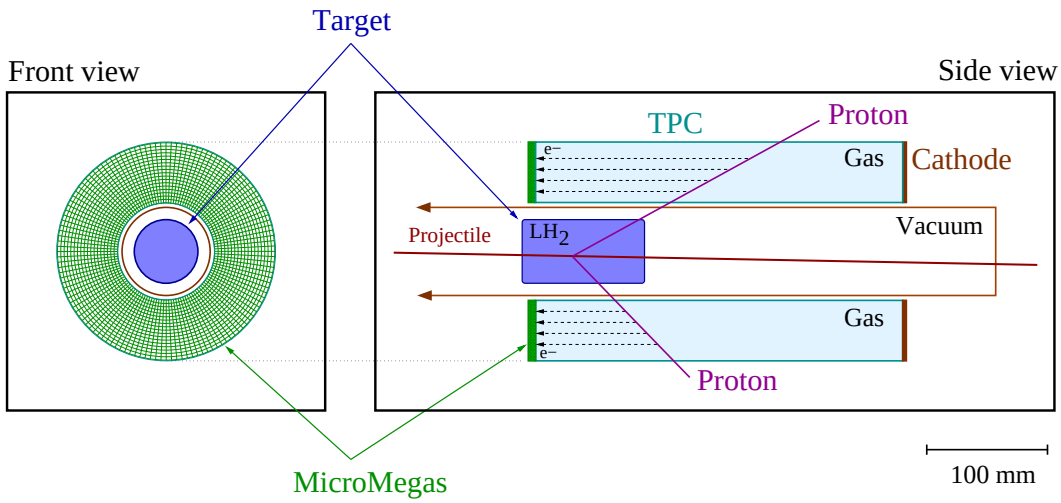

Figure 3.7: Schematics of the MINOS setup. When an incoming projectile undergoes a proton-induced reaction in the liquid hydrogen target, protons are scattered and cross the TPC volume. The ionization electrons produced inside the gas volume drift towards the MicroMegas detector. A DSSSD, not shown in the plot, was placed in front of the target to monitor the beam. All distances are to scale.

for a resulting gain between 6000 and 13000. The anode was segmented in pads of different area, arranged in a matrix of 18 rings with 256 pads each, leading to 4608 electronics channels.

For the SEASTAR campaign, a DSSSD was placed 458 mm in front of the center of the target. It was a 100×100 mm^2 detector from Micron, composed of 128 strips with 560 μm pitch in each side. This detector could be used to monitor the beam and have a more precise determination of the beam trajectory and the interaction vertex. Figure 3.7 shows an schematic view of MINOS in the configuration used for the SEASTAR campaign. In the front view, the pattern formed by the pads of the MicroMegas detector can be seen. The liquid hydrogen target as well as the TPC and the vacuum pipe are depicted. The DSSSD is not shown in the plot.

The signals from the TPC and the DSSSD were read-out using the front-end-cards (FEC) developed for the T2K experiment (90), each one equipped with four AGET chips (91). Each chip was composed of 64 channels, each channel formed by a charge sensitive pre-amplifier, a shaper and a discriminator. Thanks to the use of the discriminator, only the channels that fired were processed by the subsequent electronics in

order to save resources. The output signal of the shaper was digitized in 512 samples using the Feminos card (92), developed particularly for the MINOS setup. The trigger for the digitization was given by the external experimental trigger, which will be discussed in Section 3.2.6. The full signal shape was sent to the data acquisition system and further analysis was performed via software.

3.2.4.3 Vertex reconstruction

The digitized pulse shape, corresponding to the charge collected in each fired pad as a function of time, was fitted using the formula

$$q(t) = q_0 \exp\left\{-3\left(\frac{t - t_{pad}}{\tau}\right)\right\} \sin\left(\frac{t - t_{pad}}{\tau}\right)\left(\frac{t - t_{pad}}{\tau}\right)^3 + q_b, \tag{3.26}$$

where q_0 and q_b represent the amplitude of the signal and its base line respectively, τ is the shaping time used by the electronics and t_{pad} is the time at which the pad was fired. The constant q_b depends on the electronics and can be set to a fixed value using an initial empty target measurement. The value chosen for this pedestal was 250. At the beginning of each run the pedestal value of each channel was checked. The shaping time was also an electronics constant and it was chosen as 333 ns. Thus, the fit yields the amplitude of the measured charge pulse and the time when the pad was fired. Panel a) of Figure 3.8 shows a typical pulse shape recorded as well as the fit performed to obtain q_{pad} and t_{pad}. These data correspond to a cosmic-rays test reported in Reference (86). In addition, the known position of the pads that fired, (x_{pad}, y_{pad}), gives a 2D image of the event, as shown in panel b) of Figure 3.8.

Taking into account that the electrons inside the TPC drift following straight lines, it is possible to extract the position along the TPC where the charge was created, z_{pad}, by using t_{pas} as

$$z_{pad} = (t_{pad} - t_0)\, v_{drift}. \tag{3.27}$$

Here, v_{drift} represents the drift velocity of the electrons in the gas of the TPC and t_0 is an offset included to take into account the acquisition trigger time. This equation represents the MINOS calibration, where t_0 and v_{drift} are parameters to find experimentally. While t_0 is a constant over the entire experiment, the drift velocity is affected by water impurities in the gas, thus a calibration of this value has to be performed run by run. By using the z_{pad} information, it is possible to generate a 3D reconstruction of

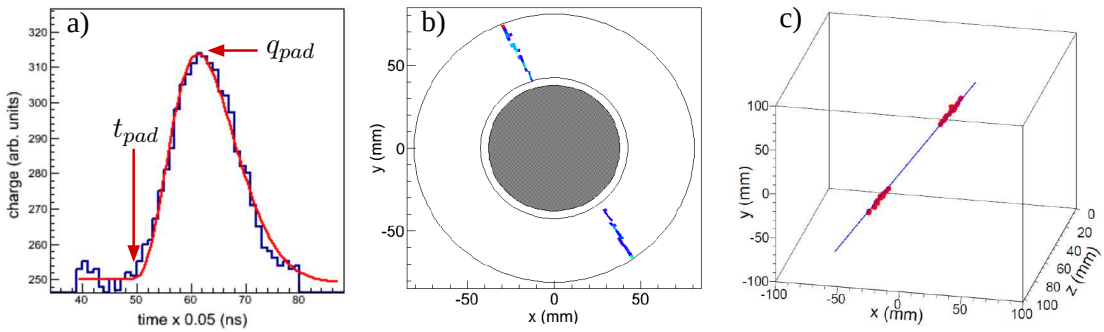

Figure 3.8: Example of MINOS signals analysis. Panel a) shows a typical signal recorded in a single pad as well as the fit performed in order to obtain q_{pad} and t_{pad}. Panel b) shows the 2D image obtained by plotting the (x_{pad}, y_{pad}) positions of the pads fired. Panel c) shows the 3D reconstruction of the tracks obtained by combining the 2D image with the z_{pad} information. The data correspond to a cosmic-rays test. Figure is taken from Reference (86) and modified.

the track, as shown in panel c) of Figure 3.8. Using the reconstructed tracks, it is possible to extract the vertex position inside the target for each event. This reconstruction was performed in three main steps.

In the first step, the 2D image created by the position of the fired pads was analyzed by a modified 2D Hough-transformation (86, 93). This procedure allowed the identification of straight lines inside the image and was applied iteratively over all the pads in order to find the most likely combination of tracks. Each identified track had to be formed by 10 or more fired pads, that the minimum amount of charge collected in each pad was 9000 electrons and at least three pads were hit in the four most inner rings of the MicroMegas detector. These conditions guaranteed that background events and sparks in the MicroMegas detector were not further processed. In the second step, the 3D image of the tracks was analyzed. A standard Hough-transformation was applied in the (x, y), (x, z) and (y, z) planes, once for each identified track. The events were further processed only if at least 15 rings of the MicroMegas detector were hit. An exception to this condition was applied for tracks with low angle, corresponding to protons with low scattering angle which crossed the cathode. This step allowed to discard events coming from δ-electrons created along the path. The last step consisted of finding the vertex position inside the target and has been implemented only for one and two final tracks so far. For the case of a single track, the intersection between

the horizontal plane and the track was found and reported as the vertex. When two tracks were reconstructed, each one of them was projected to the target volume. If they crossed, the vertex point was given by the crossing point. If they did not cross, the path that produced the minimum distance between the lines was calculated. The vertex point was then given as the mid-point of this line. The final position resolution achieved using MINOS was 5 mm in FWHM. Additional information for the vertex reconstruction can be obtained by tracking the incoming beam using the PPACs placed at the F8 focal plane or the DSSSD, in case only one proton was detected with the TPC.

3.2.5 γ-ray detection with the DALI2 array

3.2.5.1 The DALI2 array and the MINOS-DALI2 setup

DALI2 (Detector Array for Low Intensity radiation 2) is an array of 186 NaI(Tl) detectors, which is the successor of the original DALI array used at the old facility of RIKEN (94). It was designed to fulfill the needs of γ-ray spectroscopy measurements using the fast radioactive beams of the RIBF.

The full array is composed of three different types of crystals, each type with different size. The first type, manufactured by Saint-Gobain, has a volume of $45 \times 80 \times 160$ mm^3. The second type, manufactured by Scionix, has a volume of $40 \times 80 \times 160$ mm^3 and the third type, originally fabricated for DALI by Bicron, has a volume of $60 \times 60 \times 120$ mm^3. Each crystal has a thin MgO coating, a 1 mm thick aluminum housing and is read-out using a Hamamatsu PMT. The typical energy resolution achieved was about 8% (FWHM) for 662 keV (71). Table 3.3 summarizes the properties of the different types of crystals used in DALI2.

Manufacturer	Crystals	Size (mm^3)	PMT model	PMT diameter (mm)
Saint-Gobain	88	$45 \times 80 \times 160$	R580	38
Scionix	66	$40 \times 80 \times 160$	R580	38
Bicron	32	$60 \times 60 \times 120$	R1306	50

Table 3.3: Properties of the DALI2 crystals. DALI2 is formed by three different types of crystals, each with a different size. The PMTs used in all the cases are from Hamamatsu.

Due to the Lorentz boost, it is particularly important to have a good detection coverage at forward angles. In DALI2, this requirement was fulfilled by placing an array

of sixty four crystals in forward directions (32 Bicron crystals and 32 Scionix crystals). In the DALI2 standard configuration, the rest of the crystals are arranged in eleven layers perpendicular to the beam axis. In order to have enough space for MINOS and its related electronics, for the SEASTAR campaign the crystals were arranged in only ten layers, each consisting of between ten and fourteen crystals. Figure 3.9 shows a schematic view of the DALI2 array as mounted for the SEASTAR campaign, where some detectors have been removed to visualize the forward angles matrix.

The PMTs of the Saint-Gobain and the Bicron crystals were powered to a voltage between -1000 V and -1600 V, while the PMTs of the Scionix crystals were powered to about +1000 V, taking care that they all showed a similar gain. The output signal from each PMT was fed into a shaping amplifier and split in two to get both time and energy measurements. For the energy branch, the signal was processed by a peak-sensing ADC. The timing branch, which corresponded to the fast output of the shaping amplifier, was

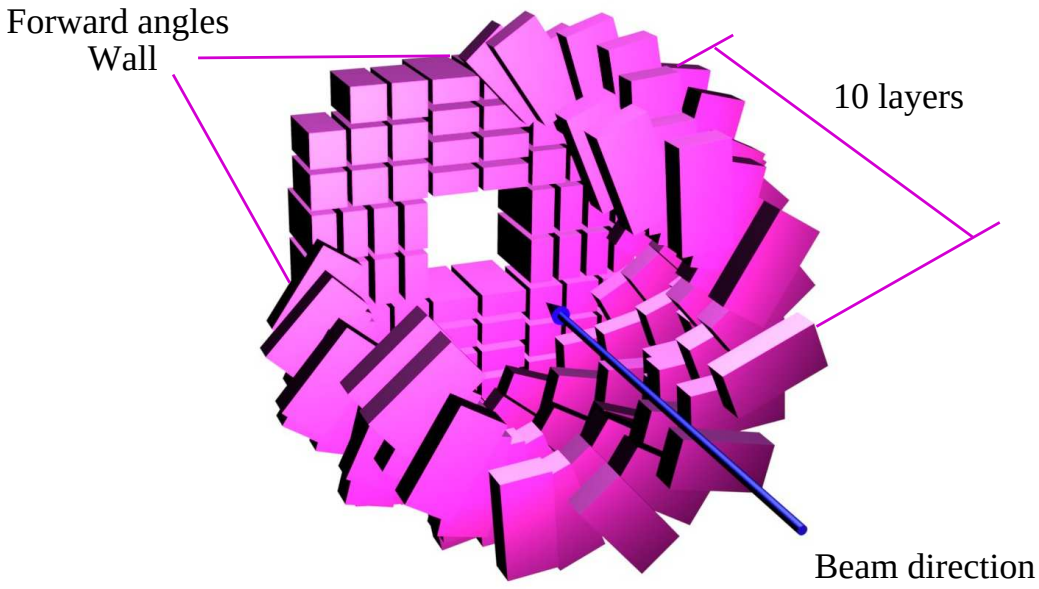

Figure 3.9: Schematic view of the DALI2 array. The ten layers perpendicular to the beam direction are shown, as well as the detector array placed in forward direction. Some detectors have been removed from the plot to allow for a better visualization.

processed by a constant-fraction-discriminator (CFD) and sent to a MhTDC. A threshold of about 200 keV was set in the CFD to discard low-energy background events. An OR signal of all the CFD outputs was used to create a γ-trigger condition.

To perform proton-induced reactions, the MINOS setup was placed inside the DALI2 array at the F8 focal plane of BigRIPS. Due to the large size of MINOS, the liquid hydrogen target was not placed in the nominal target position, but 18.35 cm upstream. Figure 3.10 shows the geometrical arrangement of the MINOS-DALI2 setup used in the first SEASTAR campaign, and the distances (in cm) between the different parts of the setup. It is noted that the TPC edge was 1.3 cm shifted with respect to the edge of the liquid hydrogen target. In this configuration, DALI2 had an angular coverage between approximately 10° and 117°.

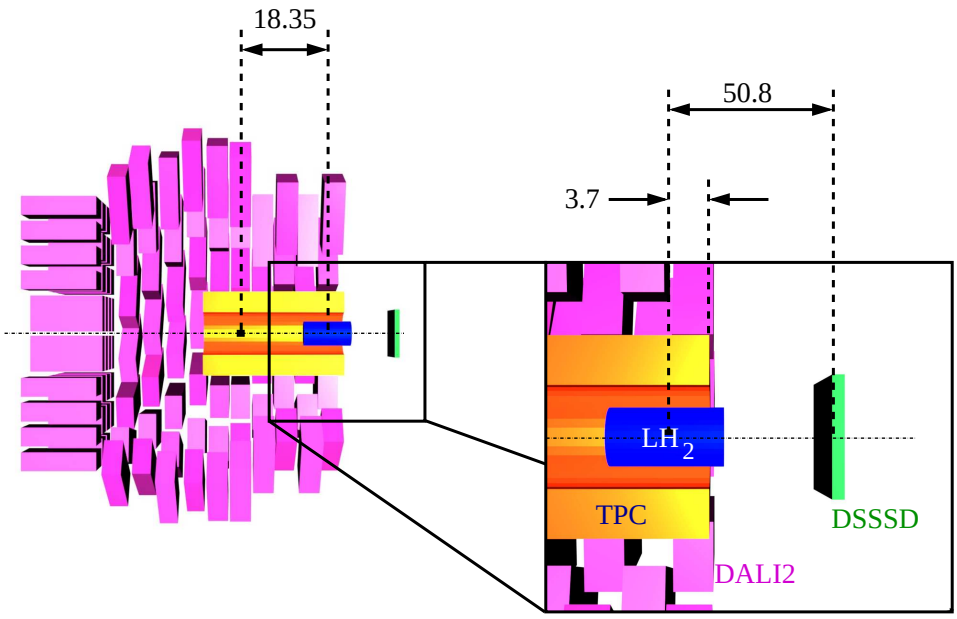

Figure 3.10: Schematic view of the MINOS-DALI2 setup placed at the F8 focal plane of BigRIPS. The liquid hydrogen target was not placed in the nominal target position, but 18.35 cm upstream. The distances between different parts of the setup are shown. The position of the DSSSD is not to scale. All distances are in cm.

3.2.5.2 Simulation of the response of DALI2

In order to fully characterize the response of DALI2, a complete `Geant4` (95) simulation is available. It allows to obtain reliable values for the γ-ray detection efficiency and energy resolution of a chosen detector geometry under realistic experimental conditions. It also takes into account effects on the γ-ray line-shape due to the target thickness and lifetimes of the excited states. More information on the simulation can be found on-line (96). As the SEASTAR setup uses an extended target, the use of the simulation to obtain efficiency values is fundamental. The simulation is divided in three steps, independent of each other.

In the first step, called the `EventGenerator`, the interaction of the projectile and the target is simulated. It takes into account the energy loss of the incoming and outgoing particles in the target and the emission of de-excitation γ-rays from the particles. Parameters such as the incoming and outgoing fragments of interest, the initial beam energy, the material and dimensions of the target and the level scheme of the excited states, can be defined using a parameter input file. This step also allows the inclusion of atomic background into the simulation. In addition, it is possible to simulate stationary sources in order to characterize the array.

The second step is called `EventBuilder`. This step simulates the detection of the γ-rays emitted by the particles. The DALI2 geometry is included in this step to get a realistic response of the array. The resolution of each crystal, experimentally obtained from stationary sources, can be used as an input of this step to get more realistic results. A beam pipe surrounding the target can also be included and a finite resolution in the determination of β can be taken into account. Additionally, Pb or Sn absorbers can be used in the simulation.

The third and final step is called `Reconstructor`. It is in charge of performing the data analysis on the simulated results. In addition to the Doppler correction, this step also performs the add-back procedure, which aims to recover the full energy peak for events where the photon performs a Compton scattering in one detector and is finally absorbed in a neighboring crystal. It is performed by selecting the crystal where the most energetic γ-ray is detected and adding to this energy the energies of the γ-rays detected in the crystals surrounding it within a given distance. The output of this step is stored in a `root` tree and can be compared to the experimentally obtained spectra in

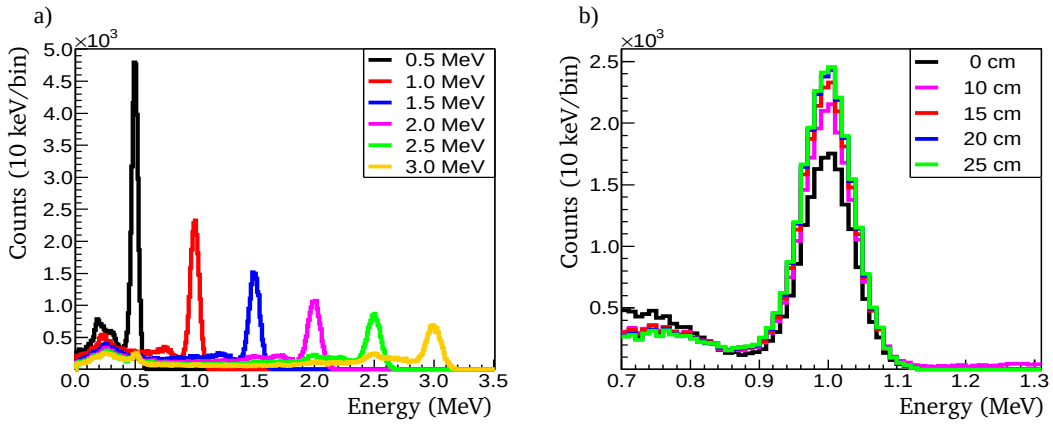

Figure 3.11: Simulation of stationary sources placed inside DALI2. Panel a) shows the response of DALI2 for different energies. The decrease in absolute efficiency and resolution can be observed. Panel b) shows the effect of the add-back procedure for different maximum distances. Improvements can be seen for 1 MeV γ-rays up to 15 cm.

order to determine the efficiency of the array and the number of de-excitation γ-rays that occurred.

Figure 3.11 shows results of simulations performed for stationary sources. Panel a) shows the response of the array to γ-rays of different energy. In all the cases the add-back procedure was applied up to a distance of 15 cm. The decrease in absolute resolution and efficiency as the energy increases can be seen. Panel b) shows the effect of using different add-back distances. The photopeak efficiency increases significantly when using add-back up to 15 cm. For larger distances, the improvements are not significant. It has been reported that the simulated efficiency of the array agrees within 6% with the experimental efficiency (97). The simulated absolute efficiency of the array for 661 keV γ-rays, without add-back, has been calculated to be 25% for the SEASTAR campaign (86).

The expected resolution and efficiency of the array for γ-rays emitted in-beam was also estimated using the `Geant4` simulation. To take into account the conditions of the SEASTAR campaign, excited states of the Ni isotopes with $\beta \approx 0.6$ decaying after interacting with a 10 cm liquid hydrogen target were simulated. In all the cases, a negligible life time of the states and a relative error in β of 10% were assumed. Panel a) of Figure 3.12 shows the estimated resolution of the peaks after performing Doppler correction for different transition energies. To show the effect of the vertex information

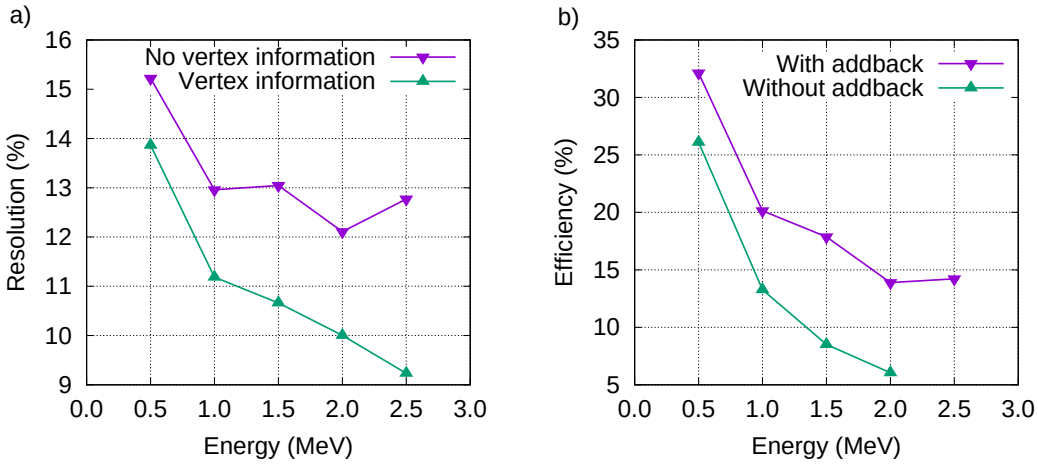

Figure 3.12: Simulation of γ-rays emitted in-beam. Panel a) shows the resolution obtained after Doppler correction as a function of the decay energy. The effect of using the vertex information from MINOS can be clearly seen. Panel b) shows the absolute photopeak efficiency after Doppler correction. In this case, the effect of using add-back up to 15 cm can be seen.

given by MINOS, two cases were simulated: In the first case, the particle was assumed to decay in the center of the target, while in the second case, the information of the position of interaction was taken into account with an uncertainty of 5 mm. The improvement on the resolution obtained by having the vertex information from MINOS can clearly be seen. Nevertheless, this improvement in resolution comes with a reduction on the photopeak efficiency due to the requirement of detecting a proton in the MINOS TPC. Panel b) of Figure 3.12 shows the simulated absolute photopeak efficiency after performing Doppler correction for different decay energies. The effect of applying add-back up to 15 cm is also shown. A clear improvement can be seen when applying the add-back procedure, specially at higher energies. For a decay of 2.5 MeV, it is not possible anymore to see a photopeak without applying add-back. In this calculation, the efficiency of the MINOS TPC was not taken into account. A use of the simulation to estimate this efficiency is discussed in Chapter 4.

3.2.6 Electronics and trigger configuration

The electronics used to read-out each of the detectors surrounding the beam line and the SEASTAR setup at F8 were briefly described in the corresponding section, and here

a more comprehensive review of these connections as well as the trigger configuration is presented. Figure 3.13 shows a schematic view of the electronics used in the setup. It can be categorized in five subsystems, corresponding to five different detectors: TEGICs, PPACs, Plastics, DALI2 and MINOS.

There were two TEGICs in the setup, one placed at F7 and one placed at F11. Each one of them provided the signals of six anodes. These signals were processed by shaping amplifiers. For the case of the TEGIC at F7 an Ortec 572 Spectroscopic Amplifier with 3 μs shaping time was used, and for the TEGIC at F11 a Canberra 2014 Fast Spectroscopic Amplifier with 2 μs shaping time was employed. In both cases, the

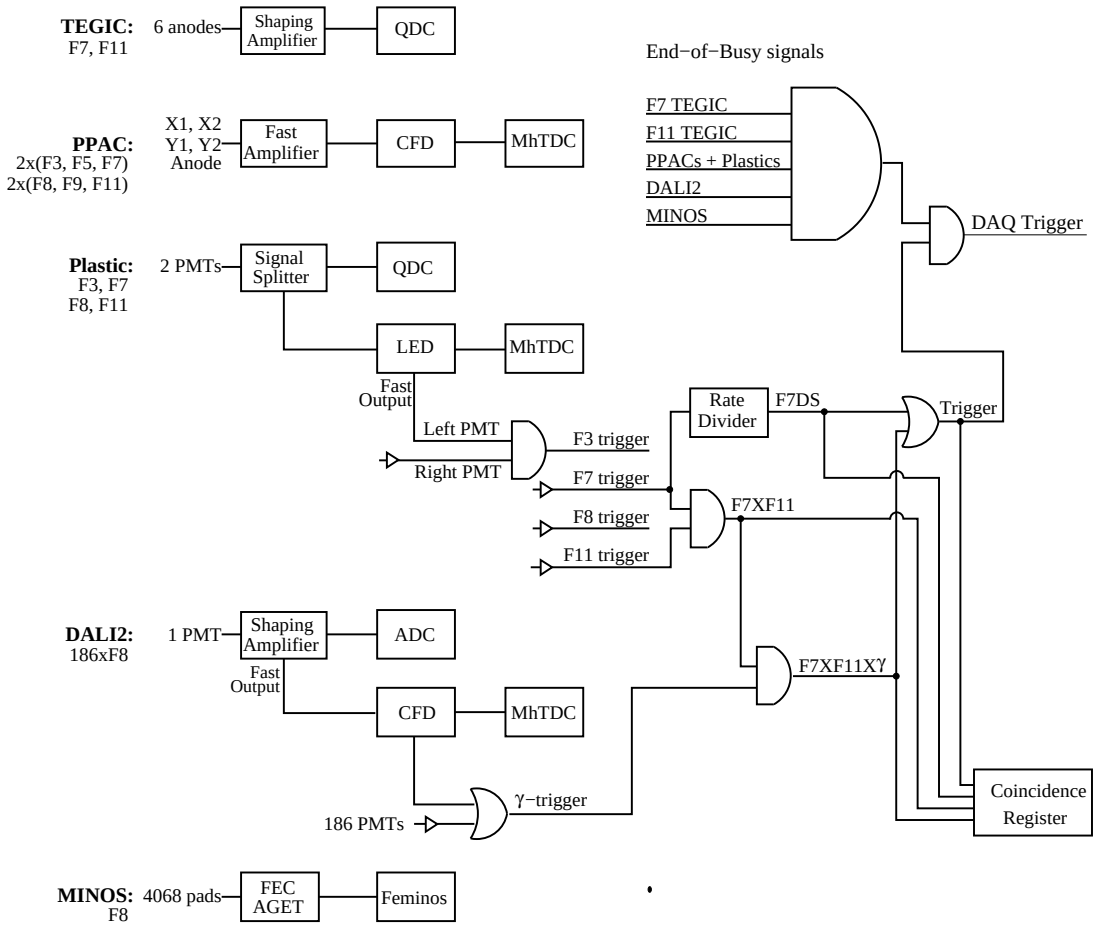

Figure 3.13: Schematic view of the electronics setup. It is divided in five subsystems, corresponding to different detectors. The location of each detector is shown along with the modules used to process each signal. The trigger configuration is also shown.

output of the amplifiers was sent to CAMAC-standard Philips 7166 QDCs. Each TEGIC was processed in a different CAMAC crate placed at the experimental hall next to the setup.

To measure the beam position, pairs of double PPACs were placed at the focal planes F3, F5, F7, F8, F9 and F11. This made in total 24 single PPACs placed along the beam line. Each PPAC gave five signals: Two for the x-position, two for the y-position and one anode signal. Each signal was amplified using an custom-made Octal Amplifier placed next to the corresponding PPAC. The amplified signal was forwarded to the Control Room (B3F) using optical cable transmitters that keep the pulse shape (83). The timing of the signals was obtained using a Quad-CFD and digitized with a CAEN V1190 MhTDC.

Plastic scintillators were placed along the beam line at F3, F7, F8 and F11 focal planes. Each one was read-out by two PMTs attached to the left and right edges of the plastic. The fast signal of each PMT was transmitted to B3F using optical cable transmitters and divided using an Octal Signal Divider. One of the signals went to a CAEN V792 QDC to get the energy information. The integration gate used for this module was about 500 ns. The second signal went to a LED, where a threshold of about 10 mV was applied. The standard output of the LED went to a CAEN V1290A MhTDC to be digitized. The fast output from the LED was combined with the timing information from the PMT placed in the opposite edge of the same detector to create a trigger for each plastic. The F3 trigger and the F8 trigger were not in use for the trigger in the SEASTAR setup. The processing of F7 trigger and F11 trigger will be discussed below. The read-out of the PPACs and the plastic was performed with a shared VME-standard acquisition.

The 186 crystals of DALI2, placed at F8, were read-out with CAEN N568B spectroscopy amplifiers. The normal output of the amplifier was digitized using a CAEN V785 peak-sensing ADC. The fast output was sent to a CAEN V812 CFD, where a threshold of about 70 mV, corresponding to 200 keV, was applied. This timing information was digitized with a CAEN V1190A MhTDC. In order to create a γ-trigger, an OR signal of all the crystals was generated. All the DALI2 electronics were read-out by a VME crate placed in the experimental hall next to the DALI2 array. The γ-trigger was sent to B3F via optical transmitters.

The MINOS setup was placed inside the DALI2 array. The 4068 pads of the MicroMegas detector as well as the 128×128 strips of the DSSSD were read-out using the AGET chips mounted on the T2K FEC.

The processing of the trigger was all done at B3F and started by splitting the F7 trigger signal. One of the branches went to a rate divider to form what is called the F7DS signal (F7 Down-Scaled). The scaling factor could be selected in the front panel of the module. During most of the experiment, it was selected as 1/20. This signal was the first hardware trigger used in the experiment. It can be used to determine the total number of particles reaching the target. The second signal was combined with the F11 trigger in a coincidence module. This created the F7XF11 signal. The F7XF11 signal was further combined in a coincidences unit with the γ-trigger created by DALI2. This resulted in the F7XF11Xγ signal, which was the physics trigger to be used in the experiment. The final trigger of the system was created by an OR gate of the F7DS and the F7XF11Xγ signals.

Nevertheless, it was still necessary to take into account the dead time of the system. The SEASTAR setup was configured as a common-dead-time system, which means that End-of-Busy signals were generated in each electronics crate and combined with an AND gate to know that the full system was ready to process the next event. The five crates producing these signals were the CAMAC crate of each TEGIC, the VME crate processing the PPACs and the plastics, the DALI2 VME crate and the MINOS crate. The resulting End-of-Busy signal was finally combined with the trigger output to produce the final DAQ trigger. This trigger was used to start the acquisition in each module of the setup as well as to produce the different gates required. In addition, a coincidence register was used to keep record of the different types of coincidences measured with the two hardware triggers. The F7DS, F7XF11 and the F7XF11Xγ signals were used as inputs of this module. The coincidence information measured by this module was stored on disk along with the event.

3.3 Description of the experiment

During the first SEASTAR campaign, three different settings of the BigRIPS separators were used. In all of them, secondary beams of interest were produced using a ^{238}U primary beam at 345 MeV/u impinging on a ^{9}Be target at the entrance of the BigRIPS

separator. The calculation of the values of the magnetic fields, target thickness, F1 and F5 degraders and slits was performed using LISE++ simulations (98) and optimized in-beam. In the first setting, ^{67}Mn was centered in BigRIPS and, in order to select mainly $(p, 2p)$ reactions in MINOS, the ZeroDegree spectrometer was set to allow isotopes around ^{66}Cr. In the second setting, ^{73}Co was selected in BigRIPS and ^{72}Fe was centered in Zero Degree, and in the last setting, ^{79}Cu was selected in BigRIPS and ^{78}Ni was centered in ZeroDegree. It is to note that for the first dipole of BigRIPS, the selection of the magnetic rigidity was not centered on the momentum of the isotope of interest, but several percentage higher due to the rate limitations of MINOS and BigRIPS. In all the cases, the ^{238}U beam had an intensity of 12-15 pnA and the primary ^{9}Be target was 3 mm thick. In the three settings, an 8 mm thick aluminum wedge degrader was used at F1 and a 2 mm thick aluminum wedge degrader was used at F5. The slits placed along the ZeroDegree spectrometer were completely open for all the settings. Table 3.4 shows a summary of the parameters used for each setting. The average energy of the beam in front of the target was calculated using LISE++ to be around 250 MeV/u

Parameter	Setting 1	Setting 2	Setting 3
Beam centered at BigRIPS	**^{67}Mn**	**^{73}Co**	**^{79}Cu**
$B\rho_{01}$ (D1) [Tm]	7.7490	7.7770	7.8920
F1 slits [mm]	$\pm$64.2	-42/+64.2	-46/+64.2
$B\rho_{1,2}$ (D2) [Tm]	7.0260	6.9802	7.0372
F2 slits [mm]	$\pm$4	$\pm$4	$\pm$4
$B\rho_{3,5}$ (D3, D4)[Tm]	7.0162	6.9625	7.0543
F5 slits [mm]	$\pm$120	-120/+60	-120/+75
$B\rho_{5,7}$ (D5,D6) [Tm]	6.8002	6.7306	6.7992
F7 slits [mm]	$\pm$70	$\pm$30	$\pm$70
Total F8 rate [kpps]	$\sim$ 6	$\sim$ 5	$\sim$ 5.5
Beam centered at ZeroDegree	**^{66}Cr**	**^{72}Fe**	**^{78}Ni**
$B\rho_{8,9}$ (D7) [Tm]	5.8300	5.6168	5.6020
$B\rho_{10,11}$ (D8) [Tm]	5.8230	5.5960	5.5914
Total measurement time [hours]	22.5	24.5	$\sim$ 120

Table 3.4: Summary of the parameters used in each setting. All the $B\rho$ values were calculated with LISE++ and optimized in-beam. The values reported correspond to the final values for each setting.

and the energy loss in the target was calculated between 50 MeV/u and 100 MeV/u, depending on the nuclei. Detailed information on the rate of the isotopes of interest is given in Chapter 4.

This thesis is focused in the inelastic proton scattering from neutron-rich Ni and Zn isotopes. From Setting 1, ^{70}Ni was studied, from Setting 2, ^{72,74}Ni as well as ^{76}Zn were analyzed, and from Setting 3, ^{78,80}Zn were investigated. As noted in Table 3.4, Setting 3 lasted about 5 days. As the statistics for the Zn isotopes were quite high, and the energy calibration of DALI2 was slightly shifting during the beam, data from only 1.5 days were used in the analysis corresponding to Setting 3.

CHAPTER 4

DATA ANALYSIS

This Chapter describes all the data analysis procedures that were performed. The calibration of the detectors placed along the BigRIPS and ZeroDegree separators is described in Section 4.1. Section 4.2 shows the particle identification performed as well as its optimization. The DALI2 calibration is described in Section 4.3 and the calibration of MINOS is reported in Section 4.4. The final particle gates applied and a description of the characteristics of the selected isotopes are presented in Section 4.5. Different gates applied to the data in order to reduce the background are shown in Section 4.6. Section 4.7 describes the Doppler correction applied on the γ-rays measured by DALI2 for the selected isotopes. Section 4.8 gives a detailed explanation on the simulation of the response of DALI2 which was used to fit the experimental spectra.

4.1 BigRIPS and ZeroDegree calibrations

4.1.1 Position measurement with the PPACs

The x and y positions of the particles at each PPAC were determined using Equation 3.20. The constants k_x and k_y take into account both the electronics conversion from channels to nanosecond (0.09765 ns/ch for the MhTDC used) as well as the conversion from nanoseconds to millimeters (around 1.25 mm/ns). The offsets X_{offset} and Y_{offset} take into account an offset due to the length of the cables, an offset due to

the delay line of each PPAC and an offset due to the alignment of the PPAC in the beam line. The total offset applied to each PPAC was in the order of 2 mm.

Inconsistent events were removed by making a selection on T_{sumX} and T_{sumY}. Figure 4.1 shows examples of T_{sumX} distributions for the first PPAC at the F7 focal plane (F7 PPAC 1A) and the last PPAC at the F11 focal plane (F11 PPAC 2B). Three settings are plotted in the Figure. Although a difference in shape can be observed, the position of the peak was the same for the three Settings. This difference in shape could be due to a modification of the beam intensity, a change in the thresholds used in the electronics, or a reduction in the PPACs efficiency. As the peak corresponds to consistent events, a gate around it was applied to reject invalid events from the analysis. The same gate was used for all the Settings and two possible ways to select it were studied. In the first approach, the minimum and maximum of the distribution were selected "by-eye", while in the second approach, a Gaussian function was fitted to the peak and a range of $\pm 3\sigma$ around the centroid was chosen. Panel a) of Figure 4.2 shows an example of these two possibilities for selecting the gate. The red area corresponds to the valid events following the first approach and the black area corresponds to the events that were taken into account using the second approach. The average loss of events when

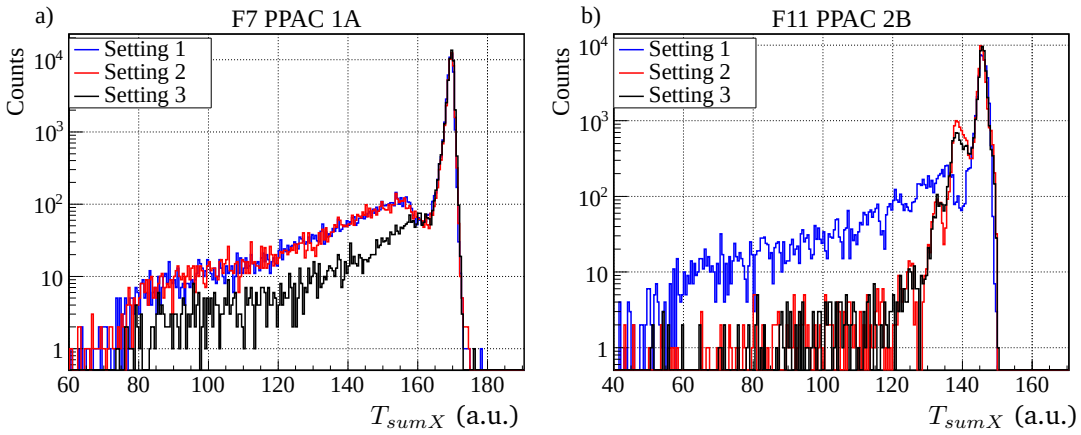

Figure 4.1: Examples of T_{sumX} plots for a) the first PPAC at F7 and b) the last PPAC at F11. It can be seen that the range of valid events did not change between the settings. In the case of F11 PPAC 2B, a change in the response of the signals can be seen, but the range of valid events remained the same. Each plot was made with 50000 events taken at the middle of the setting.

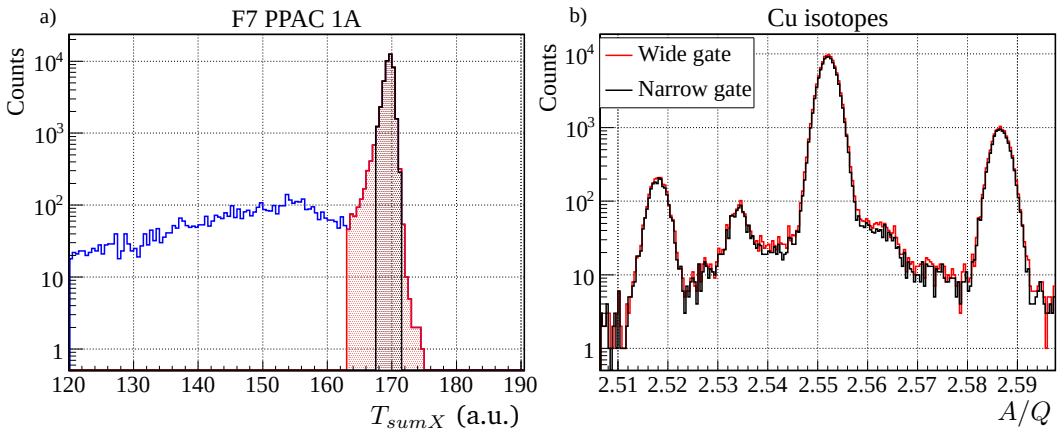

Figure 4.2: Examples of the possible T_{sumX} gates. The red area corresponds to the case of choosing the minimum and maximum of the distribution, while the black area corresponds to a $\pm 3\sigma$ gate around the centroid of the peak, after a Gaussian function was fitted.

selecting the $\pm 3\sigma$ gate was 3.9%. Panel b) of Figure 4.2 shows the effect the two gates have in the A/Q (F5-F7) of the incoming Cu ions. Details on the calculation of A/Q are given in Section 4.2. Although an improvement in resolution when selecting the narrower gate can be seen, it was small compared to the events which were lost. For BigRIPS, the relative improvement on A/Q obtained with the narrow gate was around 1.6%, but around 7% of the events were lost in the reconstruction. For ZeroDegree, an improvement in the resolution below 1% was obtained with about 1.5% of the events lost. Because of this, a wide gate for selecting consistent events in all the PPACs was taken.

Another important property of a PPAC is its efficiency. As it is dependent on the atomic number of the measured particle, a single element was selected for the analysis. For Setting 1 Mn was selected, for Setting 2 Co was chosen, and for Setting 3 Cu was taken, as these were the centered isotopes. The efficiency of each PPAC along BigRIPS was calculated as the number of valid events, compared to the total number of particles measured in the F7 TEGIC. For the PPACs along ZeroDegree, the efficiency was determined in the same way, but taking into account the total number of particles detected in the F11 TEGIC. Figure 4.3 shows the average efficiency of all the PPACs for the three settings. It can be seen that the efficiency of all of them was above 80%, and in most cases above 90%. The drastic increase in the efficiency of the BigRIPS PPACs

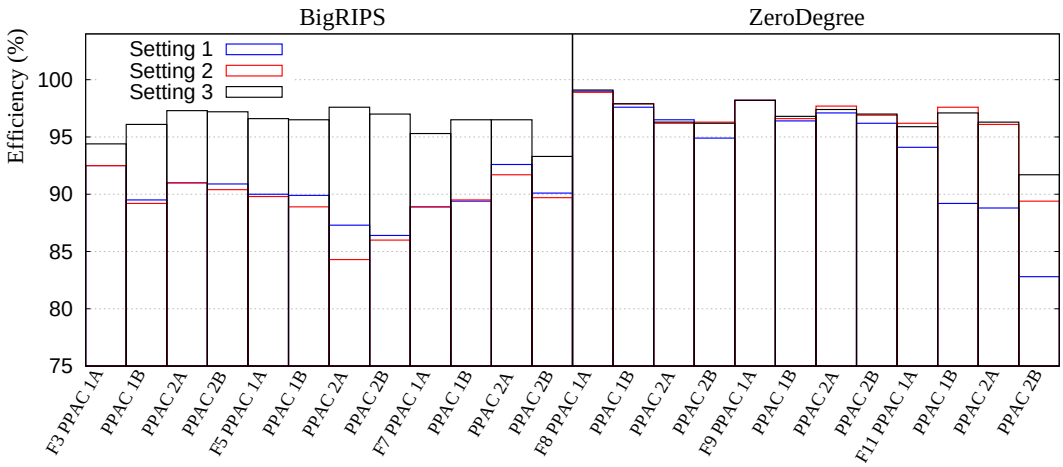

Figure 4.3: Efficiency of the PPACs for the three Settings. All the PPACs had an efficiency higher than 80%. The increase of efficiency in the BigRIPS PPACs for Setting 3 was due to a change of the thresholds applied to the discriminators performed between Setting 2 and Setting 3.

in Setting 3 was due to an adjustment of the threshold of the PPACs discriminators performed at the beginning of Setting 3. Using the position given by the PPACs, the position of the particle in each focal plane was reconstructed using a linear fit. It is important to note that to perform this tracking, at least two PPACs were required, thus possible losses in efficiency were compensated.

4.1.2 Time-of-Flight measurements with the plastic scintillators

The ToF was measured using plastic scintillators placed along the beam line. As a first check on the performance of the detectors, the validity of Equation 3.15 was checked. Figure 4.4 shows a plot of $t_2 - t_1$ vs $\ln(q_1/q_2)$ for each scintillator. Data were taken from Setting 2 and were similar for the three settings. Each panel in the plot corresponds to a different plastic detector. A clear correlation can be seen between the two quantities, indicating the consistency of the events. Some background, corresponding to the events where more than one particle hit the plastic, can be seen. To discard such events from the analysis, it was possible to take advantage of the MhTDC used to read out the plastic detectors: In a MhTDC, all the events arriving in a certain time window around the trigger-time are recorded. Most events had a single hit in each PMT, nevertheless some events were recorded with a hit-multiplicity bigger than one. Figure 4.5 shows

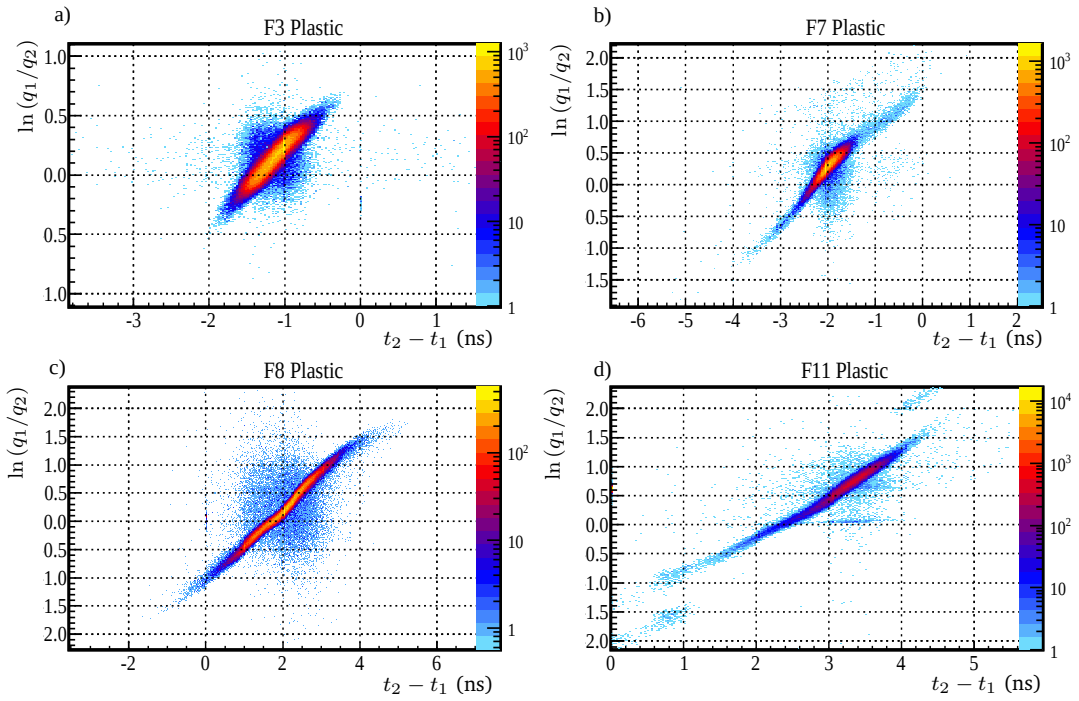

Figure 4.4: Check of consistency for the plastic scintillators at F3, F7, F8 and F11. A correlation between $t_2 - t_1$ and $\ln(q_1/q_2)$ can be observed, showing that the events come from a single particle. Some background can be seen in each plastic, which correspond to events when more than one particle hit the plastic. Data were taken from Setting 2.

an example of the effect of removing those high multiplicity events. Panel a) shows the consistency check for the F8 plastic detector using all the hit-multiplicities. Panel b) shows the effect of selecting events which have only one hit in each one of the PMTs. The events rejected amounted for about 2% of the total number of events. This requirement was applied to the four plastic scintillators for the rest of the analysis. The time at which a particle passed through the plastic detector was determined as the average of the times measured by the left and right PMTs. The ToF along BigRIPS (ToF_{37}) and ZeroDegree (ToF_{811}) were calculated as described in Equation 3.17. The calibration parameters TimeOffset(37) and TimeOffset(811) take into account all the delays in the electronics and were selected in such a way that the A/Q calculated for the isotope of interest corresponded to the theoretical value. Figure 4.6 shows an example of how this calibration was performed for Setting 1. Panel a) shows the A/Q spectra for Ni isotopes identified in ZeroDegree when a certain value of offset was applied (-162 ns

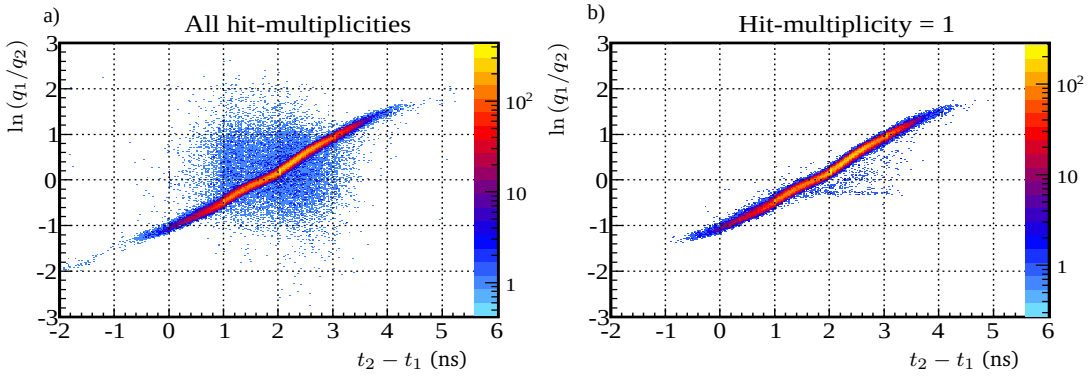

Figure 4.5: Rejection of background events in the plastic detectors. As an example, the F8 plastic scintillator is shown. Panel a) shows the consistency check for all the hit-multiplicities, while panel b) shows the effect of selecting events with only one hit recorded in the MhTDC. Data were taken from Setting 3.

in the example). A Gaussian function was fitted to the isotope of interest to obtain the centroid of the distribution. The same procedure was applied with different values of the TimeOffset in order to perform a linear interpolation, as shown in Panel b) of Figure 4.6. The correct value of A/Q of the isotope of interest was used to obtain the most appropriate offset. For Setting 1, the offset was selected to reproduce the A/Q of ^{70}Ni, for Setting 2 ^{74}Ni was used and for Setting 3 ^{80}Zn was selected.

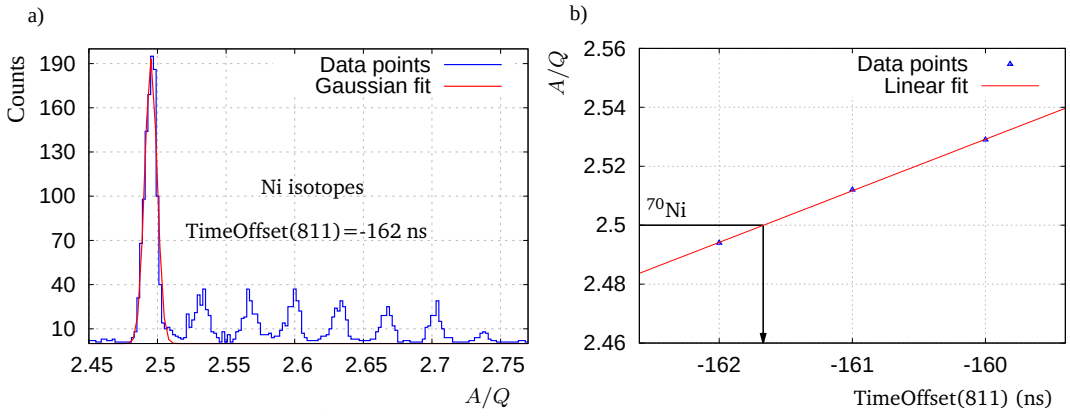

Figure 4.6: Selection of the time offset parameters. Panel a) shows the Ni isotopes identified in ZeroDegree. A Gaussian function was fitted to obtain the centroid for a particular isotope, in this case ^{70}Ni. Panel b) shows the variation in the centroid as TimeOffset changes. A linear fit was performed to obtain the offset.

4.1.3 Atomic number measurement with the TEGICs

The Z measurement was performed as explained in Section 3.2.3.1, using Equation 3.11. A geometrical average of the fired anodes was taken as the energy loss in each TEGIC. The calibration parameters K_1 and K_2 were obtained by a linear fit between the uncalibrated data and the correct Z values. Figure 4.7 shows an example of this procedure for the F11 TEGIC in Setting 1. Panel a) shows the uncalibrated data and a Gaussian fit performed in each peak to obtain its centroid. Panel b) shows the linear calibration done using those centroids and the known values of Z for each isotope. The same procedure was applied to the three settings.

After the calibration, a slight dependence of Z on the velocity was observed. Panel a) of Figure 4.8 shows the dependence of Z on β_{811} for the case of the F11 TEGIC in Setting 2. A linear fit was performed to correct for this dependence. Panel b) shows the same plot after the correction. A similar correction was performed to each TEGIC in each Setting.

Particular care has to be taken in the calibration of the TEGICs, as the energy lost by the particles on the gas depends on its temperature and pressure. To quantify the drift in the measured Z value, different runs along each setting were taken and the centroid of the Z distribution was measured. For Setting 1 $Z = 27$ was used, for Setting 2 $Z = 29$ was used and for Setting 3 $Z = 31$ was selected. The difference between

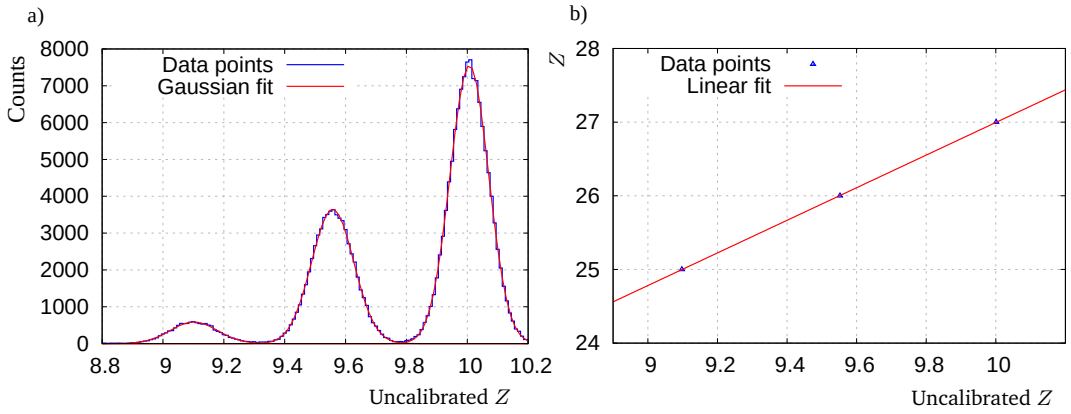

Figure 4.7: Example of the TEGIC calibration. Panel a) shows the Gaussian fit to uncalibrated data. Panel b) shows the linear fit used to obtain the calibration parameters. The data correspond to the F11 TEGIC from Setting 1.

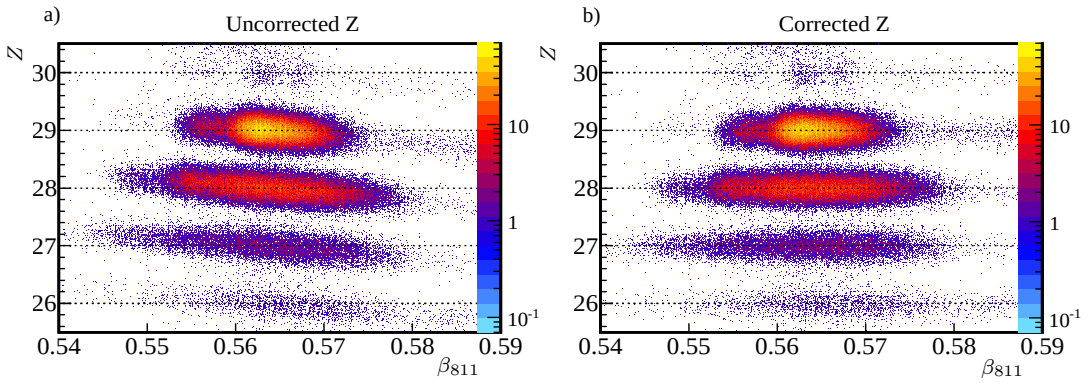

Figure 4.8: Correction of the β dependence in the TEGICs. Panel a) shows the dependence of the Z measured in the F11 TEGIC on β_{811}. A linear fit was performed to remove this dependence. Panel b) shows the same data after the correction was applied. Data were taken from Setting 2.

the measured value and the theoretical value was calculated for each run. Figure 4.9 shows this drift on the Z value for different run numbers. Both the F7 and the F11 TEGICs are shown. It can be seen that the F7 TEGIC was more stable than the F11 TEGIC. Nevertheless, for all the cases the drift was below 0.2%. No further correction was applied to this drift as it was below the achievable Z resolution.

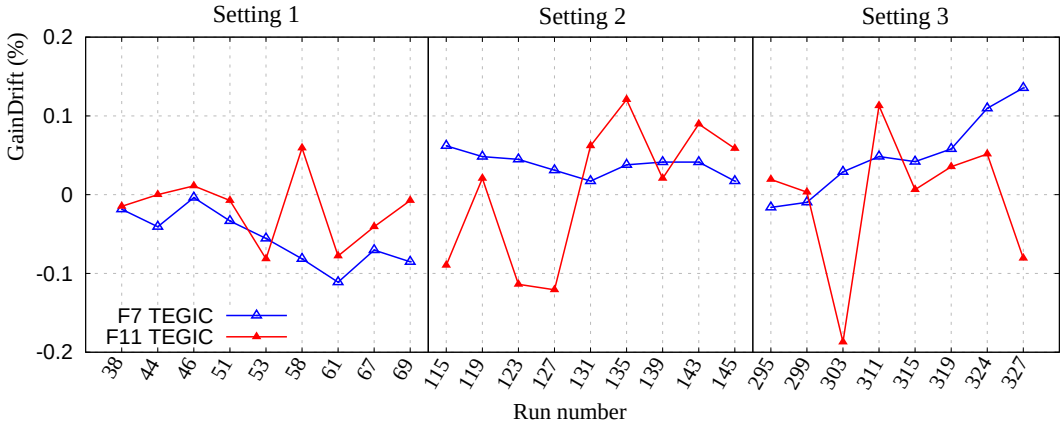

Figure 4.9: Gain drift in the TEGICs for the three Settings. The y axis represents the difference (in percentage) from the measured value to the theoretical value. In all the cases, the variation was below 0.2% and no correction was applied.

4.2 Particle identification

Using the calibrated information from the different detectors, the particle identification (PID) was performed. Different values of A/Q could be obtained by taking into account different combinations of magnetic rigidities and velocities. For BigRIPS, three values of A/Q could be obtained: The first one was calculated taking into account the two magnetic stages, from F3 to F5 and from F5 to F7, (F3-F7), and the change in velocity due to the degrader as discussed in Section 3.2.3.4. The second value was obtained by using only the first magnetic stage (F3-F5) and the velocity β_{35} calculated using Equation 3.23. The last value was obtained by taking into account only the second magnetic stage (F5-F7) and β_{57}, calculated using Equation 3.24.

For the case of ZeroDegree, it was also possible to obtain three different values of A/Q in an analogous way. The first value considered the magnetic stages from F8 to F9 and F9 to F11 (F8-F11), the second took into account only the first stage (F8-F9) and third value considered only the last magnetic stage (F9-F11). In the three cases, the velocity β_{811} was used.

Figure 4.10 shows a comparison of the different A/Q values obtained in BigRIPS and in ZeroDegree for Zn isotopes of Setting 3. For BigRIPS, it can be seen that the best resolution was achieved when only the second magnetic stage (F5-F7) was used,

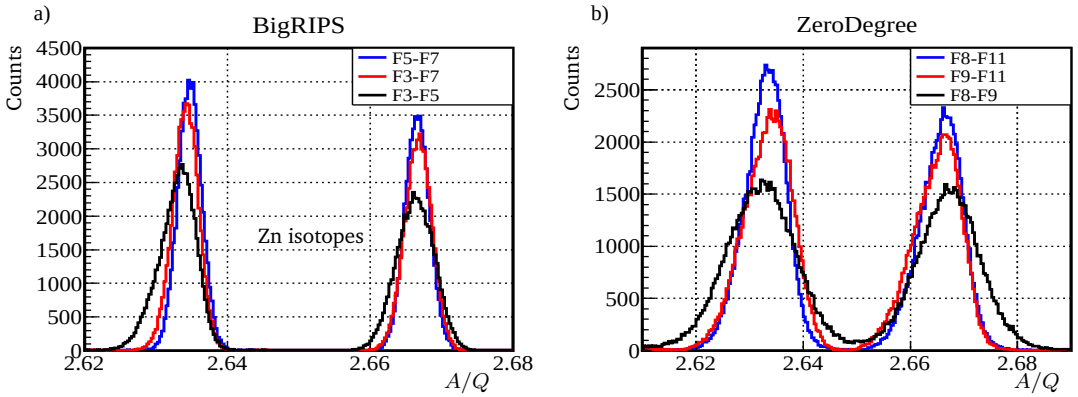

Figure 4.10: Example of the use of different magnetic stages to calculate A/Q. The distributions obtained for BigRIPS and ZeroDegree with different combinations of magnetic rigidities and velocities are shown for Zn isotopes of Setting 3. For BigRIPS, a better resolution was achieved by using the F5-F7 stage, while for ZeroDegree use of the F8-F11 stage showed a better resolution.

while the worst resolution was achieved when using only the first stage (F3-F5). An intermediate resolution was observed for the A/Q calculated using F3-F7. A probable cause of the decrease in resolution when using only the first stage is some damage in the F3 PPACs. For ^{80}Zn, the resolution improved by almost 27%, when going from the F3-F5 value to the F3-F7 one, and a further improvement of 9.5% was obtained when using the F5-F7 value. The number of counts in the ^{80}Zn peak decreased by less than 1% between the different possibilities. Is worth noting that the PID efficiency is mainly related to the PPAC efficiency.

For ZeroDegree, the lowest resolution was obtained when using only the first magnetic stage. This was equivalent to what was observed for BigRIPS. Nevertheless, in this case, the best resolution was achieved when using both magnetic stages. This can be attributed to the fact that the PPACs at F9 were the only matter between the two magnetic stages and then the double $B\rho$ measurement increased the accuracy of A/Q. This was not the case for BigRIPS due to the F5 degrader. The resolution improved by about 24% when going from the F8-F9 value to the F9-F11 one, and an extra 10% was obtained when using F8-F11. The difference in the total number of counts between the peaks was below 1%.

The fact that the number of counts did not decrease when using different magnetic stages, and thus different PPACs, was probably due to the fact that the analysis code still required information in all the focal planes to perform the analysis. Improvements of the code in this sense, which could improve the detection efficiency, are out of the scope of this thesis. For the rest of the analysis, the values of A/Q which showed better resolution were used.

For the case of BigRIPS, the identification required no further corrections. For ZeroDegree, the optical matrices used were not enough to compensate for aberrations and higher order matrix elements could be used to get a better A/Q resolution. In order to correct this optical aberrations, the dependence of A/Q with the position and angle of the particles at F9 and F11 focal planes was performed. Figure 4.11 shows an example of this procedure. In panel a) the dependence of A/Q with the particle angle, measured at F11, can be clearly seen. The data correspond to Setting 3 and a cut in Zn isotopes was applied. In order to improve the A/Q resolution for the isotopes of interest, a polynomial function was fitted to the two-dimensional plot and subtracted from the A/Q. The result of the correction can be seen in panel b) of Figure 4.11. A

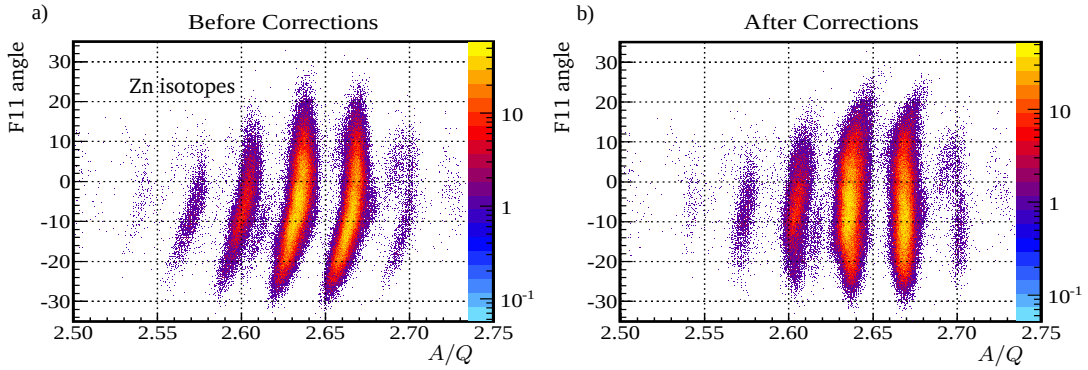

Figure 4.11: Example of the corrections applied to A/Q in ZeroDegree. Panel a) shows the dependence of A/Q of outgoing Zn isotopes on the measured F11 angle. A polynomial function was fitted to the 2D plot and subtracted from the A/Q. The result of this procedure is shown in Panel b).

similar procedure was applied to correct the dependence of A/Q with the F9 position, F9 angle and F11 position. In each case, a polynomial of different order was chosen to obtain the best correction. The procedure was performed independently for each of the three Settings.

An example of the improvement in A/Q achieved after this corrections for Setting 3 can be seen in Figure 4.12. The left panel shows the PID obtained in Zero Degree using the information of different detectors without any modification. Panel b) shows the resulting PID after correcting the dependence of A/Q on the position and angles along ZeroDegree. A clear improvement in the resolution can be observed. Nevertheless, as the correction was performed for the isotopes of interest, a small offset for other isotopes was observed. This was particularly true for Setting 2: As all the optimizations were performed for the Ni isotopes, in particular for ^{74}Ni, an offset of around 0.1 was obtained in the A/Q of ^{76}Zn. The final identification plots for each Setting, together with the particle gates used to select (p, p') channels will be shown in Section 4.5.

Table 4.1 shows the average values of A/Q and Z resolution obtained for the isotopes of interest in the BigRIPS and ZeroDegree spectrometers. The A/Q resolution corresponds to $\frac{\delta(A/Q)}{A/Q}$ and the Z resolution is, in an equivalent way, defined as $\frac{\delta Z}{Z}$. In both cases, the variation reported corresponds to the σ of the distribution. The error reported is the standard deviation of the experimental values. The numbers obtained are within the expected values of each spectrometer.

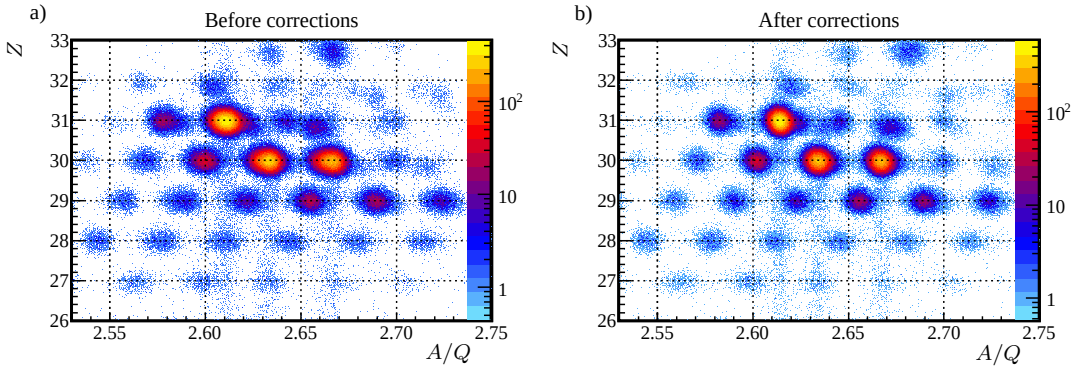

Figure 4.12: Example of the improvement of the ZeroDegree identification. Panel a) shows the PID without any improvement. Panel b) shows the effect of correcting the dependence of A/Q in the positions and angles. Data were taken from Setting 3.

	BigRIPS	**ZeroDegree**
A/Q resolution (%)	0.073(8)	0.14(3)
Z resolution (%)	0.85(5)	0.47(2)

Table 4.1: Resolution obtained for the particle identification (σ). In all the cases, the average among all the isotopes of interest is shown together with an error given by the standard deviation of the data points.

4.3 DALI2 calibration

4.3.1 Energy calibration

The energy calibration of the 186 NaI(Tl) crystals composing the DALI2 array was performed using three standard γ-sources: ^{88}Y, which emits a 898 keV and a 1836 keV γ-rays; ^{137}Cs with a transition at 662 keV and ^{60}Co, with γ-rays at 1173 keV and 1332 keV. Two calibrations were performed for each Setting. For the case of Settings 1 and 3, the calibrations were performed at the beginning and at the end of the Setting. For Setting 2, a calibration was also performed during a beam stop period shortly before the middle of the Setting. All the calibrations were performed by placing the sources, one by one, at the end of the MINOS beam pipe. Each calibration lasted about 30 min, and in some cases not all the calibration sources were used.

The photopeaks observed in each detector corresponding to the transitions of the calibration sources, were fitted with the sum of a Gaussian function and a second order

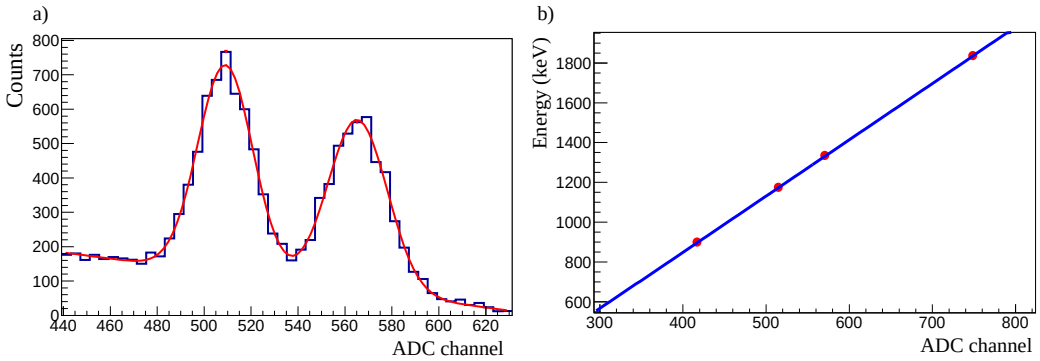

Figure 4.13: Example of the DALI2 calibration. Panel a) shows the raw data of a detector when the ^{60}Co source was placed inside the array. Two Gaussian functions and a second order polynomial were fitted to the data to obtain the centroids of the peaks. Panel b) shows the linear fit performed using the centroids of different transitions and the corresponding known energy.

polynomial in order to obtain their centroids. The condition that only one DALI2 crystal was hit per event was applied to reduce the multiple Compton scattering in the array. Panel a) of Figure 4.13 shows an example of the fit performed on the raw data when the ^{60}Co source was placed. Once all the centroids were obtained, a linear calibration was performed between these values and the know energy of the transitions. Panel b) of Figure 4.13 shows an example of such a linear calibration. Two detectors presented bad performance since the beginning of the experiment and were removed from all the analysis: Detector number 133, which did not give any signal, and detector number 64, which showed a gain drift so large that in some cases it was impossible to distinguish any photopeak.

The gain drift observed in the DALI2 crystals is due to different factors: First, the PMTs used to read-out the crystals are sensitive to the magnetic field of the dipole and quadrupole magnets placed nearby. Because of this, a slight change in the calibration was expected for different Settings. Second, the damage caused in the detectors by highly energetic particles passing through them can affect the amount of light that is collected by the PMT and thus affect the calibration. Apart from this, the PMT itself can present some damage causing a variation in its output pulse.

In order to study the gain drift in DALI2, the calibration of each detector before and

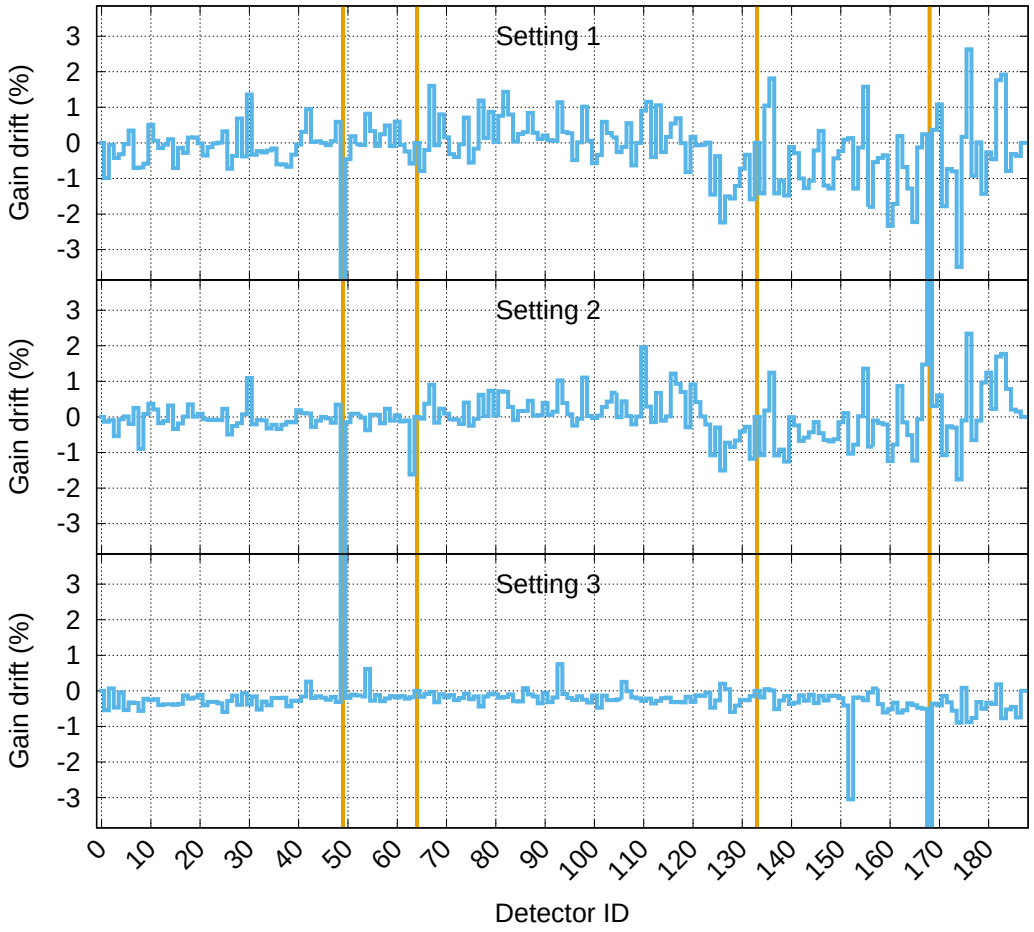

Figure 4.14: Gain drift of the DALI2 crystals. The difference in percentage between the ADC channel corresponding to 1 MeV before and after the Setting is plotted for each detector. Results obtained for the three Settings are shown. The vertical lines show the detectors removed from the analysis.

after each Setting was obtained and the gain drift was calculated using the formula

$$\text{Gain drift (\%)} = \frac{\text{ADC}_{\text{after}} - \text{ADC}_{\text{before}}}{\text{ADC}_{\text{before}}} \times 100\%, \tag{4.1}$$

where $\text{ADC}_{\text{before}}$ $\text{ADC}_{\text{after}}$ represent the ADC channel corresponding to 1 MeV before and after the Setting.

Figure 4.14 shows the gain drift of each detector for the three Settings. The upper panel shows the drift for Setting 1, the central panel for Setting 2 and the bottom panel shows the result for Setting 3. The y scale has been fixed to the range between

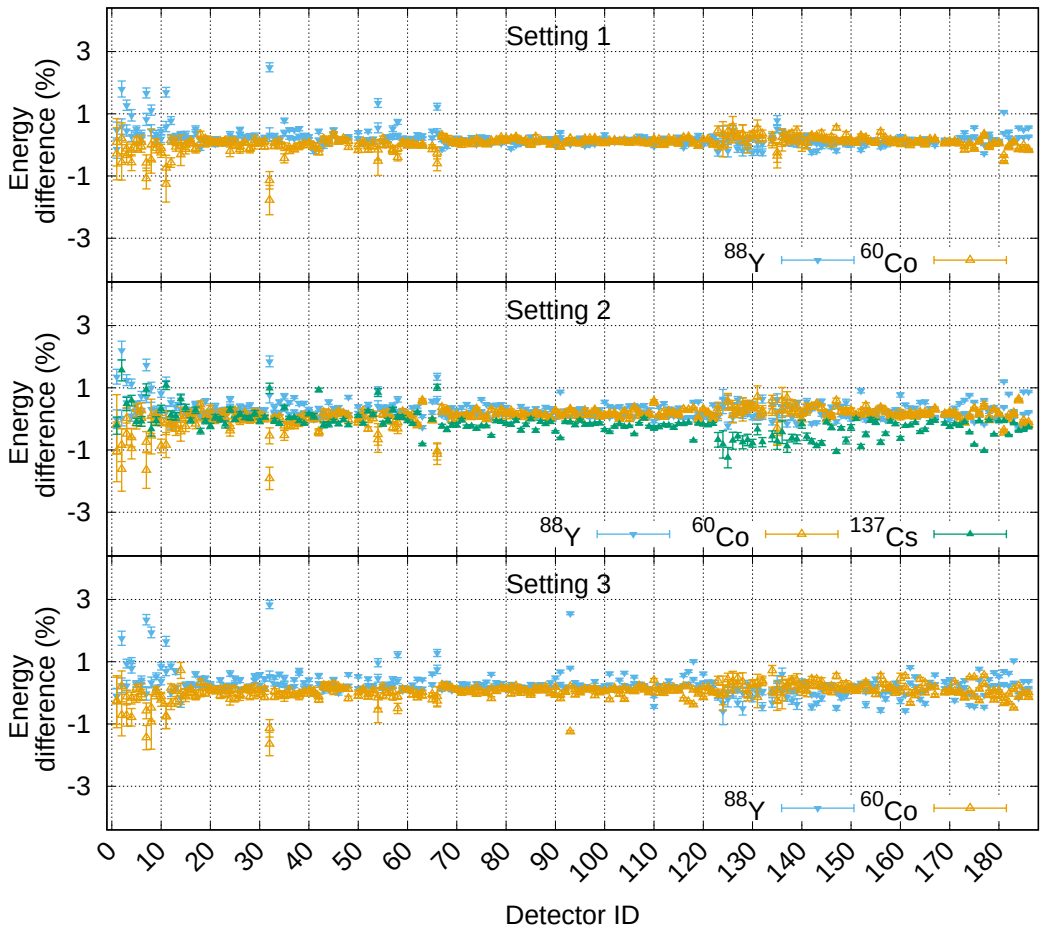

Figure 4.15: Energy difference between the expected and measured value after calibration. Data from the three Settings are shown. Most detectors show a difference below 2%.

-3.5% and 3.5%. It can clearly be seen from the plot that detectors 49 and 168 had a considerable drift in the three Settings. Although not shown in the plot as they are out of scale, the drift for these detectors was at least 5% and at most above 200%. These two detectors were removed completely from the analysis. It is also seen that the stability of the array improved when going from Setting 1 to Setting 3, where most detectors have less than 1% drift. The vertical lines in Figure 4.14 show the four detectors removed from the analysis. As most of the remaining detectors showed a gain drift below 3%, a single calibration file was used for each Setting. In the case of Settings 1 and 3, the calibration made before the Setting was used and for Setting 2,

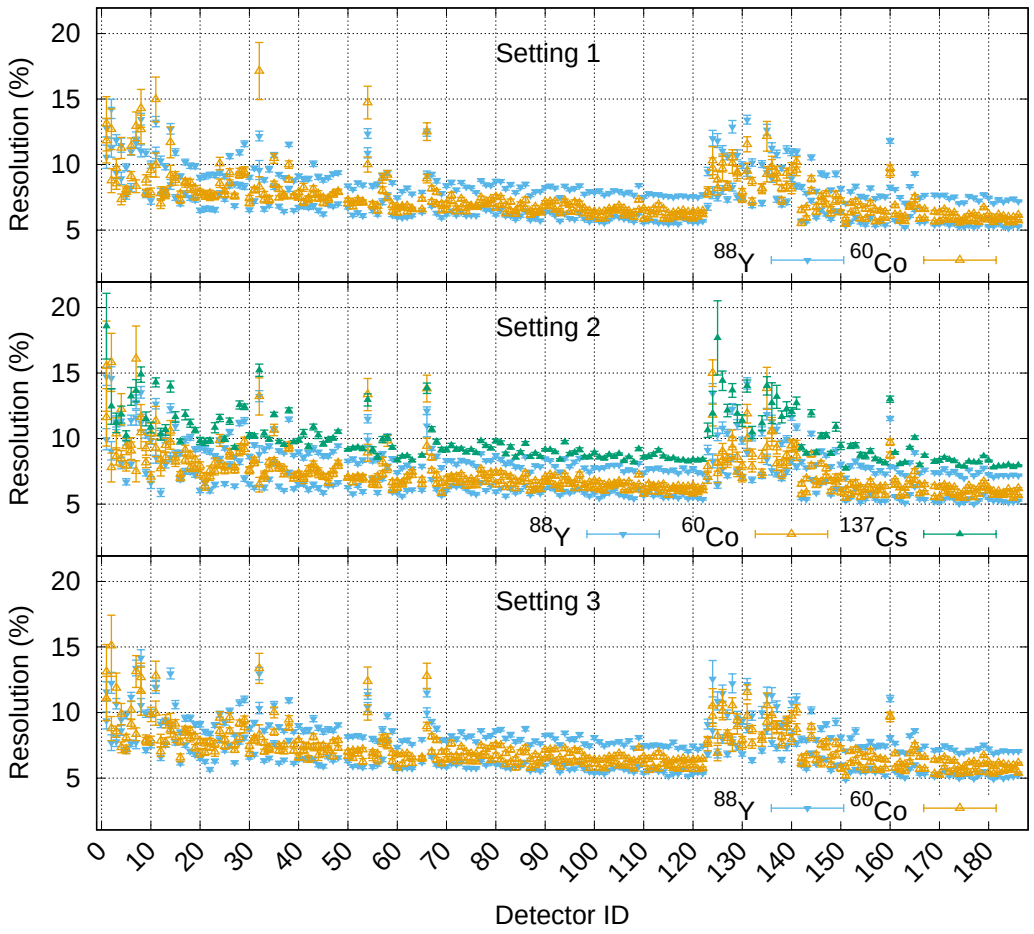

Figure 4.16: Resolution of the DALI2 crystals. Data from the three Settings are shown. For most crystals a resolution below 15% was obtained for the 661keV transition of the ^{137}Cs source.

the calibration made during the beam stop was utilized.

In order to check the goodness of the calibration, the position of the peaks were determined for each source after calibration. This was done by fitting a Gaussian function together with a second order polynomial to each peak. The difference between the value obtained in such a way and the expected value was calculated. Figure 4.15 shows the results obtained for each Setting. It can be seen that for the three Settings, most detectors show a difference below 2%. Even further, with exception of detectors 1 to 15, most of them have an energy difference below 1%. Detectors 1 to 10 correspond to the first layer of DALI2 and are more severely affected by possible radiation damage

from upstream particles hitting the detectors. A particular behavior can be observed for detector 32, which shows a relatively high energy shift compared to neighboring detectors in the three Settings.

The resolution (FWHM) of each detector was also checked for the different calibration sources. Figure 4.16 shows the results obtained for each Setting. The expected dependece on the transition energy is clearly visible and most crystals had a resolution below 15% for the 662 keV line of the ^{137}Cs source Here again, it can be seen that detectors 1 to 12 had a poorer performance. It can also be seen that some detectors between 121 and 145 presented a worsening of the resolution. These detectors were positioned in areas of the array that were shadowed by the previous layer and did not contribute much to the overall resolution. In addition, four detectors showed a worse resolution than expected: Detectors 32, 54, 66 and 160. As detector 32 also showed a considerable energy shift, it was also removed from the analysis.

The number of optical photons produced in a scintillator is proportional to the energy deposited by the γ-ray. Thus, the width of each photopeak is expected to vary proportionally to the square root of the energy (66). A non-linear response of the detector, in particular for low energies, can give rise to a small deviation from the square root behavior. The dependence of the resolution on the energy was modeled by the power formula

$$\text{FWHM} = k_1 \times E^{k_2}. \tag{4.2}$$

The parameters k_1 and k_2 were found independently for each crystal in each Setting. The values of k_1 varied between 1 and 5, while the value of k_2 was centered around 0.6. This individual crystal resolution was used as input of the Monte Carlo simulation, which will be explained in Section 4.8. Panel a) of Figure 4.17 shows the final spectrum of all the calibration sources for Setting 2. No normalization has been performed. Panel b) shows the resolution of the full array as a function of energy. The fit performed to the data points is also shown. The results obtained are in reasonable agreement with the resolution quoted for the array (71).

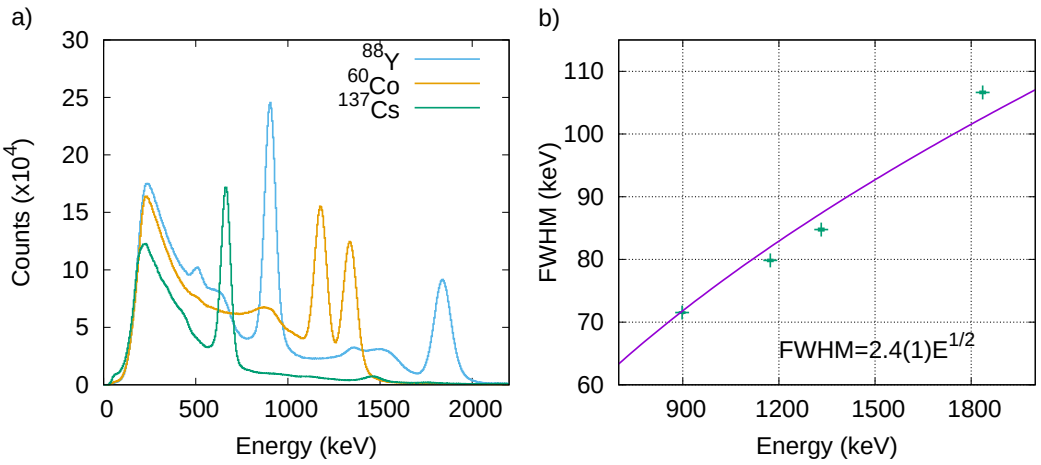

Figure 4.17: Resolution of the DALI2 array. Panel a) shows the spectra off all the calibration sources for Setting 2. Panel b) shows the dependence of the resolution on the energy. The fit performed to the data is also shown.

4.3.2 Time calibration

The time signals from each crystal were aligned to each other to obtain the timing of the array. In this case, the information of different hits was not taken into account and only the first hit was considered for each detector. This alignment was performed only for signals arising from an energy deposition above 500 keV. Figure 4.18 shows a typical time spectrum obtained from one crystal. As shown in the Figure, a Landau distribution was fitted to the spectrum to obtain the centroid of the distribution. This procedure

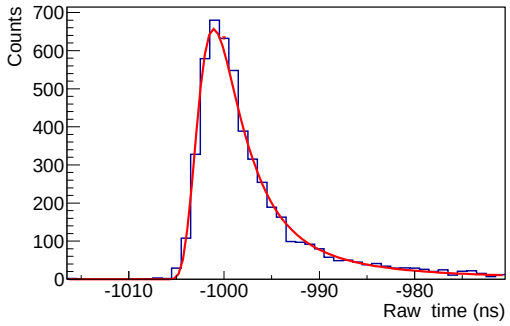

Figure 4.18: Typical time spectrum of a DALI2 crystal. A condition on the energy of the γ-rays to be higher than 500 keV was applied. A Landau function was fitted to the spectra of each crystal to get the centroid.

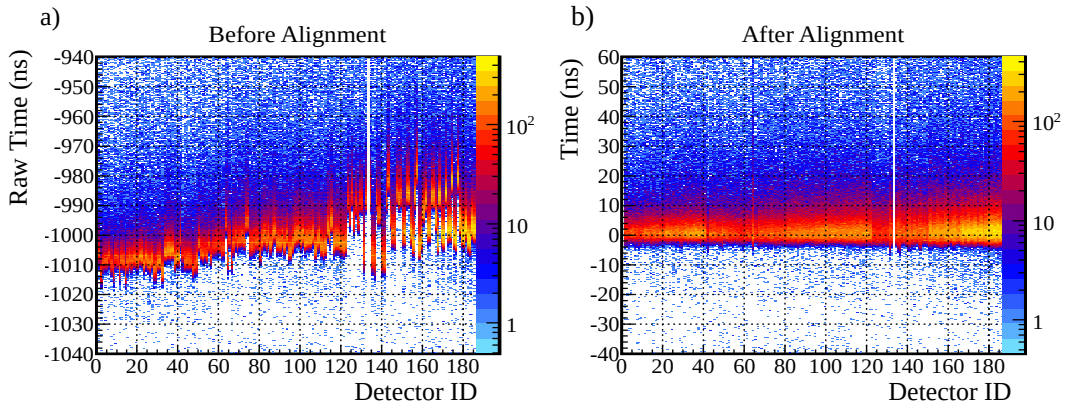

Figure 4.19: DALI2 time calibration. Panel a) shows the uncalibrated spectra. Panel b) shows the result obtained after aligning every crystal to zero. Events with detected energy higher than 500 keV were considered to avoid time walk at low energies. Data were taken from Setting 2 and were similar for the three Settings.

was applied independently for each crystal and each Setting. The centroid of the distribution was subtracted from the time spectrum of every crystal to center it around zero. The result of the calibration procedure can be seen in Figure 4.19. Panel a) of shows a two-dimensional histogram of the raw time spectrum of each crystal. It can be seen that the distribution of the different channels was not aligned. Panel b) shows the same plot after the time alignment was performed. The data were taken from Setting 1 and were similar for all the Settings.

4.4 MINOS calibration

The MINOS calibration was performed by finding the time t_0 and the drift velocity, v_{drift}, in Equation 3.27. While t_0 was a constant over the experiment, v_{drift} had to be obtained run-by-run. To do this, the distribution of drift times obtained during each run was used. Panel a) of Figure 4.20 shows a typical drift time distribution measured during one run. A selection of events having less than 10 pads hit per ring was made to remove sparks in the TPC as well as some background events (86). Electrons ionized near the MicroMegas detector should have a drift time equal to zero, while those ionized in the opposite end of the TPC have a drift time which corresponds to the length of the TPC (300 mm) divided by the drift velocity. These two times are indicated in

the Figure as t_0 and t_{max}. The t_0 was defined as the point where the initial rise of the distribution occurred, which could be seen by a kink in the data. To obtain t_{max}, a Fermi function was fitted to the falling edge of the distribution and the midpoint of the decay was taken. Using these two times, the drift velocity was calculated run by run. Panel b) of Figure 4.20 shows the drift velocity obtained for the three Settings. It can be seen that the three Settings had a small variation in the drift velocity. These changes depended on the local temperature and the amount of water impurities that were present in the gas. The big change observed during Setting 1 corresponds to a change in the gas bottle of MINOS. After the calibration was applied, the tracking algorithms described in Section 3.2.4 were used to obtain the interaction vertex, z_{vertex}. As this distribution reflects interactions of the particles in the target, its width should correspond to the target length. By determining the with of the distribution, it was possible to extract an effective target thickness of 102(2) mm and a mean density of $\rho = 70.973$ Kg/cm^3. The MINOS calibration for each Setting as well as the calculation of the target thickness and density were provided by the SEASTAR collaboration.

It is to note that MINOS was designed to have a high efficiency for mainly $(p, 2p)$ and $(p, 3p)$ reaction. The protons scattered off the target after a (p, p') reaction have large scattering angles and rather low energy transferred. Thus, the scattered protons

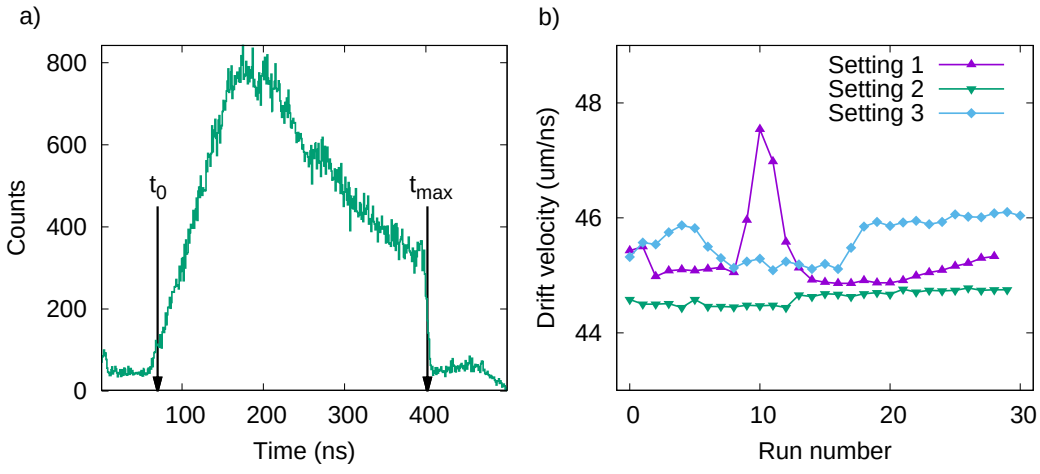

Figure 4.20: Example of the MINOS calibration. Panel a) shows a typical time distribution measured in MINOS. From this distribution, t_0 and t_{max} were extracted and used to calculate the drift velocity run by run. Panel b) shows the drift velocity calculated for each run. Data from the three Settings are shown.

stay mostly inside the liquid hydrogen target and do not reach the TPC due to the energy loss inside the thick target. This translates in a very low efficiency of MINOS for (p, p') reactions. All the cross sections were calculated without taking into account the vertex position information and assuming that the decay occurred at the center of the target. Although this entailed a decrease in the resolution, it was compensated by the increase in the efficiency.

4.5 Characteristics of the selected channels

Figure 4.21 shows the final BigRIPS and ZeroDegree PID plots obtained for all the Settings. In all the cases, the left plot corresponds to the BigRIPS PID and the right plot shows the ZeroDegree PID. The top plots display the final PID for Setting 1, the middle plot shows the PID for Setting 2 and the bottom row corresponds to Setting 3. The green circles in each plot show the particle gates used to select the isotopes of interest: ^{70}Ni from Setting 1, ^{72,74}Ni and ^{76}Zn from Setting 2 and ^{78,80}Zn from Setting 3.

To select the particle gates, the A/Q and Z distributions of each one of the isotope of interest were obtained, and a Gaussian function was fitted to each one to obtain the centroid and the width. An elliptical cut, centered in the centroid value of each distribution and having a radius of 3σ in each direction, was selected as the particle gate for each isotope. These cuts were used to select only (p, p') channels in each Setting before performing the γ-ray spectroscopy analysis.

Table 4.2 summarizes the characteristics of the selected channels. The total number of isotopes of each species, identified both in BigRIPS and ZeroDegree, was calculated as the number of F7DS triggers registered after performing the particle cuts, multiplied by the down-scale factor of the run. It is important to note that the values reported in the Table are an upper limit on the available number of isotopes. This number decreased because different gates applied to the data in order to reduce the background as will be explained in Section 4.6. The second column of the table shows the mean value of the x position at the F9 focal plane. Taking into account that the acceptance of ZeroDegree at F9 focal plane was ± 120 mm, it is visible that ^{78}Zn and, in particular, ^{70}Ni are in the edge of the acceptance of the spectrometer. The last column of the table shows the energy of the isotopes at the entrance of the target, E_{b}. This energy was calculated using LISE++ by taking into account the velocity measured in ZeroDegree

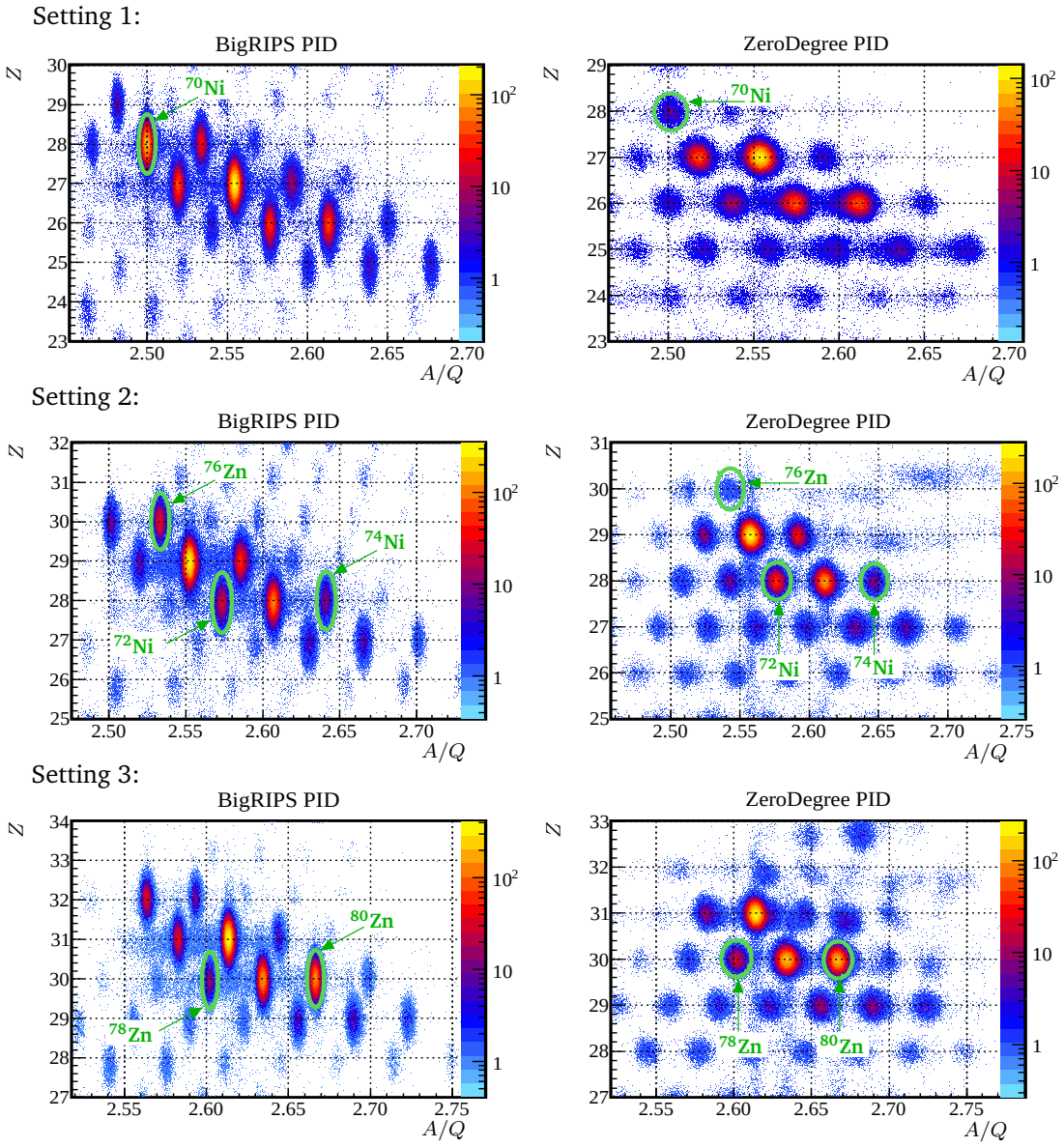

Figure 4.21: Particle identification plots for the three Settings. The left column shows the BigRIPS identification plot and the right column corresponds to the ZeroDegree identification plot. The green circles show the particle gates used for each one of the isotopes of interest. These plots do not contain the full statistics of the experiment.

and the energy loss of the isotopes in each element between the F8 plastic and the exit of the first SQT. The density of the target used for the calculation was chosen to be in agreement with the measured value reported in Section 4.4.

	Total ions	x(F9) (mm)	E_b (MeV/u)
^{70}Ni	582960	97.39	287.00
^{72}Ni	5018715	54.08	271.00
^{74}Ni	1619460	39.82	263.50
^{76}Zn	159030	72.57	275.50
^{78}Zn	951960	88.68	268.00
^{80}Zn	9571520	54.06	263.40

Table 4.2: Characteristics of the selected isotopes. The first column shows the total number of isotopes identified in both BigRIPS and ZeroDegree. The second column shows the mean value of their position at the F9 focal plane and the last column shows the energy of the isotopes at the entrance of the target calculated using the velocity measured in BigRIPS.

4.6 Gates for background reduction

In order to remove unwanted events and decrease the background, different correlations were checked and suitable gates applied to each data set. As explained in Section 4.1.2, the hit multiplicity in the plastic scintillators was selected to be equal to one. This allowed to remove events with pile-up in the TEGICs and to clean the identification plot.

To avoid the presence of charge-states or reacted particles in the analysis, the correlation between the magnetic rigidity, $B\rho$, measured for each isotope before and after the F5 degrader was checked. If the particle passing the degrader only loses energy, the only change in the magnetic rigidity comes from the reduction in the velocity. In this case, the ratio between the $B\rho$ before and after the degrader is expected to be constant. On the other hand, events that pick up or lose an electron or react inside the degrader have a bigger change in magnetic rigidity and although a correlation is still present, the ratio between the two magnetic rigidities takes different values. Panel a) of Figure 4.22 shows the $B\rho$ correlation check for ^{72}Ni. The x axis shows the ratio between the magnetic rigidities before and after the degrader, $B\rho_0/B\rho_1$, and the y axis shows $B\rho_0$. A gate between $B\rho_0/B\rho_1 = 1.030$ and $B\rho_0/B\rho_1 = 1.036$ was applied to remove events that were not correlated. The total number of events rejected by this condition was 24.62%. It can be seen from the Figure that a double structure was still present among the selected events. No significant differences in the cross section calculation

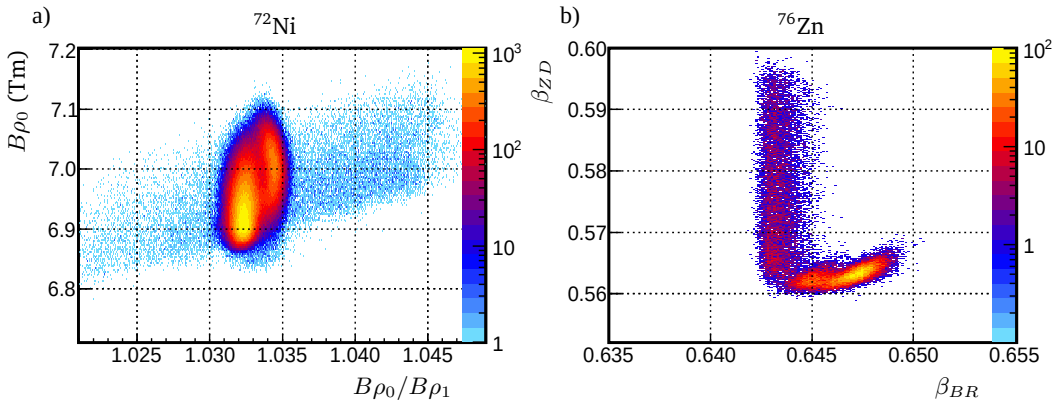

Figure 4.22: Gates for background reduction. Panel a) shows the $B\rho$ correlation checks for ^{72}Ni. Panel b) shows the correlation between incoming and outgoing particle velocities. In both cases, gates were applied to reduce the background.

were found by removing the second structure. Thus, avoid a reduction in the statistics, it was considered in the analysis.

The correlation between the incoming and outgoing velocities was also checked. If the particles cross the target, β_{BR} and β_{ZD} are expected to differ only by the amount of energy lost in the target. If the particles did not hit the target, this correlation was lost and the event should not be taken into account. Panel b) of Figure 4.22 shows β_{ZD} versus β_{BR} for ^{76}Zn. It can clearly be seen that some part of the events did not go through the target and show no correlation between the two velocities. It is also to note that this happened for the events with the smallest velocity measured in BigRIPS. The events that were not correlated were removed from the analysis. The total number of events rejected by this condition for ^{76}Zn was 30.33%. The two cases shown in Figure 4.22 are those with the highest number of events rejected by each condition. Table 4.3 shows the percentage of events rejected by each condition for each isotope. It is to note that the gates were applied sequentially. The last column of the table shows the final number of ions used for the analysis.

Isotope	Hits gate	$B\rho$ gate	β gate	Total (%)	Total ions
^{70}Ni	8.31	2.89	6.63	17.83	500300
^{72}Ni	1.99	24.62	0.00	26.62	3710865
^{74}Ni	2.17	1.29	0.92	4.37	1552020
^{76}Zn	2.04	1.28	30.33	33.64	102420
^{78}Zn	2.82	0.62	0.00	3.44	923200
^{80}Zn	2.84	0.88	0.57	4.30	9185360

Table 4.3: Percentage of events rejected from the analysis. Three gates were applied to all the settings: A selection of hit-multiplicity equal to one in all the plastic scintillators, a magnetic rigidity correlation gate to remove charge-states and a gate in the correlation between incoming and outgoing velocity to remove events that did not pass through the target. The last column reports the final number of ions used in the analysis.

4.7 Doppler correction

The γ-rays detected in the DALI2 array with an energy E_γ were Doppler corrected to obtain the emission energy, $E_{\gamma 0}$, using the relation

$$E_{\gamma 0} = E_\gamma \frac{1 - \beta \cos \vartheta}{\sqrt{1 - \beta^2}}, \tag{4.3}$$

where ϑ is the γ-ray emission angle in the laboratory frame of reference and β is the velocity of the particle at the moment it emits the γ-ray. Due to the high velocities of the projectiles, it was assumed that the incoming particles experienced a negligible change on the direction of motion after the proton inelastic scattering. In this case, ϑ is equivalent to the polar angle of the γ-ray detectors. The exact angular distribution of the outgoing fragments was not measured because no position detector was placed immediately behind the target.

Two factors affected the determination of the detection polar angle: In first place, due to the arrangement of DALI2 some detectors were shielded from the target at some angles. Also, the Compton effect affected the average position where the γ-rays were detected. To take this into account, an effective first interaction position was obtained using the Monte Carlo simulation. These positions were used instead of the geometrical center of each crystal in the analysis to obtain a more accurate polar angle determination. A second factor affecting the determination of the polar angles was the

Isotope	β_{before}	β_{middle}	β_{end}	β_{ZD}	Offset
^{70}Ni	0.6447	0.6195	0.5885	0.5830	0.037
^{72}Ni	0.6324	0.6059	0.5704	0.5653	0.041
^{74}Ni	0.6256	0.5989	0.5644	0.5576	0.041
^{76}Zn	0.6359	0.6071	0.5705	0.5631	0.044
^{78}Zn	0.6300	0.6006	0.5632	0.5557	0.045
^{80}Zn	0.6263	0.5969	0.5593	0.5517	0.045

Table 4.4: Velocity of the isotopes at the entrance, middle and end of the target. The values were obtained using LISE++ to calculate the energy loss in the target. The velocity measured after the target, β_{ZD}, is also shown, as well as the difference between this velocity and the calculated velocity at the middle of the target.

presence of an offset of the target from its nominal position. This offset was taken into account when optimizing the Doppler correction, as will be described below.

The determination of the velocity was performed based on the measurements taken along the separators. As there was less matter in ZeroDegree than in BigRIPS, the velocity measurement after the target, β_{ZD}, was more accurate and was used to perform the Doppler correction. Due to energy loss in the materials between the target and the entrance of ZeroDegree, the velocity at the moment of interaction has a higher value than β_{ZD}. To compensate for this, it was necessary to apply an offset to the velocity. This offset was estimated using LISE++. Table 4.4 shows the the velocity of each isotope at the entrance, the middle and the end of the target obtained using LISE++. Also listed in the table is the β_{ZD} obtained experimentally and the difference between this velocity and the calculated velocity of the isotopes in the middle of the target.

In order to obtain an optimized and consistent Doppler correction, a 2-dimensional scan was performed, varying the offset in the velocity and the offset in the z position. This offset was defined as the difference between the measured center of the MINOS target and the one used for the Doppler correction, along the beam line. The velocity offset was varied in 50 steps in a range from -0.1 to 0.1. The z offset varied in 50 steps between -5 cm and 5 cm. This generated a set of 2500 histograms of Doppler corrected energy. Each one of these histograms was fitted with a sum of a Gaussian function and a second order polynomial to obtain the centroid, which corresponds to the transition energy, and standard deviation of the peak.

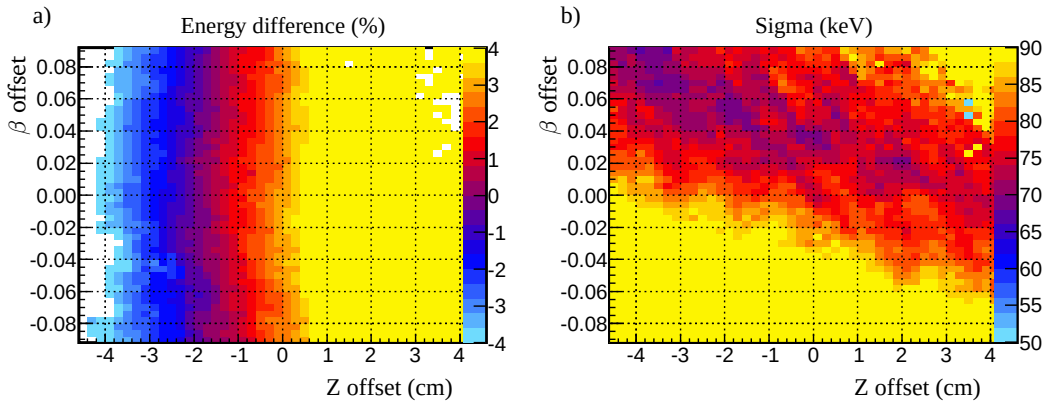

Figure 4.23: Doppler correction optimization ^{74}Ni. Different combinations of β offset and z offset were studies to obtain the best Doppler correction. Panel a) shows the difference between the Doppler corrected energy of the peaks and the known transition energy. Panel b) shows the width of the Doppler corrected peak.

Figure 4.23 shows the results obtained for ^{74}Ni. Panel a) shows a 2-dimensional histogram of the difference between the fitted centroid and the known transition energy (1024 keV for the $2_1^+ \rightarrow 0_{gs}^+$ transition in ^{74}Ni) for all the combinations of β offset and z offset. Panel b) shows the width (σ) of the fitted peak for all the offset combinations. From panel a), it can be seen that it was possible to obtain the proper Doppler corrected energy (around 0% difference) using any β offset, as long as the z offset stayed in a range between -2.5 cm to -1.0 cm. Nevertheless, it can be seen from panel b) that not all the combinations gave a reasonable value for σ: Negative values of the β offset did not seem to get good values for the resolution, as expected from the fact that the velocity at the moment of interaction was higher than β_{ZD}. Furthermore, it can be seen that for z offset between -2.5 cm and -1.0 cm, the β offset which gives a good resolution was around 0.04. This value is in agreement with the calculation performed used LISE++ as shown in Table 4.4. The selection of the z offset was performed by fixing the β offset to the calculated value and optimizing the resolution. This yielded an optimal z offset of -1.2 cm. It is to note that this value contains not only the real shift in the target position, but also any other unaccounted effect that may have influenced the Doppler correction. Due to the limited statistics for some of the isotopes, the 2-dimensional scan was not performed for all of them. Instead, a 1-dimensional scan over the β offset with a fixed z offset of -12 mm was performed. In all the cases, the

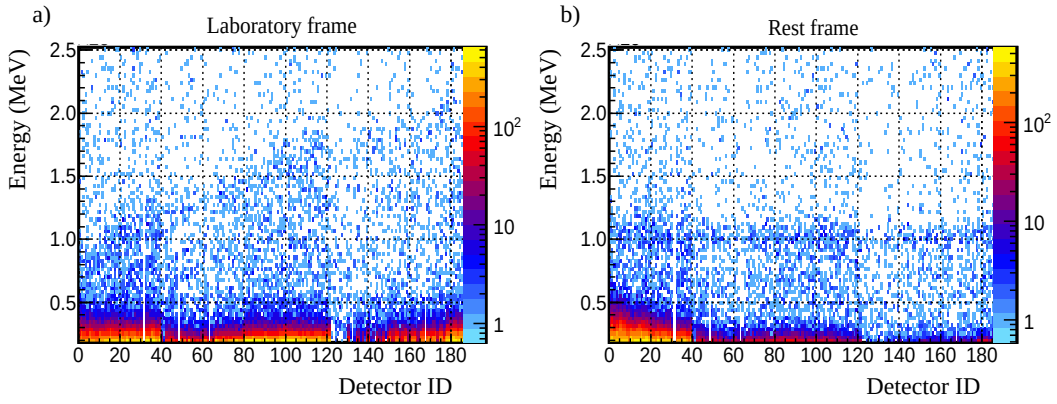

Figure 4.24: Example of the effect of the Doppler correction procedure for ^{74}Ni. Panel a) shows the detected energy as a function of the detector ID in the laboratory frame of reference. The dependence of the measured energy with the detection angle can be seen. Panel b) shows the energy in the rest frame after performing the Doppler correction.

results were consistent with the LISE++ calculations.

In order to check the Doppler correction procedure, the dependence of the Doppler corrected energy with the detection angle was investigated. Figure 4.24 shows the Doppler corrected energy as a function of the crystal number for ^{74}Ni. As the detectors are arranged in different layers, their ID number is analogous to the polar angle of detection. Panel a) shows the spectra before Doppler correction was applied (laboratory frame), while Panel b) shows the effect of performing the Doppler correction. In this case, the add-back procedure up to 15 cm was applied. It can be seen that after performing the Doppler correction, the dependence of the energy with the angle is removed and the $2_1^+ \rightarrow 0_{gs}^+$ transition can be clearly observed. A small contribution of the $4_1^+ \rightarrow 2_1^+$ transition (at 739 keV for ^{74}Ni) could also be observed for most of the isotopes. It can also be seen that the atomic background detected at low energies affects more severely the backward-angle detectors.

4.8 `Geant4` simulation

The `Geant4` simulations of DALI2 were used to obtain the response of the array to the radiation emitted by the projectiles. In the first step, the `EventGenerator`, a total of one million incoming particles was simulated. To make the simulation as realistic as possible, a cylindrical liquid hydrogen target with the dimensions of the MINOS

target was used. The density of the target was chosen to be $\rho = 70.973$ Kg/cm^3, in agreement with the measured values. The energies of the incoming particles were chosen to be equal to the energy before the target, calculated with LISE++ and listed in Table 4.2. Other parameters of the beams, such as the width of the energy distribution, and the position in the (x, y) plane, were taken from the measured characteristics of the isotopes.

A consistency check was performed by comparing the velocity at the moment of interaction, β_{real}, with the velocity at the middle of the target, β_{middle}, calculated with LISE++. Table 4.5 shows the result of this comparison. The simulated β_{real} is reported as well as the percentage difference of this value with β_{middle}. A comparison between the simulated velocity after the target, β_{end}, and the corresponding value obtained with LISE++ was also performed as reported in the last two columns of the Table. It can be seen that the velocities obtained with the simulation are in agreement with the values calculated with LISE++ within 1%. The higher difference in β_{end} for ^{70}Ni may be due to the position of this isotope at the very edge of the acceptance of the spectrometer. No atomic background was considered in this step of the simulation.

In the second step, the `EventBuilder`, the output file of the previous step was taken as input and the interaction of the emitted γ-rays with DALI2 was simulated. The individual crystal resolution was included as an input to get a more realistic response. Also in this step, the offset from the target to the nominal center of DALI2 was taken into account. A z_{vertex} resolution of 5 mm (FWHM) was included. This represents the reconstruction capabilities of MINOS, nevertheless for the present analysis it was not

Isotope	β_{real}	**Diff. (%)**	β_{end}	**Diff. (%)**
^{70}Ni	0.6184	0.2	0.5957	1.2
^{72}Ni	0.6042	0.3	0.5721	0.3
^{74}Ni	0.5972	0.2	0.5642	0.0
^{76}Zn	0.6059	0.2	0.5721	0.3
^{78}Zn	0.596	0.8	0.5638	0.1
^{80}Zn	0.5957	0.2	0.5600	0.1

Table 4.5: Simulated velocity of the isotopes at the moment of interaction and at the end of the target. The difference between β_{real} and the β_{middle} is reported as well as the difference in β_{end} between the simulation and the LISE++ calculation.

used. An additional 1% resolution in the simulated β was also included.

In the third step, the `Reconstructor`, the analysis of the simulated data was performed. The Doppler correction was done in an equivalent way as it was done for the experimental data using β_{real}. This choice was justified by the small difference between this value and β_{middle}, which was used to perform the experimental Doppler correction. Although a small effect due to the difference in the width of the distributions is still present it was negligible in the final results. The add-back procedure was taken into account and the first interaction position of the γ-rays was also obtained and used in the analysis.

In order to take into account feeding from the $4_1^+ \rightarrow 2_1^+$ transition, two situations were simulated for each isotope. In the first case, only the excitation to the 2_1^+ state was simulated, while in the second case an excitation to the 4_1^+ state was considered with the subsequent $4_1^+ \rightarrow 2_1^+$ and $2_1^+ \rightarrow 0_{\text{gs}}^+$ decays. If a higher state is populated by the reaction, the corresponding cascade was also simulated to remove the feeding.

Figure 4.25 shows examples of the simulated response of DALI2. Panel a) shows the simulation of the $2_1^+ \rightarrow 0_{\text{gs}}^+$ transition at 1260 keV in ^{70}Ni. The effect of the add-back procedure in this case can clearly be seen. Panel b) shows the simulation of the 2_1^+ as well as the 4_1^+ excitations in ^{80}Zn. If only the 2_1^+ is populated, the transition at 1492 keV can be clearly seen. If the 4_1^+ is populated, the $4_1^+ \rightarrow 2_1^+$ transition as well

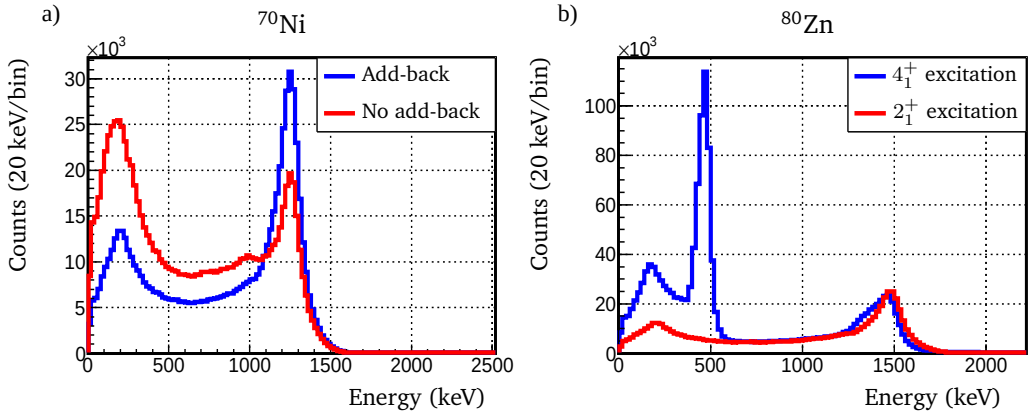

Figure 4.25: Examples of the simulated response of DALI2. Panel a) shows the effect of the add-back procedure for the $2_1^+ \rightarrow 0_{\text{gs}}^+$ transition in ^{70}Ni. Panel b) shows the simulation of 2_1^+ and 4_1^+ excitations in ^{80}Zn. In this case, the effect if the long lifetime of the 4_1^+ state in the line shape of the $2_1^+ \rightarrow 0_{\text{gs}}^+$ transition can be observed.

as the $2_1^+ \rightarrow 0_{gs}^+$ transition at 482 keV can be seen. Due to the considereation of the recently reported lifetime of about 136^{+92}_{-67} ps of the 4_1^+ state (99), a modification in the line shape of the $2_1^+ \rightarrow 0_{gs}^+$ is observed due to feeding from the 4_1^+ state. This was the only case where a lifetime effect was observed. For the rest of the isotopes, where no lifetime of the excited states is known, a negligible lifetime was assumed. As the measured line shapes did not show any additional broadening, this assumption was justified.

CHAPTER 5

RESULTS AND DISCUSSION

This Chapter shows the results obtained after performing the data analysis described in the previous Chapter. In Section 5.1, a summary of the procedure used to obtain the cross sections and the errors is presented, followed by a detailed description of the extraction of the proton inelastic cross section for each isotope. Section 5.2 presents the analysis of the error in the cross section due to the add-back procedure and a possible angular distribution of the decay radiation. In Section 5.3, the summary of the cross sections of proton inelastic scattering is shown, including all the errors considered. Finally, Section 5.4 describes the calculation of the deformation length and the neutron-to-proton matrix elements for each isotope. A discussion on the implications of the results in the structure of the isotopes of interest is also included in this section.

5.1 Cross section determination

After performing the Doppler correction procedure described in the previous chapter, γ-ray spectra were obtained for all the isotopes of interest. In all the cases, the $2_1^+ \rightarrow 0_{\rm gs}^+$ and the $4_1^+ \rightarrow 2_1^+$ transitions were observed at energies consistent with previously reported measurements. Other transitions were also observed, as will be reported below. The exclusive proton inelastic scattering cross section for the excitation of a particular state, X, was calculated as

$$\sigma^X_{(p,p')} = \frac{PA}{DN_A}, \tag{5.1}$$

where P is the interaction probability, A is the mass number of the atoms in the target, $D = 723.894$ mg/cm^2 is the thickness of the target, and $N_A = 6.022 \times 10^{23}$ mol^{-1} is the Avogadro number. This work is focused on the states $X = 2_1^+$ and $X = 4_1^+$. The reaction probability was obtained as

$$P = \frac{\text{Number of particles populating the state of interest}}{\text{Number of particles reaching the target}}. \tag{5.2}$$

The number of particles reaching the target and surviving detection through ZeroDegree was obtained from the total number of F7DS triggers, as shown in Table 4.3. The number of particles populating each excited state was obtained by comparing the simulated and the experimental γ-ray spectra.

The transitions observed in the experimental spectrum were simulated, as previously described, to obtain the response of DALI2. Apart from the known $2_1^+ \rightarrow 0_{\text{gs}}^+$ and $4_1^+ \rightarrow 2_1^+$ transitions, some not-reported decays were simulated to obtain a better description of the experimental spectrum. These simulations were fitted to the spectra together with two exponential functions. The exponential functions were included to model the atomic background at low energy and the nuclear background at high energy.

In principle, the simulation provides a line shape at a particular energy. Thus, only a scaling factor needs to be fitted for each peak. In order to take into account possible errors on the energy calibration or in the Doppler correction, the shape of the peaks remained unchanged, while their position (energy) and amplitude (scaling factor) were fitted. For the position of known peaks, only 10 keV difference with the simulated energy was allowed. For the peaks at unknown energies, a range of ± 50 keV was permitted to keep a compromise between obtaining a good fit while keeping a valid simulated shape. The parameters of the exponential functions were fitted in each case. As the simulation assumed N number of particles interacting in the target, the total number of particles populating the state of interest was calculated as NA_{fit}, where A_{fit} is the fitted amplitude of the corresponding peak.

The error in the cross section was calculated taking into account the error in the target thickness and the error in the reaction probability as

$$\left(\frac{\Delta\sigma_{(p,p')}}{\sigma_{(p,p')}}\right)^2 = \left(\frac{\Delta D}{D}\right)^2 + \left(\frac{\Delta P}{P}\right)^2, \tag{5.3}$$

where the superscript X has been removed for simplicity. For $\Delta D/D$, a value of 2% was estimated based on the possible deformation of the windows of the liquid hydrogen target. For $\Delta P/P$, following its definition in Equation 5.2, two contributions were taken into account: First, the error in the total number of ions reaching the target, which was taken as the square root of the value. Second, the error in the total number of particles populating each state, which was taken from the error given by the fit and an additional 6% error due to the simulation of the efficiency of DALI2. An additional contribution to the error due to possible unaccounted feeding was also considered for each isotope independently.

5.1.1 ^{70}Ni

Figure 5.1 shows a partial level scheme of ^{70}Ni. All the states and γ-ray energies are taken from the adopted values given by the National Nuclear Data Center (NNDC) (46).

As can be seen from the level scheme, this isotope has an 8^+ seniority isomer. During the production of this isotope, both the ground state and the isomeric state were populated. Due to this fact, some of the incoming ions reached the target in the isomeric state, thus they should not contribute to the calculation of the cross section. As the isomeric ratio was not known, the number of ions used for the normalization is over-estimated and the values reported in this section represent lower limits for the

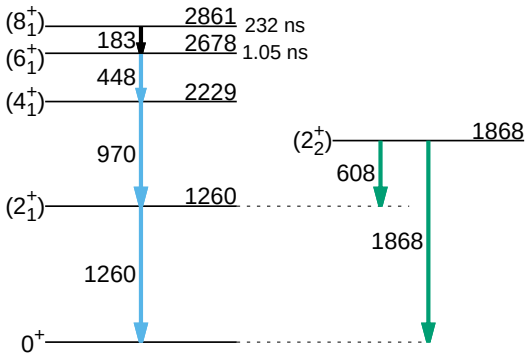

Figure 5.1: Partial level scheme of ^{70}Ni. The yrast band up to the 8_1^+ isomer is shown. Additionally, the decay of the 2_2^+ state is presented. The blue and green lines correspond to the decays simulated and used for the fit.

cross section. A more accurate value requires the analysis of the data taken by the EURICA array and is out of the scope of this thesis.

Four previously reported transitions were clearly visible in the Doppler corrected spectrum of ^{70}Ni: From the yrast band, the $2_1^+ \rightarrow 0_{gs}^+$ transition at 1260 keV and the $4_1^+ \rightarrow 2_1^+$ transition at 970 keV. Additionally, the decay of a reported potential 2_2^+ state was observed with the $2_2^+ \rightarrow 0_{gs}^+$ transition at 1868 keV and the $2_2^+ \rightarrow 2_1^+$ transition at 608 keV. These four transitions were taken into account to fit the experimental data.

Figure 5.2 shows the Doppler corrected spectra of ^{70}Ni together with the fit performed. An add-back procedure up to 15 cm was performed for both the simulation and the experimental data. The black points with error bars represent the experimental data. The blue dashed lines show the simulated response functions for the $2_1^+ \rightarrow 0_{gs}^+$ and the $4_1^+ \rightarrow 2_1^+ \rightarrow 0_{gs}^+$ cascade. The green dashed lines represents the decay of the 2_2^+ state. The same color coding for the decays is depicted in the level scheme shown in Figure 5.1. It is to note that to simulate the decay of the 2_2^+ state, the branching ratio reported in Ref. (100) was considered. The orange dashed line represents an additional decay around 2800 keV simulated to better describe the experimental spectrum at high

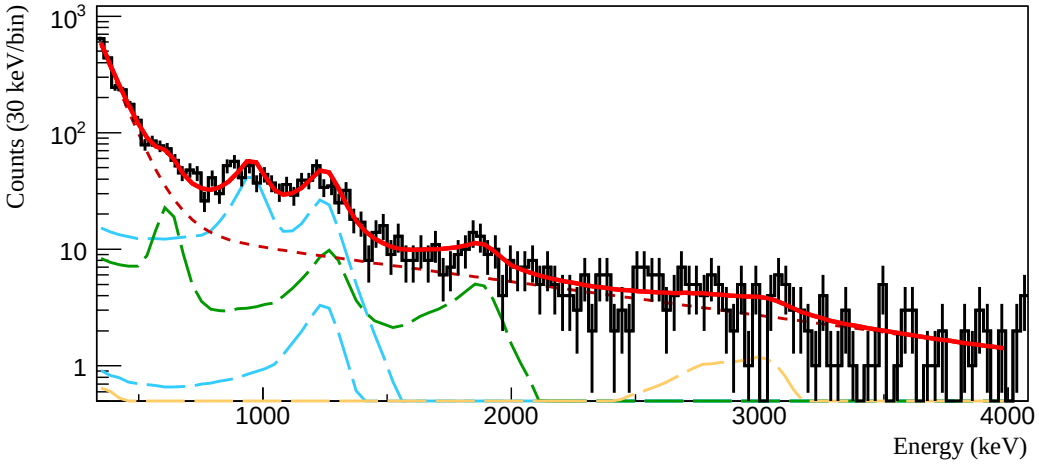

Figure 5.2: Doppler corrected spectrum of ^{70}Ni and fit performed. The experimental spectrum obtained is shown by the black points. The dashed blue, green and yellow lines show the simulated detector responses. The red dashed line shows the fitted background and the red solid line corresponds to the total fit. An add-back up to 15 cm was performed for both the data and the simulation.

energies. The red dashed line corresponds to the double exponential background and the red solid line shows the total fit. The lower limit of the cross sections for populating the 2_1^+, 4_1^+ and 2_2^+ states were obtained to be 0.4(6) mb, 2.9(5) mb 1.8(5) mb respectively. It is to note that the amplitudes of the $2_1^+ \rightarrow 0_{gs}^+$ and $4_1^+ \rightarrow 2_1^+$ transitions are very similar in the experimental spectra, which is already an indication of the low $\sigma_{(p,p')}^{2_1^+}$.

In order to check the consistency of the fits, each γ-ray corresponding to the decay of the 2_2^+ state was simulated independently. After subtraction of the feeding, this yielded cross sections for all the states in agreement with the values obtained by simulating the full cascade. The branching ratio for the 2_2^+ state was also obtained from this fit. Values of 42(29)% for the $2_2^+ \rightarrow 0_{gs}^+$ and 58(25)% for the $2_2^+ \rightarrow 2_1^+$ decays, in agreement within error bars with the previously reported values (47.7% and 52.3% respectively), were obtained.

5.1.2 ^{72}Ni

Figure 5.3 shows a partial level scheme for ^{72}Ni. The energy levels and decay energies from the yrast band are taken from the adopted values of NNDC.

In addition, two candidates for 2^+ states, recently reported in Ref. (101), are also

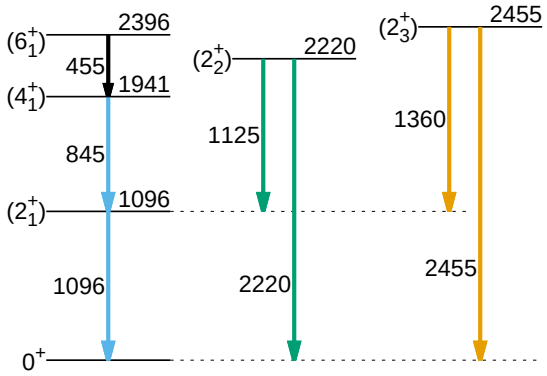

Figure 5.3: Partial level scheme of ^{72}Ni. The yrast band up to the 6_1^+ state is shown. Additionally, the decays of recently reported candidates for the 2_2^+ and the 2_3^+ states are presented. The blue, green and orange lines correspond to the decays simulated and used for the fit.

depicted. Although other candidates for low-lying 2^+ states were reported, they were not observed and therefore were not taken into account . As for ^{70}Ni, the level scheme is color coded with the transitions that were used for the fit.

The $2_1^+ \rightarrow 0_{gs}^+$ transition at 1096 keV as well as the $4_1^+ \rightarrow 2_1^+$ transition at 845 keV were observed in the Doppler corrected spectrum of ^{72}Ni. At higher energies, the presence of additional peaks on top of the background was evident from the shape of the spectrum. A systematic study on the best fit of the high-energy region resulted in the conclusion that the highest contribution to the background comes from a possible transition at around 2200 keV. This result can be seen as an indication of the $2_2^+ \rightarrow 0_{gs}^+$ transition, which is reported to lay at 2220 keV. The resolution of DALI2 did not allow to resolve the possible $2_2^+ \rightarrow 2_1^+$ transition at 1125 keV from the $2_1^+ \rightarrow 0_{gs}^+$ transition. Nevertheless, the population of this state is a reasonable assumption given the reaction mechanism and the equivalent observation on ^{70}Ni. A cross-check of this assumption based on a γ-γ coincidence matrix will be presented below.

Figure 5.4 shows the experimental spectrum of ^{72}Ni together with the fit performed. Add-back up to 15 cm was applied to the data as well as to the simulation. The black

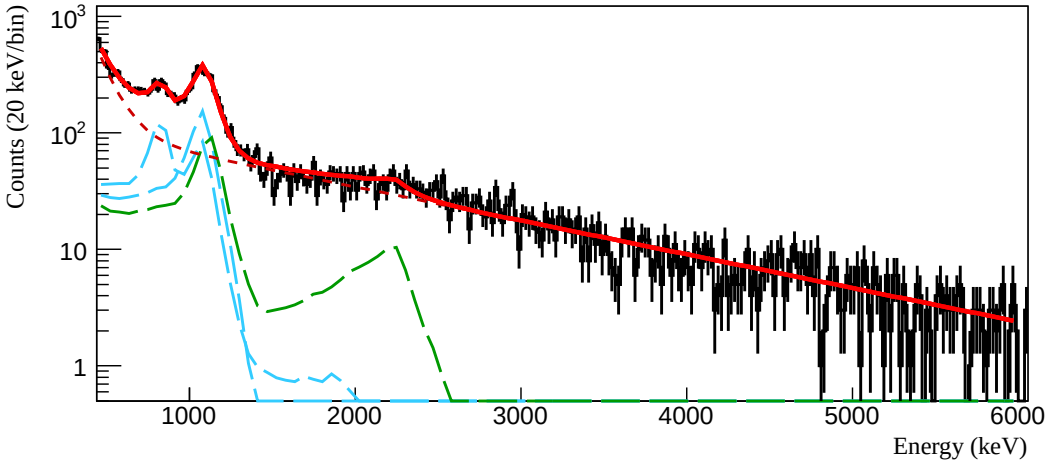

Figure 5.4: Doppler corrected spectrum of ^{72}Ni and fit performed. The experimental spectrum is shown by the black points. The dashed blue, green and yellow lines show the simulated detector responses. The red dashed line shows the fitted background and the red solid line corresponds to the total fit. An add-back up to 15 cm was performed for both the data and the simulation.

points with error bars represent the experimental data. The blue dashed lines show the simulated response functions for the $2_1^+ \rightarrow 0_{gs}^+$ and the $4_1^+ \rightarrow 2_1^+ \rightarrow 0_{gs}^+$ cascade. The green dashed lines represents the decay of the 2_2^+ state. This simulation was performed using the branching ratio reported in Ref. (101) and due to the overlapping energies, the simulation of each peak independently was not feasible. The dashed red line show the background and the solid red line corresponds to the total fit. The cross sections for populating the 2_1^+, 4_1^+ and 2_2^+ states were measured to be 2.6(4) mb, 1.5(2) mb and 1.4(3) mb, respectively. From the experimental spectrum, it can be clearly seen that the ratio between the amplitudes of the $2_1^+ \rightarrow 0_{gs}^+$ and $E(4_1^+)$ transitions is different than for ^{70}Ni and indicate a reduction on the $\sigma_{(p,p')}^{4_1^+}$.

Although no clear evidence of the population of the 2_3^+ state was observed, its decay was included in the fit to take into account additional feeding. Figure 5.5 shows the result obtained. Although the goodness of the fit is improved, the values obtained for the cross section are in agreement with the reported values within error bars. The inclusion of more transitions to further improve the description of the high energy background did not changes the cross sections. This guarantees that any possible feeding is included in the error bars. It is noted that if only the population of the 2_1^+ and 4_1^+ states

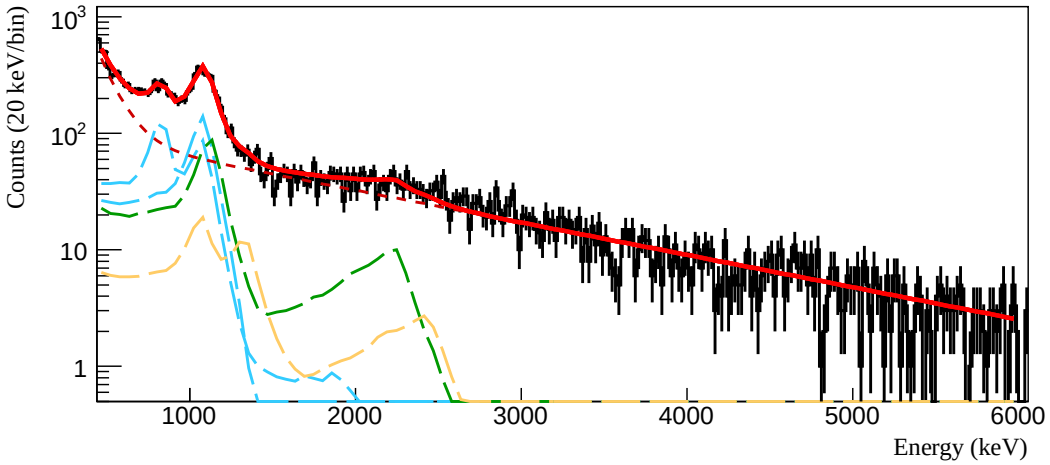

Figure 5.5: Doppler corrected spectrum of ^{72}Ni with additional lines fitted. The lines in the Figure have the same meaning as in the previous fit. The additional orange dashed line represents the decay of the 2_3^+ state.

is considered, an upper limit of $\sigma^{2_1^+}_{(p,p')}$ =4.0(4) mb is obtained. The difference between this limit and the reported cross section clearly indicates the importance of the feeding transitions for this analysis.

In order to confirm the feeding of the 2_1^+ state, a γ-γ coincidence matrix was obtained. Due to very irregular background, which prevented the recognition of an energy region where no transitions were expected, a background gate resulted unfeasible.

Gates in the low- and high-energy side of the $2_1^+ \rightarrow 0_{gs}^+$ transition were performed and the results compared as shown in Figure 5.6. The inset shows the total projection of the γ-γ matrix together with the gates applied. The resulting spectra are shown by the black and red histograms. It can be seen from the Figure that when gating on the low-energy side of the peak (black gate), which should mainly correspond to the $2_1^+ \rightarrow 0_{gs}^+$ transition, the $4_1^+ \rightarrow 2_1^+$ transitions is clearly visible. In addition, a structure around 1100 keV can be seen. On the other hand, when gating on the high-energy side of the peak (red gate), the intensity of the $4_1^+ \rightarrow 2_1^+$ transition decreases and a structure can be observed at around 1000 keV. These observations are in agreement with the presence of a feeding transition at an energy slightly higher than the $2_1^+ \rightarrow 0_{gs}^+$

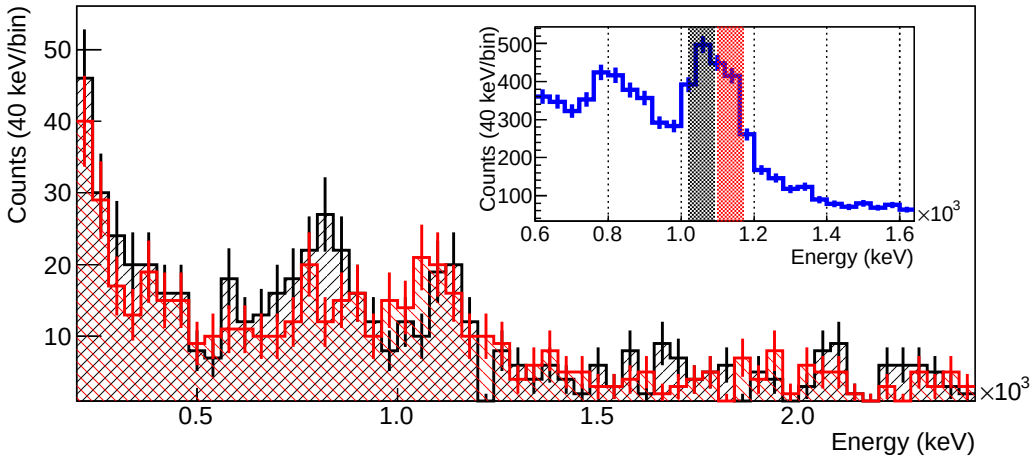

Figure 5.6: Spectrum of γ-rays measured in coincidence with the 2_1^+ state in ^{72}Ni. The inset shows the total projection of the γ-γ matrix as well as the gates used. The black histogram shows the spectrum gated in the low-energy side of the peak and the red histogram shows the spectrum when gated in the high-energy side. An evidence of the 2_2^+ state can be observed. No background subtraction was performed.

transition. Due to the limited statistics, any statement about the feeding from higher lying states was unreasonable.

The relative intensity of the feeding from the 4_1^+ state compared to the feeding from the possible 2_2^+ state was obtained using the black spectrum in Figure 5.6 by fitting an exponential and a Gaussian function to the peaks. The widths of the Gaussian functions were fixed according to the simulated responses. It was found that the feeding from these two states has a comparable intensity, with the feeding from the 4_1^+ state about 1.3 times higher. Taking into account the large error bars, this result is in agreement with the cross sections obtained.

As a cross check, the spectrum in coincidence with the $4_1^+ \rightarrow 2_1^+$ transition was obtained, as shown in Figure 5.7. In this case, the $2_1^+ \rightarrow 0_{gs}^+$ transition can be clearly observed. Although some hints of peaks can be seen at between 500 keV and 1000 keV, statistics are not enough to make a conclusive statement. No other structure was statistically significant, pointing to the absence of higher-lying transitions feeding the 4_1^+ state.

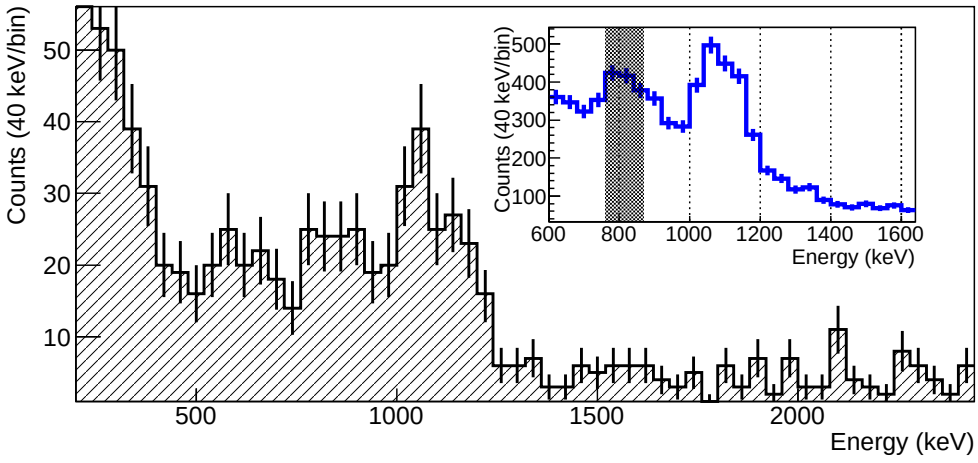

Figure 5.7: Spectrum of γ-rays measured in coincidence with the 4_1^+ state in ^{72}Ni. The inset shows the total projection of the γ-γ matrix and the gate applied. No background subtraction was performed.

5.1.3 ^{74}Ni

The known level scheme of ^{74}Ni is presented in Figure 5.8. Only the 2_1^+ and 4_1^+ states have been reported. The energy levels as well as the transition energies are taken from NNDC. The energies of the 2_1^+ and 4_1^+ states are very similar to the ones of ^{72}Ni, suggesting a similar structure.

The $2_1^+ \rightarrow 0_{gs}^+$ transition at 1024 keV was clearly visible in the Doppler corrected spectrum of ^{74}Ni. A small peak at an energy consistent with the reported $4_1^+ \rightarrow 2_1^+$ transition at 739 keV was also observed. No other significant peaks were present. Nevertheless, in a similar fashion as ^{72}Ni, the shape of the high-energy part of the spectrum suggested the presence of additional peaks. The systematic search for the best fit suggested the presence of two structures in this energy region: One at around 2250 keV and one around 3100 keV. Although no transitions are reported at these energies, the two simulations were taken into account to fit the spectrum.

Figure 5.9 shows the experimental spectrum obtained for this isotope together with the fit performed. An add-back up to 15 cm was performed both in the simulation and in the experimental data. The black points with error bars represent the experimental data. The blue dashed lines shows the simulated response functions for the $2_1^+ \rightarrow 0_{gs}^+$ and the $4_1^+ \rightarrow 2_1^+ \rightarrow 0_{gs}^+$ cascade. The green and orange dashed lines represent the simulated response of a decay of 2150 keV and 3100 keV respectively. The dashed red line show the background and the solid red line corresponds to the total fit.

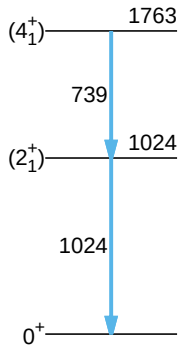

Figure 5.8: Partial level scheme of ^{74}Ni. The only two states reported are the 2_1^+ and the 4_1^+ states. The population of these two states was considered in the fit.

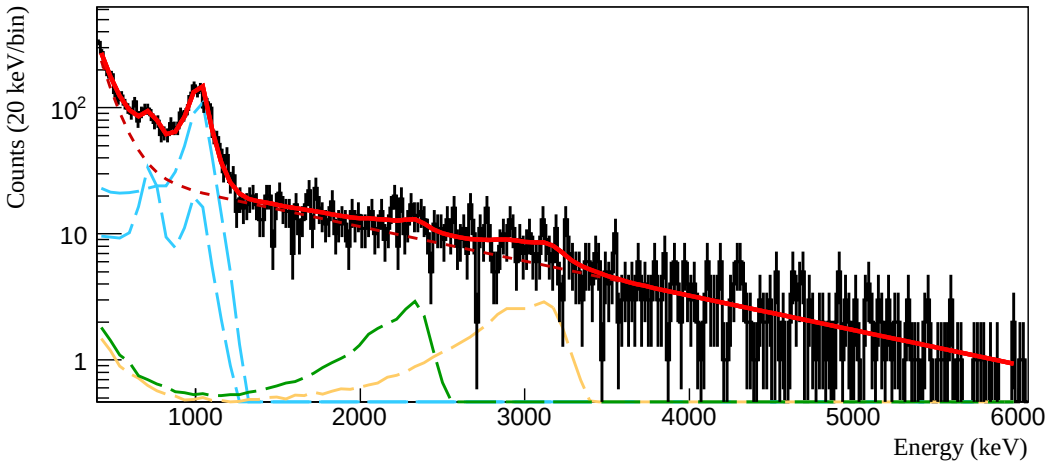

Figure 5.9: Doppler corrected spectrum of ^{74}Ni and fit performed. The experimental spectrum is shown by the black points. The dashed blue, green and yellow lines show the simulated detector responses. The red dashed line shows the fitted background and the red solid line corresponds to the total fit. An add-back up to 15 cm was applied for both the data and the simulation.

The cross section obtained for the population of the 2_1^+ state was 4.3(5) mb and for populating the 4_1^+ state was 0.8(2) mb. The total cross section for populating the higher-lying states was measured to be 0.7(4) mb. If any of these states feeds to the 2_1^+ state, the corresponding cross section will be reduced. Following the case of ^{72}Ni and the expected similarity in their structure, it was considered that the peak at around 2150 keV corresponds to the $2_2^+ \rightarrow 0_{gs}^+$ transition. In this case, a $2_2^+ \rightarrow 2_1^+$ transition is to be expected around 1120 keV. In the same way as for ^{72}Ni, this transition would be unresolvable with DALI2. In order to study the effect of this feeding in the cross section, this proposed cascade was simulated and used in the fit. The branching ratio for the decay of the 2_2^+ state was assumed to be the same as for ^{72}Ni.

Figure 5.10 shows the fit obtained when including the proposed 2_2^+ decay. It can be seen that the fit results in a not negligible contribution to the 2_1^+ state. The cross sections for populating the 2_1^+ state using this fit was 3.6(5) mb. Although in agreement within error bars, this value is lower than the one reported without the feeding. Due to the presence of high-energy background, this lower value is considered to take into account any unobserved feeding and was used for the subsequent calculations.

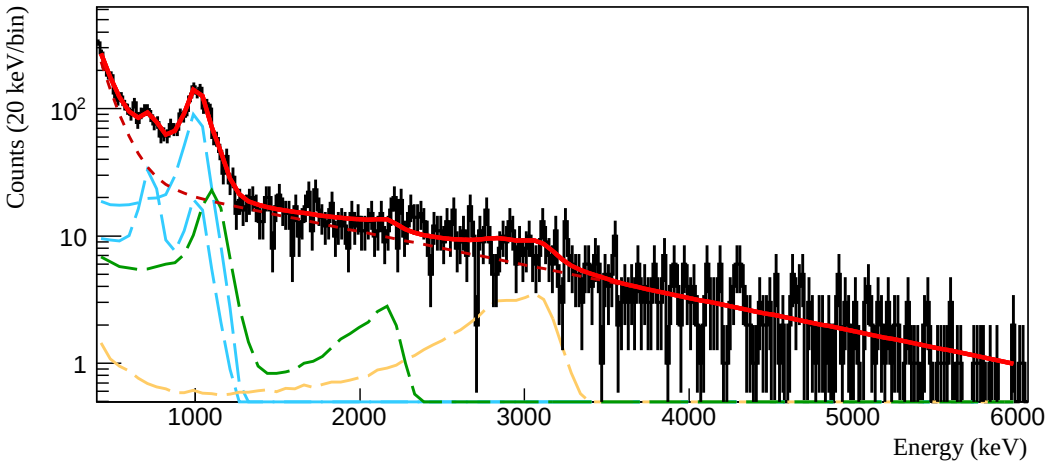

Figure 5.10: Doppler corrected spectrum of ^{74}Ni with additional lines fitted. The lines in the Figure have the same meaning as in the previous fit. The green line shows now the possible decay of a 2_2^+ state.

The cross section for populating the 4_1^+ state was not modified when using this fit, and a value of 0.8(2) mb was obtained for the cross section of the possible 2_2^+ state. No other states were considering to contribute to the feeding.

In order to shed light on the presence of the proposed 2_2^+ state, a coincidence matrix was constructed. As for ^{72}Ni, no background gate was implemented. The same strategy of gating on the low- and high-energy sides of the peak corresponding to the $2_1^+ \rightarrow 0_{gs}^+$ transition was applied. Figure 5.11 shows the obtained coincidence spectrum. The inset shows the total projection of the γ-γ matrix together with the gates applied. The resulting spectra are shown by the black and red histograms. The spectrum in coincidence with the low-energy side of the peak (black gate) shows a structure at the $4_1^+ \rightarrow 2_1^+$ transitions. In addition, a structure around 1100 keV can also be seen. The spectrum in coincidence with the high-energy side of the peak (red gate) shows no structure resembling the $4_1^+ \rightarrow 2_1^+$ transition, but a structure can be observed at around 1000 keV. Although this is an indication of the presence of the 2_2^+ state, the limited resolution of DALI2 and the reduced statistics prevent drawing strong conclusion about it.

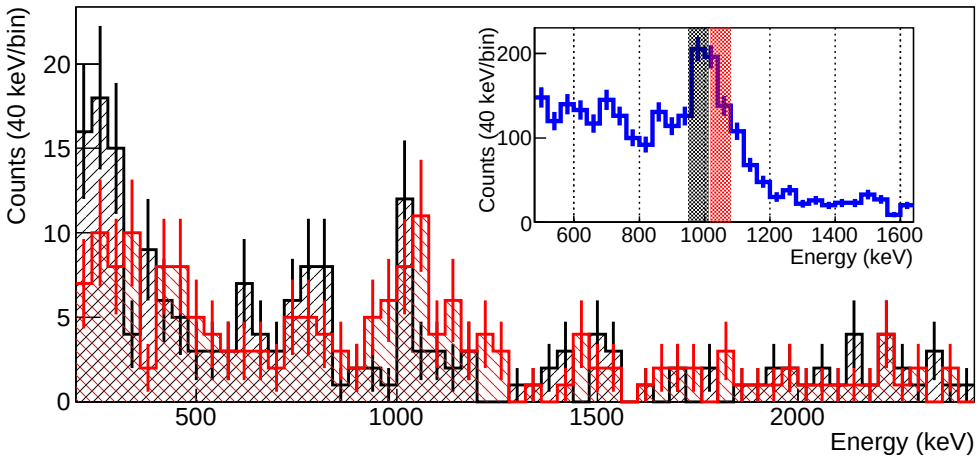

Figure 5.11: Spectrum of γ-rays measured in coincidence with the 2_1^+ state in ^{74}Ni. The inset shows the total projection of the γ-γ matrix and as the gates used. The black histogram shows the spectrum gated in the low-energy side of the peak. The red histogram shows the spectrum when gated in the high-energy side. No background subtraction was performed.

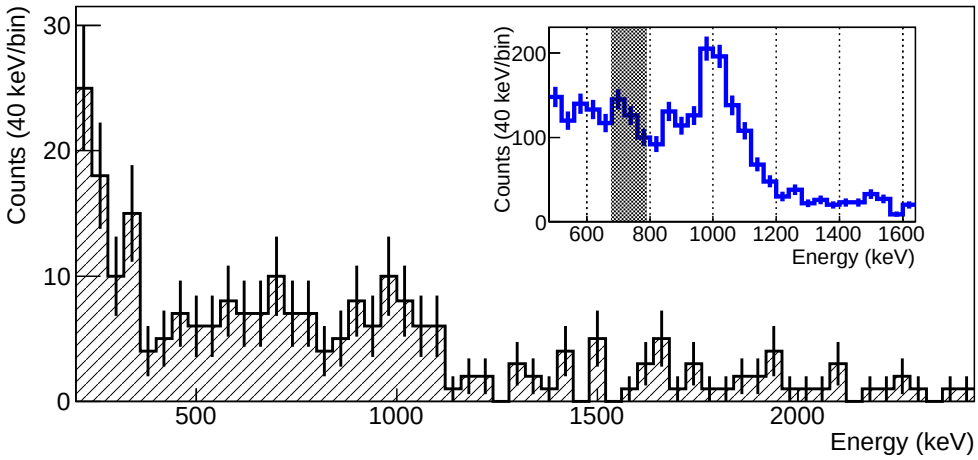

Figure 5.12: Spectrum of γ-rays measured in coincidence with the 4_1^+ state in ^{74}Ni. The inset shows the total projection of the γ-γ matrix and the gate applied. The black histogram shows the spectrum gated in the $4_1^+ \rightarrow 2_1^+$ transition energy. No background subtraction was performed.

The spectrum in coincidence with the $4_1^+ \rightarrow 2_1^+$ transition was also obtained and the result is shown in Figure 5.12. A small structure corresponding to the $2_1^+ \rightarrow 0_{gs}^+$ transition can be observed. Apart form what seems to be a self-coincidence, no other structure was observed, pointing to the absence of higher-lying states feeding the 4_1^+ state and to the small cross section to populate the 4_1^+ state.

5.1.4 ^{76}Zn

A partial level scheme for ^{76}Zn is presented in Figure 5.13. From the yrast band only the 2_1^+ and the 4_1^+ states are shown. A reported candidate for 0_2^+ is also shown. Higher-lying states of this isotope have been reported, but are not shown in the figure. The energy levels and decay energies are taken from the adopted values of NNDC.

In spite of the reduced statistics, it was possible to observe the $2_1^+ \rightarrow 0_{gs}^+$ transition at 599 keV, as well as the $4_1^+ \rightarrow 2_1^+$ transition at 698 keV on ^{76}Zn. Although the resolution of DALI2 did not allow for a proper separation of the two lines, the structure observed around 600 keV has clearly an asymmetric shape. No other peak was apparent in the spectrum.

Figure 5.14 shows the experimental spectrum obtained together with the fit. An add-back distance up to 15 cm was applied to the data as well as to the simulation. The black points with error bars represent the experimental data. The blue dashed lines show the simulated response functions for the $2_1^+ \rightarrow 0_{gs}^+$ and the $4_1^+ \rightarrow 2_1^+ \rightarrow 0_{gs}^+$ cascade. The dashed red line show the background and the solid red line corresponds

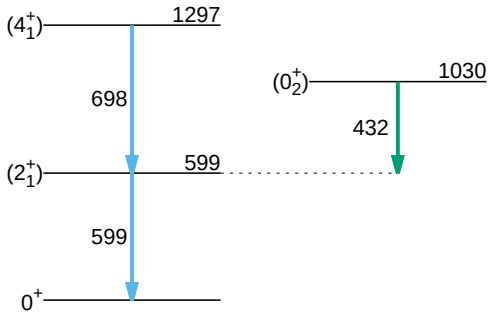

Figure 5.13: Partial level scheme of ^{76}Zn. From the yrast band only the 2_1^+ and the 4_1^+ states are represented. Additionally, a reported 0_2^+ state is shown.

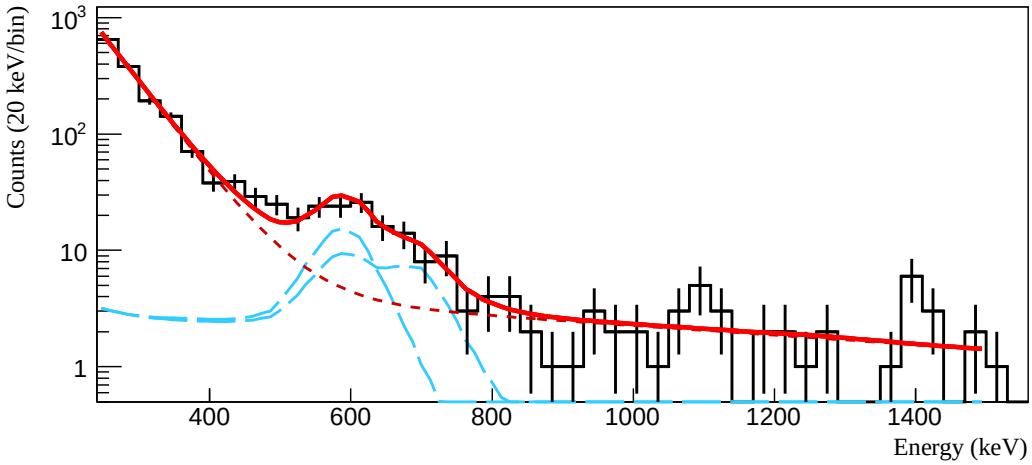

Figure 5.14: Doppler corrected spectrum of ^{76}Zn and fit performed. The experimental spectrum is shown by the black points. The dashed blue lines show the simulated detector responses. The red dashed line shows the fitted background and the red solid line corresponds to the total fit. Add-back up to 15 cm was performed for both the data and the simulation

to the total fit. The cross section of populating the 2_1^+ state was obtained as 2.7(12) mb and the cross section for populating the 4_1^+ state was measured as 1.8(7) mb. The reduced statistics are clearly reflected in the big error bars of almost 50%. Feeding from higher-lying states was considered and included in the large error bars. The reduced statistics prevented the construction of a γ-γ matrix.

5.1.5 ^{78}Zn

Figure 5.15 shows a partial level scheme of ^{78}Zn up to the reported 8_1^+ isomeric state. All the states and γ-ray energies are taken from NNDC. Just as for ^{70}Ni, due to the presence of the isomer, the calculation of the cross section is not possible and allowed to report only lower limits for its value.

The $2_1^+ \rightarrow 0_{gs}^+$ transition at 730 keV, as well as the $4_1^+ \rightarrow 2_1^+$ transition at 891 keV were observed in the Doppler corrected spectrum of ^{78}Zn. The shape of the spectrum at higher energies suggests the presence of other states above 2000 keV. No sign of any additional transition was observed between 1000-2000 keV. A systematic search for the best fit at high energies suggested the presence of two peaks, one at around 2600 keV

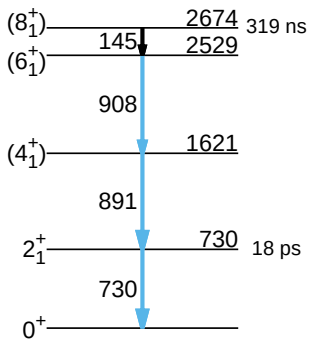

Figure 5.15: Partial level scheme of ^{78}Zn. The yrast band up to the 8_1^+ isomer is shown. The blue lines correspond to the decays simulated and used for the fit.

and one at around 3400 keV. In spite of the fact that such states have not been reported, the simulated response functions were included in the fit to obtain a better agreement with the data.

Figure 5.16 shows the Doppler corrected spectrum of ^{78}Zn and the fit performed.

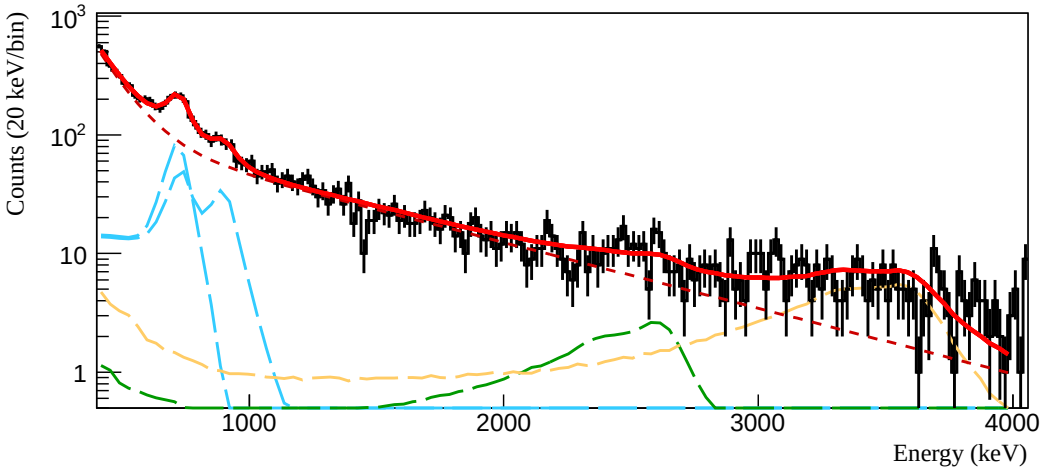

Figure 5.16: Doppler corrected spectrum of ^{78}Zn and fit performed. The experimental spectrum is shown by the black points. The dashed blue, green and yellow lines show the simulated detector responses. The red dashed line shows the fitted background and the red solid line corresponds to the total fit. Add-back up to 15 cm was performed for both the data and the simulation.

Add-back up to 15 cm was applied to both the experimental and the simulated data. The black points with error bars represent the experimental data. The blue dashed lines shows the simulated response functions for the $2_1^+ \rightarrow 0_{gs}^+$ decay and the $4_1^+ \rightarrow 2_1^+ \rightarrow 0_{gs}^+$ cascade. The green and orange dashed lines represent the simulated responses of transitions at 2600 keV and 3400 keV respectively. The dashed red line shows the fitted background and the solid red line corresponds to the total fit.

The cross section for populating the 2_1^+ state was obtained to be 3.4(7) mb, the corresponding value for the 4_1^+ state was 1.9(4) mb and the total cross section for populating the higher-lying states was obtained to be 2.0(8) mb. As in the case of ^{74}Ni, it is necessary to take into account the possible feeding of these high-energy transitions to the 2_1^+ state. The decrease in the cross section due to the feeding of the transition at 2600 keV is negligible within error bars. Nevertheless the peak at 3400 keV would represent a considerable contribution.

In order to investigate the coincidence of this transition with the 2_1^+ state, a γ-γ matrix was generated. Figure 5.17 shows the obtained spectrum. The inset shows the total projection of the γ-γ matrix and the two gates applied. The black gate corresponds

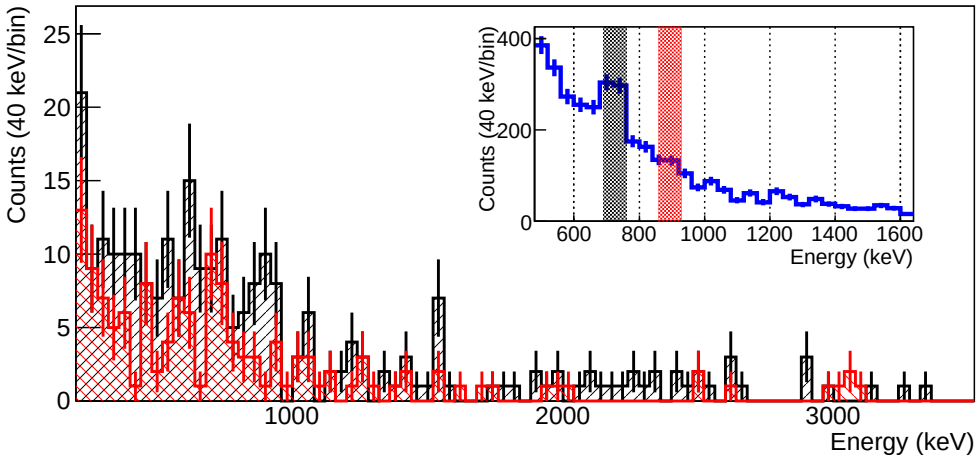

Figure 5.17: Spectrum of γ-rays measured in coincidence with the 2_1^+ and 4_1^+ states in ^{78}Zn. The inset shows the total projection of the γ-γ matrix as well as the gates used. The black histogram shows the spectrum gated in the $2_1^+ \rightarrow 0_{gs}^+$ transition and the red histogram shows the spectrum when gated in the $4_1^+ \rightarrow 2_1^+$ transition. No background subtraction was performed.

to the $2_1^+ \rightarrow 0_{gs}^+$ transition energy and the red gate was set around the $4_1^+ \rightarrow 2_1^+$ transition energy. The black and red histograms show the corresponding spectra. The black histogram shows a structure around 900 keV, which corresponds to the $4_1^+ \rightarrow 2_1^+$ transition. Apart from a self-coincidence, no other significant peaks can be distinguished. This suggests that the high-energy transitions fitted in the spectrum are not feeding the 2_1^+ state and could then correspond to ground-state transitions. Therefore, the value obtained for the cross section was not modified. The red histogram, showing the γ-rays in coincidence with the $4_1^+ \rightarrow 2_1^+$ transition, shows once again the coincidence of the 4_1^+ and 2_1^+ states. No other peak can be distinguished in this coincidence spectrum.

5.1.6 ^{80}Zn

Figure 5.18 shows the known level scheme for ^{80}Zn. The energy of the 2_1^+ state was taken from the adopted values of NNDC. The energy of the 4_1^+ state as well as two transitions recently reported are taken from Ref. (99).

The $2_1^+ \rightarrow 0_{gs}^+$ transition at 1492 keV as well as a transition consistent with the recently reported $4_1^+ \rightarrow 2_1^+$ transition at 482 keV were observed in the Doppler corrected spectrum of ^{80}Zn. The shape of the spectrum at higher energies resembles the one obtained for ^{78}Zn: No transitions are apparent below 2000 keV, and two additional peaks are needed above this energy in order to get a good description of the data. These two peaks were found to be at energies around 3600 keV and 4100 keV. The simulated response to these transitions was included in the fit.

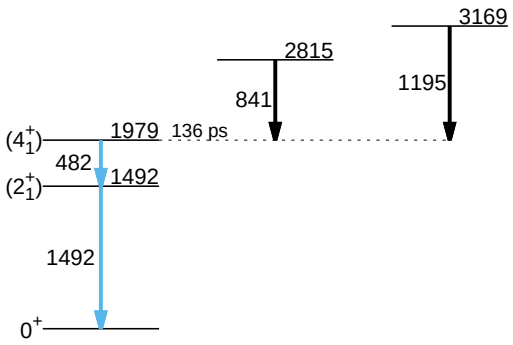

Figure 5.18: Partial level scheme of ^{80}Zn. The yrast band up to the 4_1^+ state is shown. Additionally, two recently reported transitions are presented.

Figure 5.19 shows the Doppler corrected spectrum of ^{80}Zn and the fit that was performed. Add-back up to 15 cm was applied to both the experimental and the simulated data. Due to the low energy of the $4_1^+ \rightarrow 2_1^+$ transition, it was necessary to reduce the atomic background. This was achieved by removing the detectors at backward angles (detectors 1 to 52) from the analysis.

The black points with error bars represent the experimental data. The blue dashed lines show the simulated response functions for the $2_1^+ \rightarrow 0_{gs}^+$ and the $4_1^+ \rightarrow 2_1^+ \rightarrow 0_{gs}^+$ cascade. The green and orange dashed lines represent the simulated responses of the high-energy transitions. The dashed red line show the fitted background and the solid red line corresponds to the total fit. The cross section to populate the 2_1^+ state was 2.7(3) mb. For the 4_1^+ state was 0.8(2) mb. The combined cross section for populating the high-energy states was 1.0(3) mb.

In order to discriminate the possible feeding of these states in the 2_1^+ state, a γ-γ matrix was generated and projections of the γ-rays in coincidence with the 2_1^+ state were performed. Figure 5.20 shows the spectra of γ-rays in coincidence with the low- and the high-energy part of the $2_1^+ \rightarrow 0_{gs}^+$ transition. The inset shows the total projection of the γ-γ matrix together with the gates applied.

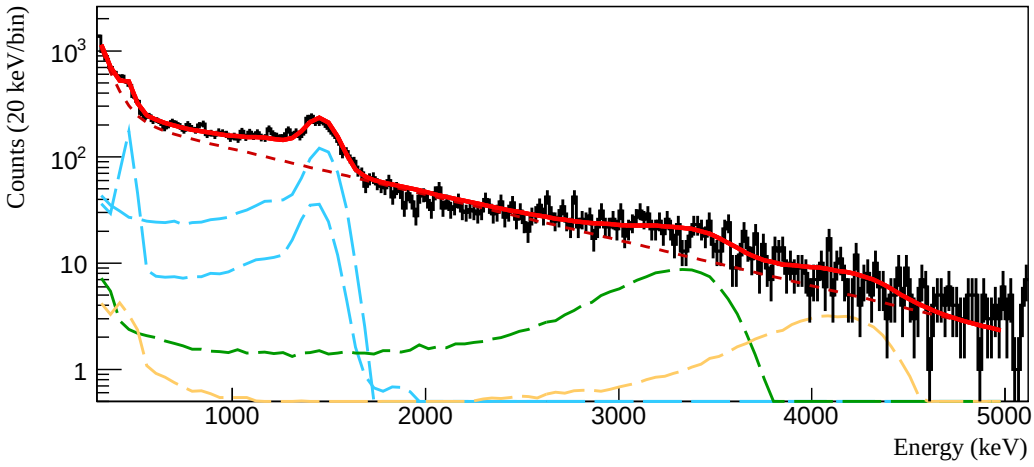

Figure 5.19: Doppler corrected spectrum of ^{80}Zn and fit performed. The experimental spectrum is shown by the black points. The dashed blue, green and yellow lines show the simulated detector responses. The red dashed line shows the fitted background and the red solid line corresponds to the total fit. An add-back up to 15 cm was performed.

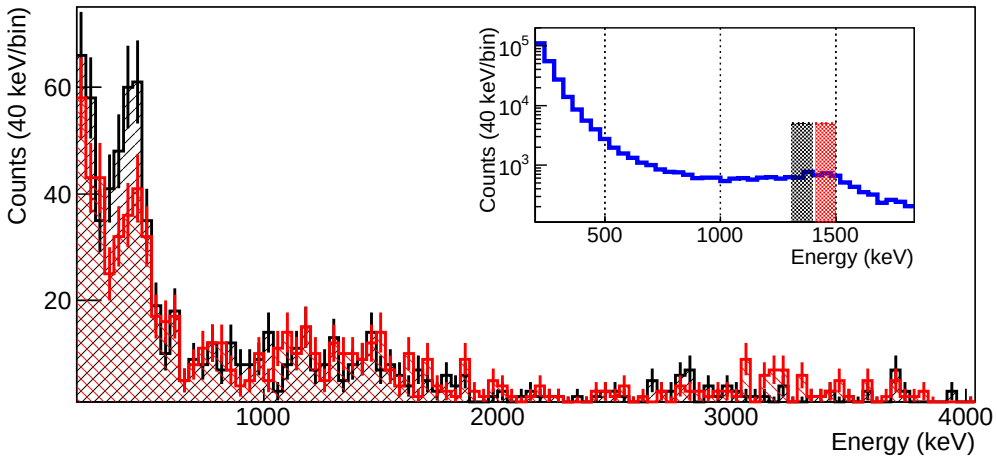

Figure 5.20: Spectrum of γ-rays measured in coincidence with the 2_1^+ state in ^{80}Zn. The inset shows the total projection of the γ-γ matrix as well as the gates used. The black histogram shows the spectrum gated in the low-energy side of the peak and the red histogram shows the spectrum when gating on the high-energy side. No background subtraction was performed.

The presence of the $4_1^+ \rightarrow 2_1^+$ transition is clear when gating on the lower side of the $2_1^+ \rightarrow 0_{gs}^+$ transition peak. This is consistent with the long lifetime of this state reported in Ref. (99). The energy of this peak was found to be 442(7) keV, which is slightly lower than the value reported in the mentioned reference. The high-energy gate shows still indications of the $4_1^+ \rightarrow 2_1^+$ transition, but in none of the gates high-energy transitions can be distinguished, leading to the conclusion that it is not necessary to consider the feeding.

In order to get a better estimate of the cross section, the region between 300-2000 keV was fitted using only the $2_1^+ \rightarrow 0_{gs}^+$ transition and the $4_1^+ \rightarrow 2_1^+$ transition, with an energy consistent with the one found using the coincidence spectrum. Figure 5.21 shows the result of this fit. All the lines have the same meaning as in the previous fit. The cross sections found using this fit are in agreement with the previously obtained values. The effect of the lifetime of the 4_1^+ state is clearly visible in the fit.

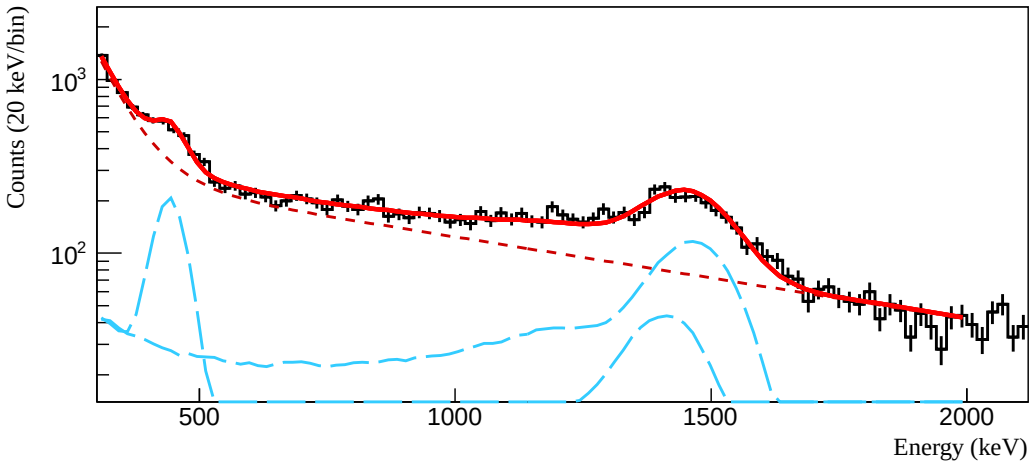

Figure 5.21: Doppler corrected spectrum of ^{80}Zn fitted between 300-2000 keV. The lines in the Figure have the same meaning as in the previous fit. The effect of the lifetime of the 4_1^+ state can be seen by the shift of the peak. No evidence of other transition is observed in this energy range.

5.2 Add-back procedure and angular distribution

In addition to the systematic errors, originating from the simulation of the efficiency of DALI2 and the target thickness, the statistical errors, arising from the fitting procedure, two more contributions to the error were considered: The statistical error due to the add-back procedure and the systematic error resulting from neglecting the angular distribution of the decay radiation.

5.2.1 Add-back procedure

Figure 5.22 shows the cross section for the 2_1^+ state and for the 4_1^+ state obtained for different add-back distances. The left panel shows the results obtained for ^{72}Ni and the right panel shows ^{74}Ni. It can be seen that $\sigma_{(p,p')}^{2_1^+}$ for ^{72}Ni has no change for different add-back distances. This is also the case for $\sigma_{(p,p')}^{4_1^+}$ in ^{74}Ni. Although the results are consistent within error bars, a slight decrease in the 2_1^+ state cross section can be observed for ^{74}Ni. A more significant reduction can be observed for $\sigma_{(p,p')}^{4_1^+}$ in ^{72}Ni.

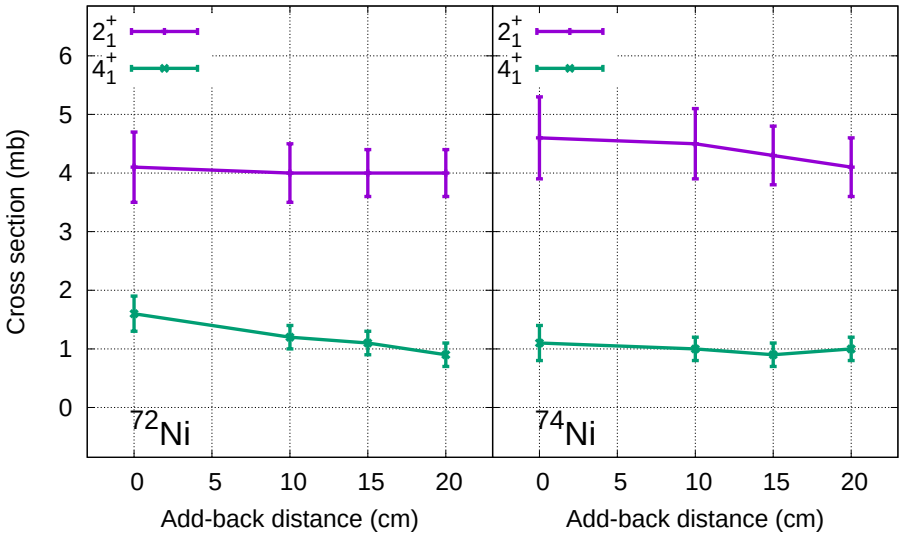

Figure 5.22: Cross section as a function of the add-back distance. The cross sections for the 2_1^+ state as well as for the 4_1^+ state are shown. The left panel shows the case of ^{72}Ni and the right panel shows ^{74}Ni. See text for details.

Two effects are important when performing the add-back procedure: For large add-back distances, the probability to add-up radiation coming from the atomic background increases. This will effectively remove events from the photo-peak and smear them out towards higher energy. For small add-back distances, the γ-rays with energies higher than 1-2 MeV are not properly reconstructed, thus the high-energy feeding will be underestimated. To keep a compromise between the two cases, an add-back distance of 15 cm was used for the experimental data, as shown in the previous section. The difference between the cross sections measured between 10 and 20 cm were in all the cases below 8%. As all values were in agreement within error bars, no systematic error from that add-back procedure was considered.

5.2.2 Angular distribution

All the simulations were performed assuming that the excited states decay isotropically. In order to take into account the error due to any possible alignment of the states, the cross section was obtained for different angular regions of DALI2. Figure 5.23 shows the result obtained for $\sigma^{2_1^+}_{(p,p')}$ and $\sigma^{4_1^+}_{(p,p')}$ in ^{72}Ni and ^{74}Ni.

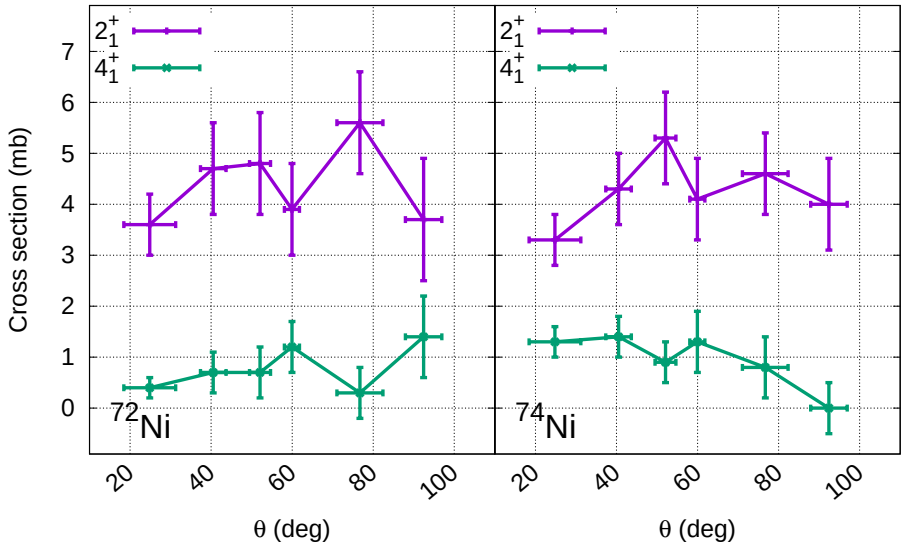

Figure 5.23: Cross section as a function of the DALI2 polar angle. The cross section to populate the 2_1^+ and 4_1^+ states is shown. The left panel shows the result obtained for ^{72}Ni and the right panel the result obtained for ^{80}Zn. See text for details.

In spite of some variations in the cross section, the error bars do not allow for any conclusive statement. No theory for the alignment of the states populated by proton inelastic scattering at relativistic energies is available, but some studies suggest that this reaction generate mainly oblate aligned states (102, 103). Nevertheless, the strong presence of feeding transitions also alter the alignment of the magnetic sub-states contributing to a more spherical distribution.

In order to give estimates of the error in the cross sections due to a possible angular distribution, the two extreme cases of purely prolate and purely oblate alignments were considered. Figure 5.24 show the cross sections for the 2_1^+ and 4_1^+ states when a spherical, a 100% prolate and a 100% oblate angular distribution were taken into account in the simulation. The left panel shows the case of ^{72}Ni and the right panel shows ^{80}Zn.

It can be seen from the plot that the variation of the cross sections for the three cases considered is negligible for the case of ^{72}Ni. For ^{80}Zn, a more pronounced variation is observed. This can be explained by noticing that DALI2 covers almost 4π solid angle. Thus, when considering the full array, the angular distribution of the decay radiation does not affect the cross section calculation. For ^{80}Zn, backward angles detectors were

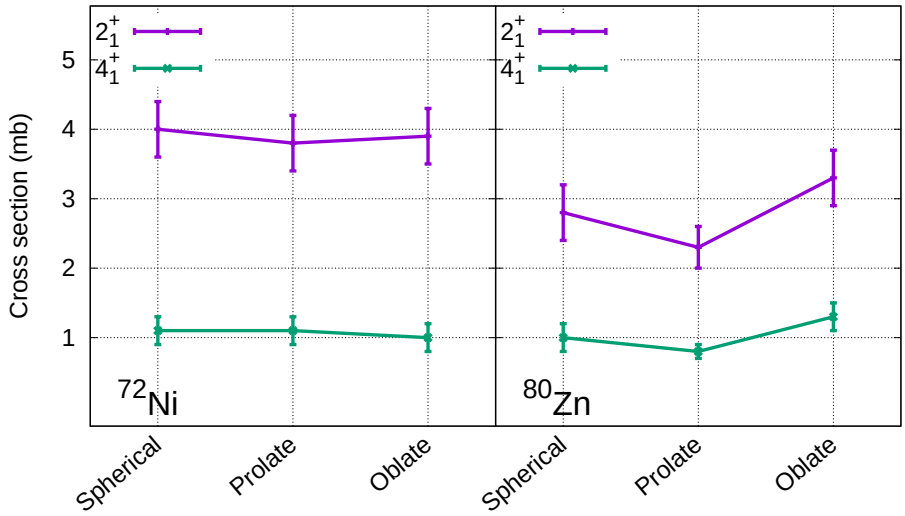

Figure 5.24: Cross section for different alignments of the magnetic sub-states. Spherical, 100% prolate and 100% oblate alignments were considered. No effect is visible for ^{72}Ni, as DALI2 covers almost 4π solid angle. For ^{80}Zn, where backwards detectors were not used, a variation is observed.

not used in order to reduce the atomic background, while for ^{72}Ni, and the rest of the isotopes of interest, all the detectors were used.

As no strong angular dependence of the cross section was observed in Figure 5.23, it is reasonable to assume maximum alignment of 50% (prolate or oblate). This leads to a maximum error in the cross section due to the angular distribution of 9%. This additional error was included only in the cross sections of ^{80}Zn.

5.3 Summary of cross sections

The values of $\sigma^{2_1^+}_{(p,p')}$ and $\sigma^{4_1^+}_{(p,p')}$ obtained for the isotopes of interest are summarized in Table 5.1. The errors due to the add-back procedure and the angular distribution are included. The results are also displayed in Figure 5.25 where the 2_1^+ and 4_1^+ states cross sections are plotted as a function of the neutron number for the two isotopic chains. The arrows in the plot for ^{70}Ni and ^{78}Zn are included to emphasize that only lower limits are reported. For the Ni chain, an increase of $\sigma^{2_1^+}_{(p,p')}$ and a decrease of $\sigma^{4_1^+}_{(p,p')}$ with neutron number can be observed. The trend for the Zn isotopes is not so clear due to

Isotope	$\sigma_{(p,p')}^{2_1^+}$ (mb)	$\sigma_{(p,p')}^{4_1^+}$ (mb)
^{70}Ni	0.4(4)	2.3(6)
^{72}Ni	2.2(5)	1.1(2)
^{74}Ni	3.6(6)	0.8(2)
^{76}Zn	2.0(14)	1.6(8)
^{78}Zn	3.3(7)	1.6(5)
^{80}Zn	2.0(4)	0.8(2)

Table 5.1: Summary of cross sections for the isotopes of interest. Both $\sigma_{(p,p')}^{2_1^+}$ and $\sigma_{(p,p')}^{4_1^+}$ are listed. For ^{70}Zn and ^{78}Zn, the cross sections correspond to lower limits.

the large error bars for ^{76}Zn and the presence of the isomer in ^{78}Zn. However, most likely, the cross section for the closed-neutron shell nucleus ^{80}Zn is smaller than those for its neighboring open-shell isotopes.

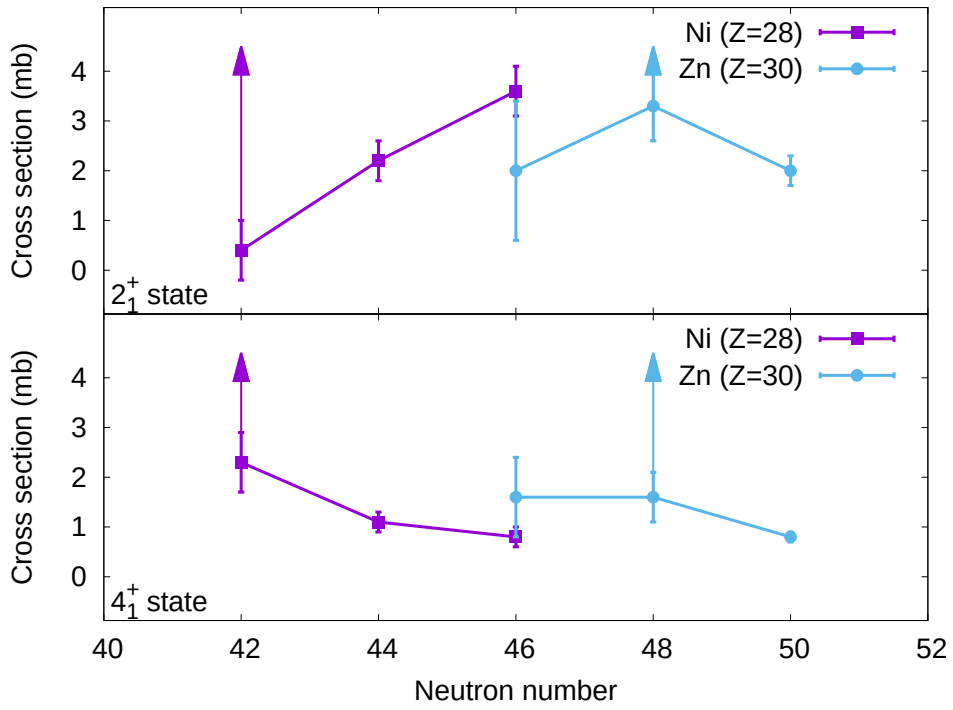

Figure 5.25: Cross section for the isotopes of interest. The $\sigma_{(p,p')}^{2_1^+}$ and $\sigma_{(p,p')}^{4_1^+}$ cross sections are reported for the Ni and Zn isotopes. The arrows are included to emphasize that only lower limits are reported.

The proton inelastic scattering cross section depends on the energy of the incoming ions. Although the energies of the isotopes of interest are relatively similar, in order to draw further conclusion on the structure of the isotopes, the energy dependence has to be removed. This can be done using optical models for the interaction. The next Section describes the calculation of the deformation lengths for the isotopes of interest.

5.4 Deformation lengths and M_n/M_p ratios

The deformation lengths for proton inelastic scattering were estimated using the coupled-channels calculation code ECIS-97 (104, 105). The calculations included a first order, harmonic vibrational model, where the volume, surface and Coulomb potentials were chosen to have the same deformation. An example file showing the parameters used for the calculation can be found in Appendix C.

The optical potentials that were used for the calculations corresponds to the KD02 Global Optical Potentials (31). This potential has been tested up to 200 MeV only, which is below the energy used in this experiment. Nevertheless, among the available potentials this is the one that best suits the experimental conditions.

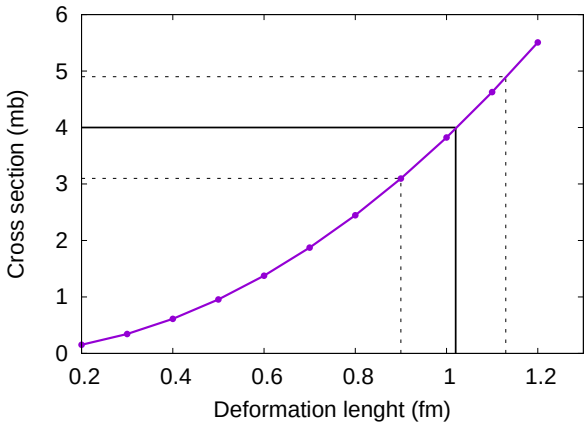

Figure 5.26: Calculation of the deformation length based on the measured cross section. The solid purple line shows the cross section obtained with ECIS-97 as a function of the deformation length. The black solid and dashed lines represent the measured cross section and the errors respectively. These values are used to obtain the corresponding deformation length.

The deformation length for each isotope was obtained by scanning different values until the experimental cross section was reproduced. An example of how this procedure was performed can be seen in Figure 5.26. The purple solid line shows the cross section obtained with ECIS-97 for different values of the deformation length, $\delta_{(p,p')}$. The measured cross section, including the error bar are shown by the horizontal black solid and dashed lines. The vertical lines show the values of the deformation length that reproduce the cross section for the chosen optical model.

The procedure was applied to each isotope and the results are summarized in Figure 5.27, where the deformation lengths for the Ni (purple line) and the Zn (green line) isotopes is plotted as a function of the neutron number. It is important to remember that for ^{70}Ni and ^{78}Zn the values correspond to minimum values due to the presence of the isomeric states. Given the large error bars, the deformation lengths of the different isotopes are rather close in size of about 0.8(2) fm, suggesting that the amplitudes of their vibrations is similar for all the cases within a variation of only about 200 attometers.

To attempt discriminating the neutron and proton contributions to the excitations, the neutron-to-proton matrix element ratio was obtained by combining the measured deformation lengths of proton inelastic scattering with previously performed Coulex

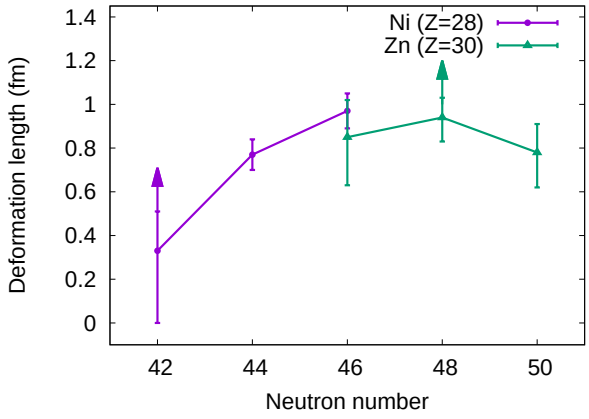

Figure 5.27: Deformation length as a function of neutron number. The purple line shows the results obtained for Ni and the green line the results for Zn isotopes. Within the large error bars, the deformation length of the different isotopes are fairly constant at a value of around 0.8 (2) fm, except for ^{70}Ni which may show a smaller value.

data. This procedure was not applied to ^{70}Ni and ^{78}Zn due to the problems arising from the isomers as discussed before. First, the $B(E2;\ 0^+_{gs} \rightarrow 2^+_1)$ value reported for each isotope was transformed to deformation length, δ_C, using the expression,

$$\delta_C = \frac{1}{4\pi eR}\sqrt{B(E2;\ 0^+_{gs} \rightarrow 2^+_1)}, \tag{5.4}$$

where $R = 1.2A^{1/3}$ is the nuclear radius. The two deformation lengths were then combined using the expression given by Bernstein (34) to obtain M_n/M_p as shown in Equation 2.14. The coefficients b_p and b_n were taken as 0.3 and 0.9 respectively following Ref. (43). The ratio M_n/M_p depends mainly on the ratio between the deformation lengths and does not change significantly for different values of b_p/b_n. Variation of these parameters in the known limits gave an additional 8% error, which was included in the final error bar. The values of the different variables used for the calculation are summarized in Table 5.2.

It can be seen from Equation 2.14 that in the case where $\delta_{(p,p')} = \delta_C$, the ratio $M_n/M_p = N/Z$. Thus, a clearer way to visualize the results is to divide the M_n/M_p ratio by N/Z as shown in Figure 5.28. The blue point corresponds to the result obtained in a previous study (108), which is confirmed by the present data. Since the present work uses a much larger beam energy as compared to Ref. (108), the agreement of the present analysis with the value obtained in Ref. (108) supports the validity of the present analysis, including the choice of optical model.

It can be seen from the plot that the Ni isotopes have $(M_n/M_p)/(N/Z) > 1$. This indicates that the collectivity of the 2^+_1 states of the open neutron-shell Ni isotopes is dominated by the neutrons. Given that the protons form a spherical closed shell, this seems reasonable. For the case of the Zn isotopes, $(M_n/M_p)/(N/Z) \leq 1$. The difference in the value of $(M_n/M_p)/(N/Z)$ between ^{76}Zn and the isotone ^{74}Ni amounts

Isotope	$B(E2)\uparrow$ (e^2fm^4)	δ_C (fm)	$\delta_{(p,p')}$ (fm)	M_n/M_p
^{72}Ni	370(50)	0.58(8)	$0.91^{+0.24}_{-0.33}$	$2.56^{+0.90}_{-0.98}$
^{74}Ni	642^{+216}_{-226}	0.75(26)	$1.02^{+0.11}_{-0.13}$	2.33(86)
^{76}Zn	1450(180)	1.05(13)	$0.83^{+0.22}_{-0.30}$	$1.15^{+0.50}_{-0.58}$
^{80}Zn	750(160)	0.74(16)	$0.78^{+0.13}_{-0.16}$	$1.76^{+0.63}_{-0.65}$

Table 5.2: Deformation lengths and M_n/M_p ratios for the isotopes of interest. The $B(E2)\uparrow$ values were taken from Ref. (41, 42, 43, 106, 107).

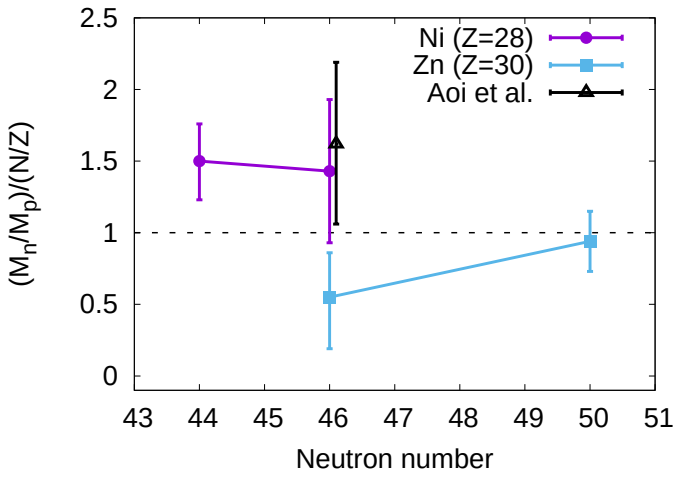

Figure 5.28: Neutron-to-proton matrix element ratios as a function of neutron number. The previously reported measurement by Aoi *et al.* (108) has been confirmed. Nevertheless, the large error bars prevent distinguishing small variations in M_n/M_p.

to a factor of about 3. This nuclear structure effect indicating the presence/absence of a proton shell closure for Ni/Zn isotopes could only be quantified by combining the previously known $B(E2)\uparrow$ values (which considerably differ between ^{74}Ni and ^{76}Zn) with the deformation lengths obtained in this work for inelastic (p, p') reaction cross sections for the first time.

A reduction of the error bars could be obtained by using an array made of detectors with a higher intrinsic resolution, such as $LaBr_3$ or Ge. A tracking of the protons would also benefit the determination of the vertex position, which could in turn improve the Doppler correction and the width of the observed peaks. A plausible scenario for further studies on proton inelastic scattering at relativistic energies is, therefore, the HiSPEC experiment at the upcoming FAIR facility.

CHAPTER 6

SUMMARY AND OUTLOOK

For decades, one of the fundamental pillars of nuclear structure has been the concept of single-particle motion in a mean potential. This view leads to the appereance of shell structure governed by a mean-field with strong spin-orbit interaction. Nevertheless, shell structure changes as one moves away from the stability line. Phenomena such as neutron skins, halos, and changes in the ordering and spacing of energy levels have been observed on the neutron-rich side of the nuclear chart. Of paramount importance to study these shell-evolution effects, are nuclei around doubly-closed shells, for example nuclei around ^{78}Ni ($Z = 28$, $N = 50$). In order to experimentally access these exotic nuclei, advanced facilities such as RIBF at RIKEN, Japan, or the future FAIR facility at Darmstadt, Germany, are needed.

To increase the understanding of the collective behavior of nuclei near the doubly-magic ^{78}Ni, proton inelastic scattering of ^{70,72,74}Ni and ^{76,78,80}Zn off a proton target was performed at RIBF, RIKEN, Japan as part of the first SEASTAR campaign. A detailed analysis of the complex experimental data was performed. This analysis included the calibration of the detectors placed along the BigRIPS and ZeroDegree magnetic separators and the optimization of the Doppler correction for the γ-rays detected in the DALI2 array. In addition, for the first time, the capabilities of the electronics to discriminate multiple particles in one event were implemented.

The $2_1^+ \rightarrow 0_{\rm gs}^+$ and $4_1^+ \rightarrow 2_1^+$ transitions were identified in all the isotopes of interest. With the aid of `Geant4` simulations, the proton inelastic scattering cross sections were

obtained. An increase in the 2_1^+ state cross section with increasing proton number was suggested by the data along the Ni chain. Due to the presence of the seniority isomer in ^{70}Ni, only lower values could be given for this isotope. The cross section to populate the 4_1^+ state decreased with increasing neutron number. In the Zn chain, The 2_1^+ state cross section did not show any significant change. Here again, the presence of the ^{78}Zn isomer prevents to give absolute values for the cross section of this isotope. The 4_1^+ cross sections showed no significant modification.

The ECIS-97 code was used to obtain the deformation lengths of the isotopes of interest based on the measured cross sections. Except for ^{70}Ni, the value of the deformation lengths was roughly constant at a value of 0.8(2) fm. This suggests that all the isotopes have a similar vibrational amplitude. The deformation lengths calculated in this work were combined with the previously measured $B(E2;\ 0^+_{\rm gs} \rightarrow 2^+_1)$ values to obtain the neutron-to-proton matrix element ratios, M_n/M_p, for each isotope. This calculation was performed following the Bernstein approach. For ^{72,74}Ni, $M_n/M_p > N/Z$, indicating that in these isotopes the contribution of the neutrons to the collectivity of the 2_1^+ states is higher than the one of the protons. This behavior can be expected due to the closed proton shell. For ^{76,80}Zn, the M_n/M_p values are smaller than one. Comparison between the isobars ^{74}Ni and ^{76}Zn suggest that the two proton hole configuration in the $f_{7/2}$ shell has more effect in the collectivity than the four-hole neutron $g_{9/2}$ shell. The $M_n/M_p \approx 1$ value obtained for ^{80}Zn may be an indication of an approaching doubly-magic isotope.

The results obtained in this thesis are an important step in the understanding of the difference between the proton and the neutron collectivity in nuclei towards ^{78}Ni, and open new possibilities for proton inelastic scattering experiments. Improvements in the method can be obtained, for example, by using γ-ray detectors with a higher intrinsic resolution, such as $LaBr_3$ or Ge. This scenario will be available within the HISPEC experiments at the coming FAIR facility.

Appendices

APPENDIX A

OPTICAL MATRICES

The coordinates of a particle, $\vec{X}$, can be obtained by using the initial coordinates, $\vec{X}_0$, as

$$\vec{X} = M\vec{X}_0, \tag{A.1}$$

where M is the optical matrix describing a magnetic stage. The vector $\vec{X}$ is given by

$$\vec{X} = (x, a, y, b, \delta), \tag{A.2}$$

where x and a are the position and angle of the particle in the horizontal plane, y and b are the position and angle of the particle in the vertical place and δ is the relative momentum deviation of the particle with respect to the central trajectory. The optical matrix M has the form

$$M = \begin{pmatrix} (x|x) & (x|a) & (x|y) & (x|b) & (x|\delta) \\ (a|x) & (a|a) & (a|y) & (a|b) & (a|\delta) \\ (y|x) & (y|a) & (y|y) & (y|b) & (y|\delta) \\ (b|x) & (b|a) & (b|y) & (b|b) & (b|\delta) \\ (\delta|x) & (\delta|a) & (\delta|y) & (\delta|b) & (\delta|\delta) \end{pmatrix}. \tag{A.3}$$

The optical matrices used to perform the reconstruction of the position of the particles along the separator are listed here using the format described by equation A.3.

$$M(\text{F3-F5}) = \begin{pmatrix} 0.917467 & -0.018721 & 0 & 0 & -0.0316630 \\ -0.00520039 & 1.09006 & 0 & 0 & 1.88156 \\ 0 & 0 & 1.07852 & 0.331125 & 0 \\ 0 & 0 & 0.0325887 & 0.937205 & 0 \\ 0 & 0 & 0 & 0 & 1 \\ 31.6051 & -0.0129966 & 0 & 0 & 89.6693 \end{pmatrix}. \tag{A.4}$$

$$M(\text{F5-F7}) = \begin{pmatrix} 1.09101 & -0.0172247 & 0 & 0 & -0.00277197 \\ 0.020415 & 0.916262 & 0 & 0 & -1.72349 \\ 0 & 0 & 0.939059 & 0.336060 & 0 \\ 0 & 0 & 0.0255208 & 1.07403 & 0 \\ 0 & 0 & 0 & 0 & 1 \\ -34.4457 & 0.590371 & 0 & 0 & 89.8155 \end{pmatrix}. \tag{A.5}$$

$$M(\text{F8-F9}) = \begin{pmatrix} -2.00438 & 0.248732 & 0 & 0 & -0.346472 \\ -0.0576387 & -0.491755 & 0 & 0 & 0.687606 \\ 0 & 0 & -2.11414 & -0.0222608 & 0 \\ 0 & 0 & 0.18493 & -0.471059 & 0 \\ 0 & 0 & 0 & 0 & 1 \\ -24.8252 & 0.0115515 & 0 & 0 & 40.9434 \end{pmatrix}. \tag{A.6}$$

$$M(\text{F9-F11}) = \begin{pmatrix} 1 & 0 & 0 & 0 & -0.00721884 \\ 0 & 1 & 0 & 0 & 1.39695 \\ 0 & 0 & 0.525997 & 0.0521447 & 0 \\ 0 & 0 & -0.179933 & 1.88332 & 0 \\ 0 & 0 & 0 & 0 & 1 \\ 24 & 0 & 0 & 0 & 80.2942 \end{pmatrix}. \tag{A.7}$$

APPENDIX B

CALCULATION OF A/Q

To deduce Equations 3.23 and 3.24, the initial assumption is that the A/Q of the particle does not change when passing through the degrader, as expressed in Equation 3.22. This expression can be re-written as

$$\gamma_{57}\beta_{57} = R\gamma_{35}\beta_{35}, \tag{B.1}$$

where

$$R = \frac{(B\rho)_{57}}{(B\rho)_{35}}.$$

On the other hand, a relation between the ToF_{37} and the velocities between F3-F5 and F5-F7 is given by Equation 3.19. This equation can be re-written as

$$c\text{ToF}_{37} = \frac{L_{35}}{\beta_{35}} + \frac{L_{57}}{\beta_{57}}. \tag{B.2}$$

Solving this equation for β_{35}

$$\frac{L_{35}}{\beta_{35}} = \frac{c\text{ToF}_{37}\beta_{57} - L_{57}}{\beta_{57}} \tag{B.3}$$

$$\beta_{35} = \frac{L_{35}\beta_{57}}{c\text{ToF}_{37}\beta_{57} - L_{57}}, \tag{B.4}$$

is obtained. Using the definition of γ_{35} and Equation B.4

$$\gamma_{35}^2 = \frac{(c\text{ToF}_{37}\beta_{57} - L_{57})^2}{(c\text{ToF}_{37}\beta_{57} - L_{57})^2 - L_{35}^2\beta_{57}^2}, \tag{B.5}$$

is obtained. Taking the square of both sides of Equation B.1 and using the definition of γ_{57} results in

$$\frac{\beta_{57}^2}{1-\beta_{57}^2} = R^2\gamma_{35}^2\beta_{35}^2. \tag{B.6}$$

Replacing β_{35} and γ_{35} from Equations B.4 and B.5 and simplifying,

$$\frac{\beta_{57}^2}{1-\beta_{57}^2} = R^2\left[\frac{(c\text{ToF}_{37}\beta_{57}-L_{57})^2}{(c\text{ToF}_{37}\beta_{57}-L_{57})^2 - L_{35}^2\beta_{57}^2}\right]\left[\frac{L_{35}^2\beta_{57}^2}{(c\text{ToF}_{37}\beta_{57}-L_{57})^2}\right] \tag{B.7}$$

$$\frac{1}{1-\beta_{57}^2} = R^2\frac{L_{35}^2\beta_{57}^2}{(c\text{ToF}_{37}\beta_{57}-L_{57})^2 - L_{35}^2\beta_{57}^2}, \tag{B.8}$$

is obtained. Solving for β_{57} gives the quadratic equation

$$\left[c^2\text{ToF}_{37}^2 - L_{35}^2 + R^2L_{35}^2\right]\beta_{57}^2 - \left[2c\text{ToF}_{37}L_{57}\right]\beta_{57} + \left[L_{57}^2 - R^2L_{35}\right] = 0. \tag{B.9}$$

The solution of this equation is given by

$$\beta_{57} = \frac{-B+\sqrt{B^2-4AC}}{2A}, \tag{B.10}$$

with

$$\begin{aligned} A &= c^2\text{ToF}_{37}^2 - L_{35}^2 + R^2L_{35}^2 \\ B &= -2c\text{ToF}_{37}L_{57} \\ C &= L_{57}^2 - R^2L_{35}, \end{aligned}$$

where the negative root has been removed to avoid a negative solution. The discriminant $D = B^2 - 4AC$ can be simplified as follows:

$$D = 4c^2\text{ToF}_{37}^2L_{57}^2 - 4\left(c^2\text{ToF}_{37}^2 - L_{35}^2 + R^2L_{35}^2\right)\left(L_{57}^2 - R^2L_{35}\right) \tag{B.11}$$

$$D = 4\left[R^2c^2\text{ToF}_{37}^2L_{35}^2 + L_{35}^2L_{57}^2 - R^2L_{35}^4 - R^2L_{35}^2L_{57}^2 + R^4L_{35}^2\right] \tag{B.12}$$

$$D = 4L_{35}^2\left[R^2c^2\text{ToF}_{37}^2 + L_{35}^2(R^4-R^2) + L_{57}^2(1-R^2)\right]. \tag{B.13}$$

By making the definition

$$a = \sqrt{R^2c^2\text{ToF}_{37}^2 + L_{35}^2(R^4-R^2) + L_{57}^2(1-R^2)}, \tag{B.14}$$

the solution for β_{57} is given by

$$\beta_{57} = \frac{aL_{35} + c\text{ToF}_{37}L_{57}}{c^2\text{ToF}_{37}^2 + L_{35}^2(R^2-1)}. \tag{B.15}$$

Replacing this result in Equation B.2 and simplifying

$$\frac{L_{35}}{\beta_{35}} = c\text{ToF}_{37} - L_{57}\left[\frac{c^2\text{ToF}_{37}^2 + L_{35}^2(R^2-1)}{aL_{35} + c\text{ToF}_{37}L_{57}}\right] \tag{B.16}$$

$$\frac{L_{35}}{\beta_{35}} = \frac{c\text{ToF}_{37}L_{35}a - L_{35}^2L_{57}(R^2-1)}{c\text{ToF}_{37}L_{57} + L_{35}a}. \tag{B.17}$$

is obtained. Finally, solving for β_{35} results in

$$\beta_{35} = \frac{aL_{35} + c\text{ToF}_{37}L_{57}}{ac\text{ToF}_{37} + L_{35}L_{57}(1-R^2)}, \tag{B.18}$$

which are the equations written in Chapter 3, section 3.2.3.4.

B. CALCULATION OF A/Q

APPENDIX C

ECIS-97 INPUT FILE

Figure C.1 shows an example of the input file used for the ECIS-97 code. It describes the 2_1^+ state on ^{72}Ni in a first order, harmonic vibrational model. Card 2 contains the parameters related to the model, the interaction and the integration. Card 3 mainly deals with the output parametes. The following cards contain the different parameters of the nulcear states and the optical potentials. Further documentation on the input file can be found in Refs. (104, 105).

```
72Ni, vib|rati,on 2|39.39, MeV|/u K,D02 |     ,     |                    card 1
FFFFFtFtFFttFFFtFFFFFFFFtFFFFFFFFFFFFFFFFFFFFFFFFF                     card 2
FtFFFFFFFFFFFFFFFFFFFFFFFFFFFFFFFFFFFFFtFtFFFFFFFFF                    card 3
    2 2000                                                             card 4
                                                                       card 5
0.       +   17236.1       0.0      72.0       1.0       28.0         nuclear state (g.s)
    0                                                                  number of phonons
2.       +    1.096                                                   nuclear state (2+)
    1    1                                                             number of phonons
    2    0   0.91                                                     phonon description
  10.9383    1.20645   0.66709                                        real volume
  13.9238    1.20645   0.66709                                        im volume
                                                                      real surface
  0.08984    1.27646   0.55618                                       im surface
  2.28708    1.02988   0.59000                                       real s.o.
                                                                      im s.o.
  1.24870    0.60000                                                 Coulomb
                                                                      s.o. Coulomb
      0.02       0.1     1.5                                        equidistant angles
FIN
```

Figure C.1: Example of ECIS-97 input file.

REFERENCES

[1] T. Otsuka, T. Suzuki, R. Fujimoto, H. Grawe, and Y. Akaishi. **Evolution of Nuclear Shells due to the Tensor Force**. *Phys. Rev. Lett.*, **95**:232502, Nov 2005. 1, 7

[2] S. Beane, W. Detmold, K. Orginos, and M. Savage. **Nuclear physics from lattice QCD**. *Progress in Particle and Nuclear Physics*, **66**(1):1 – 40, 2011. 1

[3] E. Chang, W. Detmold, K. Orginos, et al. **Magnetic structure of light nuclei from lattice QCD**. *Phys. Rev. D*, **92**:114502, Dec 2015. 1

[4] G. Hagen, A. Ekstrom, C. Forssen, et al. **Neutron and weak-charge distributions of the ^{48}Ca nucleus**. *Nat Phys*, **12**(2):186–190, Feb 2016. Article. 2

[5] G. Hagen, T. Papenbrock, M. Hjorth-Jensen, and D. J. Dean. **Coupled-cluster computations of atomic nuclei**. *Reports on Progress in Physics*, **77**(9):096302, 2014. 2

[6] F. Ameil, M. Danchev, P. Boutachkov, et al. **Time of flight with a segmented plastic finger detector at high particle rate**. In *GSI Scientific Report 2011*. GSI, Darmstadt, 2012. 2

[7] M. L. Cortés, H. Schaffner, I. Kojouharov, et al. **Development and test of a segmented Time-of-Flight plastic detector**. In *GSI Scientific Report 2013*. GSI, Darmstadt, 2014. 2

[8] S. Akkoyun, A. Algora, B. Alikhani, et al. **AGATA Advanced GAmma Tracking Array**. *Nuclear Instruments and Methods in Physics Research Section A: Accelerators, Spectrometers, Detectors and Associated Equipment*, **668**:26 – 58, 2012. 2

[9] I. Lee, R. Clark, M. Cromaz, et al. **GRETINA: A gamma ray energy tracking array**. *Nuclear Physics A*, **746**:255 – 259, 2004. Proceedings of the Sixth International Conference on Radioactive Nuclear Beams (RNB6). 2

[10] C. LOUCHART, J. GHELLER, P. CHESNY, ET AL. **The PRESPEC liquid-hydrogen target for in-beam gamma spectroscopy of exotic nuclei at GSI**. *Nuclear Instruments and Methods in Physics Research Section A: Accelerators, Spectrometers, Detectors and Associated Equipment*, **736**:81 – 87, 2014. 3

[11] A. OBERTELLI, A. DELBART, S. ANVAR, ET AL. **MINOS: A vertex tracker coupled to a thick liquid-hydrogen target for in-beam spectroscopy of exotic nuclei**. *The European Physical Journal A*, **50**(1), 2014. 3, 24, 34

[12] F. WIENHOLTZ, D. BECK, K. BLAUM, ET AL. **Masses of exotic calcium isotopes pin down nuclear forces**. *Nature*, **498**(7454):346–349, Jun 2013. Letter. 3

[13] D. STEPPENBECK, S. TAKEUCHI, N. AOI, ET AL. **Evidence for a new nuclear 'magic number' from the level structure of 54Ca**. *Nature*, **502**(7470):207–210, Oct 2013. Letter. 3

[14] R. F. GARCIA RUIZ, M. L. BISSELL, K. BLAUM, ET AL. **Unexpectedly large charge radii of neutron-rich calcium isotopes**. *Nat Phys*, **advance online publication**, Feb 2016. Article. 3

[15] R. KANUNGO, C. NOCIFORO, A. PROCHAZKA, ET AL. **One-Neutron Removal Measurement Reveals ^{24}O as a New Doubly Magic Nucleus**. *Phys. Rev. Lett.*, **102**:152501, Apr 2009. 3

[16] B. BASTIN, S. GRÉVY, D. SOHLER, ET AL. **Collapse of the $N = 28$ Shell Closure in ^{42}Si**. *Phys. Rev. Lett.*, **99**:022503, Jul 2007. 3, 7

[17] G. LORUSSO, S. NISHIMURA, Z. Y. XU, ET AL. **β-Decay Half-Lives of 110 Neutron-Rich Nuclei across the $N = 82$ Shell Gap: Implications for the Mechanism and Universality of the Astrophysical r Process**. *Phys. Rev. Lett.*, **114**:192501, May 2015. 3

[18] K. S. KRANE. *Introductory Nuclear Physics*. John Wiley & Sons, Inc., third edition, 1988. 6, 7

[19] R. F. CASTEN. *Nuclear Structure from a Simple Perspective*. Oxford University Press, second edition, 2000. 6, 7, 8, 13

[20] M. G. MAYER. **On Closed Shells in Nuclei. II**. *Phys. Rev.*, **75**:1969–1970, Jun 1949. 6

[21] O. HAXEL, J. H. D. JENSEN, AND H. E. SUESS. **On the "Magic Numbers" in Nuclear Structure**. *Phys. Rev.*, **75**:1766–1766, Jun 1949. 6

[22] R. V. F. JANSSENS. **Nuclear physics: Unexpected doubly magic nucleus**. *Nature*, **459**(7250):1069–1070, Jun 2009. 7

[23] N. PIETRALLA AND O. M. GORBACHENKO. **Evolution of the "β excitation" in axially symmetric transitional nuclei**. *Phys. Rev. C*, **70**:011304, Jul 2004. 9

[24] I. E. MCCARTHY. *Nuclear Reactions*. Pergamon Press, first edition, 1970. 10

[25] H. SCHEIT. *Low-Lying Collective Excitations in Neutron-Rich Even-Even Sulfur and Argon Isotopes Studied via Intermediate-Energy Coulomb Excitation and Proton Scattering*. PhD thesis, Department of Physics and Astronomy, Michigan State University, 1998. 10, 12

[26] P. E. HODGSON. **The Optical Model of the Nucleon-Nucleus Interaction**. *Annual Review of Nuclear Science*, **17**(1):1–32, 1967. 10

[27] J. J. KELLY, M. A. KHANDAKER, P. BOBERG, ET AL. **Neutron and proton transition densities from ^{32,34}S(*p* , *p* ') at E_p=318 MeV. I. Isoscalar densities for ^{32}S**. *Phys. Rev. C*, **44**:1963–1977, Nov 1991. 10

[28] A. LAGOYANNIS, F. AUGER, A. MUSUMARRA, ET AL. **Probing the ^{6}He halo structure with elastic and inelastic proton scattering**. *Physics Letters B*, **518**(12):27 – 33, 2001. 10

[29] S. STEPANTSOV, D. BOGDANOV, A. FOMICHEV, ET AL. **24.5 AMeV ^{6}He+p elastic and inelastic scattering**. *Physics Letters B*, **542**(12):35 – 42, 2002. 10

[30] F. D. BECCHETTI AND G. W. GREENLEES. **Nucleon-Nucleus Optical-Model Parameters, $A > 40$, $E < 50$ MeV**. *Phys. Rev.*, **182**:1190–1209, Jun 1969. 11

[31] A. KONING AND J. DELAROCHE. **Local and global nucleon optical models from 1 keV to 200 MeV**. *Nuclear Physics A*, **713**(34):231 – 310, 2003. 11, 108

[32] J.-P. JEUKENNE, A. LEJEUNE, AND C. MAHAUX. **Optical-model potential in finite nuclei from Reid's hard core interaction**. *Phys. Rev. C*, **16**:80–96, Jul 1977. 11

[33] N. ALAMANOS AND A. GILLIBERT. **Selected Topics in Reaction Studies with Exotic Nuclei**. In *The Euroschool Lectures on Physics with Exotic Beams*, **I**. Springer, 2004. 12

[34] A. BERNSTEIN, V. BROWN, AND V. MADSEN. **Neutron and proton transition matrix elements and inelastic hadron scattering**. *Physics Letters B*, **103**(45):255 – 258, 1981. 12, 110

[35] V. A. MADSEN, V. R. BROWN, AND J. D. ANDERSON. **Differences of deformation parameter β for different transition mechanisms; comparison with data**. *Phys. Rev. C*, **12**:1205–1211, Oct 1975. 13

[36] O. SORLIN AND M.-G. PORQUET. **Nuclear magic numbers: New features far from stability**. *Progress in Particle and Nuclear Physics*, **61**(2):602 – 673, 2008. 13

[37] M. CHARTIER, B. BLANK, S. CZAJKOWSKI, ET AL. **5th International Conference on Radioactive Nuclear Beams Discovery of doubly-magic 48Ni at GANIL**. *Nuclear Physics A*, **701**(1):433 – 436, 2002. 13

[38] T. OHNISHI, T. KUBO, K. KUSAKA, ET AL. **Identification of 45 New Neutron-Rich Isotopes Produced by In-Flight Fission of a ^{238}U Beam at 345 MeV/nucleon**. *Journal of the Physical Society of Japan*, **79**(7):073201, 2010. 13

[39] I. TALMI. *Simple Models of Complex Nuclei: Shell Model and Interacting Boson Model*. CRC Press, first edition, 1993. 13

[40] B. PRITYCHENKO, J. CHOQUETTE, M. HOROI, B. KARAMY, AND B. SINGH. **An update of the B(E2) evaluation for transitions in eveneven nuclei near**. *Atomic Data and Nuclear Data Tables*, **98**(4):798 – 811, 2012. 14

[41] O. PERRU, O. SORLIN, S. FRANCHOO, ET AL. **Enhanced Core Polarization in ^{70}Ni and ^{74}Zn**. *Phys. Rev. Lett.*, **96**:232501, Jun 2006. 14, 110

[42] K. KOLOS, D. MILLER, R. GRZYWACZ, ET AL. **Direct Lifetime Measurements of the Excited States in ^{72}Ni**. *Phys. Rev. Lett.*, **116**:122502, Mar 2016. 14, 110

[43] T. MARCHI, G. DE ANGELIS, J. J. VALIENTE-DOBÓN, ET AL. **Quadrupole Transition Strength in the ^{74}Ni Nucleus and Core Polarization Effects in the Neutron-Rich Ni Isotopes**. *Phys. Rev. Lett.*, **113**:182501, Oct 2014. 14, 110

[44] S. PÉRU AND M. MARTINI. **Mean field based calculations with the Gogny force: Some theoretical tools to explore the nuclear structure**. *The European Physical Journal A*, **50**(5):1–35, 2014. 14

[45] C. B. HINKE, M. BOHMER, P. BOUTACHKOV, ET AL. **Superallowed Gamow-Teller decay of the doubly magic nucleus ^{100}Sn**. *Nature*, **486**(7403):341–345, Jun 2012. 14

[46] N. N. D. CENTER. **Table of Isotopes**. Accessed: 05.05.2016. 15, 85

[47] A. GOTTBERG. **Target materials for exotic ISOL beams**. *Nuclear Instruments and Methods in Physics Research Section B: Beam Interactions with Materials and Atoms*, **376**:8 – 15, 2016. Proceedings of the XVIIth International Conference on Electromagnetic Isotope Separators and Related Topics (EMIS2015), Grand Rapids, MI, U.S.A., 11-15 May 2015. 17

[48] M. BORGE. **Highlights of the ISOLDE facility and the HIE-ISOLDE project**. *Nuclear Instruments and Methods in Physics Research Section B: Beam Interactions with Materials and Atoms*, pages –, 2016. In Press. 17

[49] PRETEA, G., ANDRIGHETTO, A., MANZOLARO, M., ET AL. **The SPES project at the INFN-Laboratori Nazionali di Legnaro**. *EPJ Web of Conferences*, **66**:11030, 2014. 17

[50] H. GEISSEL, P. ARMBRUSTER, K. BEHR, ET AL. **The GSI projectile fragment separator (FRS): a versatile magnetic system for relativistic heavy ions**. *Nuclear Instruments and Methods in Physics Research Section B: Beam Interactions with Materials and Atoms*, **70**(1):286 – 297, 1992. 17, 20

[51] T. KUBO, D. KAMEDA, H. SUZUKI, ET AL. **BigRIPS separator and ZeroDegree spectrometer at RIKEN RI Beam Factory**. *Progress of Theoretical and Experimental Physics*, **2012**(1), 2012. 17, 20, 24, 26

[52] D. MORRISSEY, B. SHERRILL, M. STEINER, A. STOLZ, AND I. WIEDENHOEVER. **Commissioning the A1900 projectile fragment separator**. *Nuclear Instruments and Methods in Physics Research Section B: Beam Interactions with Materials and Atoms*, **204**:90 – 96, 2003. 14th International Conference on Electromagnetic Isotope Separators and Techniques Related to their Applications. 17, 20

[53] M. SAINT-LAURENT. **The LISE spectrometer at GANIL**. *Nuclear Instruments and Methods in Physics Research Section B: Beam Interactions with Materials and Atoms*, **26**(1):273 – 279, 1987. 17, 20

[54] R. E. LAXDAL, A. C. MORTON, AND P. SCHAFFER. **Radioactive Ion Beams and Radiopharmaceuticals**. In A. W. CHAO AND W. CHOU, editors, *Reviews of Accelerator Science and Technology*, **6**. World Scientific Publishing Company, 2013. 18

[55] D. J. MORRISSEY AND B. M. SHERRILL. **In-Flight Separation of Projectile Fragments**. In *The Euroschool Lectures on Physics with Exotic Beams*, **I**. Springer, 2004. 18

[56] D. J. MORRISSEY, L. F. OLIVEIRA, J. O. RASMUSSEN, ET AL. **Microscopic and Macroscopic Model Calculations of Relativistic Heavy-Ion Fragmentation Reactions**. *Phys. Rev. Lett.*, **43**:1139–1142, Oct 1979. 18

[57] J. HÜFNER, K. SCHÄFER, AND B. SCHÜRMANN. **Abrasion-ablation in reactions between relativistic heavy ions**. *Phys. Rev. C*, **12**:1888–1898, Dec 1975. 18

[58] H. SUZUKI, T. KUBO, N. FUKUDA, ET AL. **Production cross section measurements of radioactive isotopes by BigRIPS separator at RIKEN RI Beam Factory**. *Nuclear Instruments and Methods in Physics Research Section B: Beam Interactions with Materials and Atoms*, **317, Part B**:756 – 768, 2013. XVIth International Conference on ElectroMagnetic Isotope Separators and Techniques Related to their Applications, December 27, 2012 at Matsue, Japan. 18

[59] M. BERNAS, C. ENGELMANN, P. ARMBRUSTER, ET AL. **Discovery and cross-section measurement of 58 new fission products in projectile-fission of 750 A MeV ^{238}U**. *Physics Letters B*, **415**(2):111 – 116, 1997. 18

[60] P. ARMBRUSTER, M. BERNAS, S. CZAJKOWSKI, ET AL. **Low-energy fission investigated in reactions of 750 AMeV ^{238}U-ions with Pb and Be targets**. *Zeitschrift für Physik A Hadrons and Nuclei*, **355**(1):191–201, 1996. 18

[61] T. BAUMANN. **Minicourse on Experimental techniques at the NSCL. Fragment Separators**, August 2001. 19

[62] H. GEISSEL, G. MUNZENBERG, , AND K. RIISAGER. **Secondary Exotic Nuclear Beams**. *Annual Review of Nuclear and Particle Science*, **45**(1):163–203, 1995. 19

[63] H. GEISSEL, H. WEICK, M. WINKLER, G. MÜNZENBERG, AND M. YAVOR. **Ion-optical layout of a powerful next-generation pre-separator for in-flight separation of relativistic rare isotopes**. *Nuclear Instruments and Methods in Physics Research Section B: Beam Interactions with Materials and Atoms*, **247**(2):368 – 376, 2006. 19

[64] N. FUKUDA, T. KUBO, T. OHNISHI, ET AL. **Identification and separation of radioactive isotope beams by the BigRIPS separator at the RIKEN RI Beam Factory**. *Nuclear Instruments and Methods in Physics Research Section B: Beam Interactions with Materials and Atoms*, **317, Part B**:323 – 332, 2013. XVIth International Conference on Electro-Magnetic Isotope Separators and Techniques Related to their Applications, December 27, 2012 at Matsue, Japan. 19

[65] G. F. KNOLL. *Radiation Detection and Measurement*. John Wiley & Sons, Inc., fourth edition, 2010. 20, 21

[66] W. R. LEO. *Techniques for Nuclear and Particle Physics Experiments*. Springer-Verlag, second revised edition, 1994. 20, 21, 67

[67] P. DOORNENBAL. **In-beam gamma-ray spectroscopy at the RIBF**. *Progress of Theoretical and Experimental Physics*, **2012**(1), 2012. 23, 24

[68] P. DOORNENBAL, P. REITER, H. GRAWE, ET AL. **Lifetime effects for high-resolution gamma-ray spectroscopy at relativistic energies and their implications for the RISING spectrometer**. *Nuclear Instruments and Methods in Physics Research Section A: Accelerators, Spectrometers, Detectors and Associated Equipment*, **613**(2):218 – 225, 2010. 24

[69] P. DOORNENBAL AND A. OBERTELLI. **RIKEN proposal for scientific program: Shell evolution and search for two-plus states at the RIBF (SEASTAR)**. Unpublished, 2013. 24

[70] Y. YANO. **The RIKEN RI Beam Factory Project: A status report**. *Nuclear Instruments and Methods in Physics Research Section B: Beam Interactions with Materials and Atoms*, **261**(12):1009 – 1013, 2007. 24

[71] S. TAKEUCHI, T. MOTOBAYASHI, Y. TOGANO, ET AL. **DALI2: A NaI(Tl) detector array for measurements of rays from fast nuclei**. *Nuclear Instruments and Methods in Physics Research Section A: Accelerators, Spectrometers, Detectors and Associated Equipment*, **763**:596 – 603, 2014. 24, 39, 67

[72] H. OKUNO, N. FUKUNISHI, AND O. KAMIGAITO. **Progress of RIBF accelerators**. *Progress of Theoretical and Experimental Physics*, **2012**(1), 2012. 25

[73] T. NAKAGAWA, M. KIDERA, Y. HIGURASHI, ET AL. **New superconducting electron cyclotron resonance ion source for RIKEN RI beam factory projecta)**. *Review of Scientific Instruments*, **79**(2), 2008. 25

[74] Y. HIGURASHI, J. OHNISHI, T. NAKAGAWA, ET AL. **Results for RIKEN superconducting electron cyclotron resonance ion source with 28 GHz microwave**. In *RIKEN Accelerator Progress Report*, **45**. RIKEN Nishina Center for Accelerator-Based Science, 2012. 25

[75] N. SAKAMOTO, M. FUJIMAKI, N. FUKUNISHI, ET AL. **Performance of new injector RILAC2 for RIKEN RI-Beam Factory**. In *Proceedings of LINAC2014*, 2014. 25

[76] H. IMAO, H. OKUNO, H. KUBOKI, ET AL. **Charge stripping of ^{238}U ion beam by helium gas stripper**. *Physical Review Special Topics - Accelerators and Beams*, **15**:123501, Dec 2012. 26

[77] H. OKUNO, N. FUKUNISHI, H. HASEBE, ET AL. **Charge strippers for Radioisotope Beam Factory at RIKEN**. *Journal of Radioanalytical and Nuclear Chemistry*, **299**(2):945–949, 2013. 26

[78] H. HASEBE, H. OKUNO, H. KUBOKI, ET AL. **Development of rotating beryllium disk stripper**. *Journal of Radioanalytical and Nuclear Chemistry*, **305**(3):825–829, 2015. 26

[79] T. KUBO. **Status and features of Big-RIPS separator project**, November 2005. Presentation at the RIBF Technical Advisory Committee TAC05. 27

[80] P.-A. SÖDERSTRÖM, S. NISHIMURA, P. DOORNENBAL, ET AL. **Installation and commissioning of EURICA Euroball-RIKEN Cluster Array**. *Nuclear Instruments and Methods in Physics Research Section B: Beam Interactions with Materials and Atoms*, **317, Part B**:649 – 652, 2013. XVIth International Conference on ElectroMagnetic Isotope Separators and Techniques Related to their Applications, December 27, 2012 at Matsue, Japan. 28

[81] K. KIMURA, T. IZUMIKAWA, R. KOYAMA, ET AL. **High-rate particle identification of high-energy heavy ions using a tilted electrode gas ionization chamber**. *Nuclear Instruments and Methods in Physics Research Section A: Accelerators, Spectrometers, Detectors and Associated Equipment*, **538**(13):608 – 614, 2005. 29

[82] H. KUMAGAI, A. OZAWA, N. FUKUDA, K. SÜMMERER, AND I. TANIHATA. **Delay-line PPAC for high-energy light ions**. *Nuclear Instruments and Methods in Physics Research Section A: Accelerators, Spectrometers, Detectors and Associated Equipment*, **470**(3):562 – 570, 2001. 31

[83] H. KUMAGAI, T. OHNISHI, N. FUKUDA, ET AL. **Development of Parallel Plate Avalanche Counter (PPAC) for BigRIPS fragment separator**. *Nuclear Instruments and Methods in Physics Research Section B: Beam Interactions with Materials and Atoms*, **317, Part B**:717 – 727, 2013. XVIth International Conference on ElectroMagnetic Isotope Separators and Techniques Related to their Applications, December 27, 2012 at Matsue, Japan. 31, 32, 46

[84] K. MAKINO AND M. BERZ. **COSY INFINITY Version 9**. *Nuclear Instruments and Methods in Physics Research Section A: Accelerators, Spectrometers, Detectors and Associated Equipment*, **558**(1):346 – 350, 2006. Proceedings of the 8th International Computational Accelerator Physics ConferenceICAP 20048th International Computational Accelerator Physics Conference. 33

[85] OBERTELLI, A. AND UESAKA, T. **Hydrogen targets for exotic-nuclei studies developed over the past 10 years**. *Eur. Phys. J. A*, **47**(9):105, 2011. 34

[86] C. SANTAMARIA. *Quest for new nuclear magic numbers with MINOS*. PhD thesis, Université Paris-Sud XI, 2015. 34, 35, 37, 38, 43, 69

[87] Y. GIOMATARIS, P. REBOURGEARD, J. ROBERT, AND G. CHARPAK. **MICROMEGAS: a high-granularity position-sensitive gaseous detector for high particle-flux environments**. *Nuclear Instruments and Methods in Physics Research Section A: Accelerators, Spectrometers, Detectors and Associated Equipment*, **376**(1):29 – 35, 1996. 35

[88] S. BIAGI. **A multiterm Boltzmann analysis of drift velocity, diffusion, gain and magnetic-field effects in argon-methane-water-vapour mixtures**. *Nuclear Instruments and Methods in Physics Research Section A: Accelerators, Spectrometers, Detectors and Associated Equipment*, **283**(3):716 – 722, 1989. 35

[89] I. GIOMATARIS, R. D. OLIVEIRA, S. ANDRIAMONJE, ET AL. **Micromegas in a bulk**. *Nuclear Instruments and Methods in Physics Research Section A: Accelerators, Spectrometers, Detectors and Associated Equipment*, **560**(2):405 – 408, 2006. 35

[90] N. ABGRALL, B. ANDRIEU, P. BARON, ET AL. **Time projection chambers for the T2K near detectors**. *Nuclear Instruments and Methods in Physics Research Section A: Accelerators, Spectrometers, Detectors and Associated Equipment*, **637**(1):25 – 46, 2011. 36

[91] S. ANVAR, P. BARON, B. BLANK, ET AL. **AGET, the GET front-end ASIC, for the readout of the Time Projection Chambers used in nuclear physic experiments**. In *Nuclear*

Science Symposium and Medical Imaging Conference (NSS/MIC), 2011 IEEE, pages 745–749, Oct 2011. 36

[92] D. CALVET. **A new versatile and cost effective readout system for small to medium scale gaseous and silicon detectors**. In *Nuclear Science Symposium and Medical Imaging Conference (NSS/MIC), 2013 IEEE*, pages 1–8, Oct 2013. 37

[93] P. HOUGH. **Method and means for recognizing complex patterns**, December 18 1962. US Patent 3,069,654. 38

[94] T. NISHIO, T. MOTOBAYASI, K. IEKI, ET AL. **NaI(TI) Detector Assembly for Low Intensity Radiation (DALI)**. In *RIKEN Accelerator Progress Report*, **29**. RIKEN Nishina Center for Accelerator-Based Science, 1996. 39

[95] S. AGOSTINELLI, J. ALLISON, K. AMAKO, ET AL. **Geant4a simulation toolkit**. *Nuclear Instruments and Methods in Physics Research Section A: Accelerators, Spectrometers, Detectors and Associated Equipment*, **506**(3):250 – 303, 2003. 42

[96] P. DOORNENBAL. **Manual of a GEANT4 Simulation Code for γ-Ray Detectors used in the RIKEN-RIBF Facility**. Accessed: 04.02.2016. 42

[97] M. MATSUSHITA. *Shape Evolution in Neutron-Rich Si Isotopes Towards the Neutron Magic Number N = 28*. PhD thesis, Department of Physics, Rikkyo University, 2013. 43

[98] O. TARASOV AND D. BAZIN. **LISE++: Radioactive beam production with in-flight separators**. *Nuclear Instruments and Methods in Physics Research Section B: Beam Interactions with Materials and Atoms*, **266**(1920):4657 – 4664, 2008. Proceedings of the XVth International Conference on Electromagnetic Isotope Separators and Techniques Related to their Applications. 48

[99] Y. SHIGA, K. YONEDA, D. STEPPENBECK, ET AL. **Investigating nuclear shell structure in the vicinity of ^{78}Ni: Low-lying excited states in the neutron-rich isotopes ^{80,82}Zn**. *Phys. Rev. C*, **93**:024320, Feb 2016. 81, 100, 102

[100] C. J. CHIARA, D. WEISSHAAR, R. V. F. JANSSENS, ET AL. **Identification of deformed intruder states in semi-magic ^{70}Ni**. *Phys. Rev. C*, **91**:044309, Apr 2015. 86

[101] A. I. MORALES, G. BENZONI, H. WATANABE, ET AL. **Low-lying excitations in ^{72}Ni**. *Phys. Rev. C*, **93**:034328, Mar 2016. 87, 89

[102] H. OLLIVER, T. GLASMACHER, AND A. E. STUCHBERY. **Angular distributions of γ rays with intermediate-energy beams**. *Phys. Rev. C*, **68**:044312, Oct 2003. 105

[103] E. SHELDON AND D. M. VAN PATTER. **Compound Inelastic Nucleon and Gamma-Ray Angular Distributions for Even- and Odd-Mass Nuclei**. *Rev. Mod. Phys.*, **38**:143–186, Jan 1966. 105

[104] J. RAYNAL. **Coupled channel code ECIS97**. Unpublished. 108, 123

[105] J. RAYNAL. **Recurrence relations for distorted-wave Born approximation Coulomb excitation integrals and their use in coupled channel calculations**. *Phys. Rev. C*, **23**:2571–2585, Jun 1981. 108, 123

[106] J. VAN DE WALLE, F. AKSOUH, F. AMES, ET AL. **Coulomb Excitation of Neutron-Rich Zn Isotopes: First Observation of the 2_1^+ State in ^{80}Zn**. *Phys. Rev. Lett.*, **99**:142501, Oct 2007. 110

[107] J. VAN DE WALLE, F. AKSOUH, T. BEHRENS, ET AL. **Low-energy Coulomb excitation of neutron-rich zinc isotopes**. *Phys. Rev. C*, **79**:014309, Jan 2009. 110

[108] N. AOI, S. KANNO, S. TAKEUCHI, ET AL. **Enhanced collectivity in ^{74}Ni**. *Physics Letters B*, **692**(5):302 – 306, 2010. 110, 111

Personal information

Martha Liliana Cortés Sua

Personal Details

Date of birth: September 28th, 1984
Place of birth: Bogotá, Colombia
Citizenship: Colombian

Education

- (07/2011–07/2016) Ph.D Student.
  Technical University of Darmstadt, Darmstadt, Germany.

- (01/2008–03/2011) Maestría en Ciencias-Física.
  Universidad Nacional de Colombia, Bogotá, Colombia.
  Thesis: *Time and energy characterization of the response of soil to gamma rays*.
  Supervisor: Dr. Fernando Cristancho.
- (01/2002–11/2007) Bachelor in Physics.
  Universidad Nacional de Colombia, Bogotá, Colombia.
  Final Report: *Study of the interaction of gamma rays with soil*.
  Supervisor: Dr. Fernando Cristancho.

- (01/1996–11/2001) Secondary school.
  Colegio El Minuto de Dios, Bogotá, Colombia.

- (01/1991–11/1195) Primary school.
  Colegio El Minuto de Dios, Bogotá, Colombia.